Surface Water as a Reporter on the Interfacial Microenvironment during Biomolecular Adhesion to Aqueous Interfaces

by

Tasha Alexandra Jarisz
B.Sc., University of Victoria, 2015

A Dissertation Submitted in Partial Fulfillment of the
Requirements for the Degree of

DOCTOR OF PHILOSOPHY

in the Department of Chemistry

Surface Water as a Reporter on the Interfacial Microenvironment
during Biomolecular Adhesion to Aqueous Interfaces

by

Tasha Jarisz
B.Sc., University of British Victoria, 2015

Supervisory committee

Dr. Dennis K. Hore, Supervisor
(Department of Chemistry)

Dr. Frank van Veggel, Academic Unit Member
(Department of Chemistry)

Dr. Jay Cullen, Non-Unit Member Member
(School of Earth & Ocean Sciences)

Supervisory committee

Dr. Dennis K. Hore, Supervisor
(Department of Chemistry)

Dr. Frank van Veggel, Academic Unit Member
(Department of Chemistry)

Dr. Jay Cullen, Non-Unit Member
(School of Earth & Ocean Sciences)

ABSTRACT

The roles of solvation and solution conditions during biomolecular and cell adhesion to surfaces are integral to gaining insight into these processes, yet remain poorly understood. Surface-specific nonlinear vibrational spectroscopy is used to characterize the silica–water interface. Sum frequency generation (SFG) experiments revealed the presence of two distinct water populations in the electrical double layer that respond differently to changes in the bulk ionic strength and pH. These results provide a new understanding of the structure of the double layer at silica–aqueous interfaces at high salt concentrations (where a Stern layer is present), and have important implications for biomolecular and cell adhesion to silica. Further SFG experiments, combined with bulk solution measurements and imaging, are then used to study silica surface conditions during the growth of *E. Coli*. As a result of the high surface charge density of silica, the water structure at the silica–aqueous interface is known to be especially sensitive to pH and ionic strength, and surface concentration profiles develop that can be appreciably different from the bulk solution conditions. We illustrate that, in the presence of growing cells, a unique microenvironment is established near the surface as a result of biopolymers and metabolites accumulating above it. Even

in the subsequent absence of cells, these charged exopolymers and osmolytes work to reduce the interfacial ionic strength as revealed by the enhanced signal from surface water molecules. In the presence of growing bacteria, an additional boost in surface water signal is attributed to a local pH that is higher than that of the bulk solution. Zeta potential measurements of silica beads with adhered bacteria—both normal and those stripped of their extracellular polymeric substances (EPS)—show an increasingly positive trend that suggests an increase in negative surface potential is not responsible for the observed changes in the sum frequency response of interfacial water. In addition, spatial correlation with SFG intensity on the surface reveals that the surface water response is independent of the number of cells adhered, and therefore the surface charge density. Finally, vibrational SFG spectroscopy, in combination with QCM-D, is used to investigate the adsorption of a hydrophobic amino acid (leucine) onto a hydrophobic surface (polystyrene) in water and heavy water. QCM-D experiments showed that more than twice the amount of leucine adsorbed to the surface when in heavy water. When this ratio of adsorbed masses is used in a model of the SFG response, the intensity and appearance of the spectral features are entirely accounted for. This suggests a similar adsorbed structure in the two solvent environments, highlighting the role solvent plays in dictating the extent of biomolecular adsorption to hydrophobic surfaces, while not altering the adsorbed structure. All of these results provide new insight into surface conditions during biomolecular and cell adhesion to hydrophilic and hydrophobic surfaces, and the important role that solvent plays in mediating these interactions.

Contents

List of Tables

List of Figures

List of Abbreviations and Definitions

Abbreviation	Definition
E. coli	*Escherichia coli*
SFG	sum frequency generation
QCM-D	quartz crystal microbalance with dissipation monitoring
CLSM	confocal laser scanning microscopy
EPS	extracellular polymeric substances
ECM	extracellular matrix
LB	Luria–Bertani broth
OD_{600}	optical density at 600 nm
LPS	lipopolysaccharide
EPM	electrophoretic mobility
EDL	electrical double layer
pzc	point-of-zero charge
DLVO	Derjaguin-Landau-Verway-Overbeek
OHP	outer Helmholtz plane
SAM	self-assembled monolayer

ACKNOWLEDGEMENTS

First and foremost, I wish to thank Dennis Hore for his immense support and encouragement. Your invaluable mentorship, enthusiasm for research, and incredible curry dinners saw me through this journey. Thank you also to my committee members, Frank van Veggel and Jay Cullen, for your advice and helpful suggestions throughout this project.

Thank you to the many members of the Hore group, past and present. Thank you especially to Lea Gozdzialski and Sarah Lane for your hard work and input on the *E. coli* project. Thank you to Sandra Roy, William Fitzgerald, and Sean Yang for putting up with my many python queries. I would also like to thank Becky Hof and Stas Konorov for their constant support and advice.

Thank you to Juli Gibbs and members of the Gibbs group at the University of Alberta for providing me the opportunity to be apart of such a successful collaboration. I would also like to thank Matt Dixon at Biolin Scientific for use of the QCM-D instrument and your input in the leucine project.

I would also like to thank Karina Giesbrecht for being such an inspiring role model. The hours spent helping me with my chemistry homework (and making it fun!) will never be forgotten. My sincere thanks also goes to my sister, lunch buddy, and fellow woman in science, Rhea Ashmead, for commiserating and laughing with me when I needed it most.

Last, but certainly not least, I could not have made it to this point without the love and support of my amazing family and friends. Mom and Dad, you never let me doubt myself and were always there to lift me up when I needed it. Ryan, you were there for me everyday on this journey, for the good days and the bad. Your unwavering support means everything to me.

Chapter 1

Introduction

1.1 Solid–Aqueous Interfaces

The solid–aqueous interface is one of the most abundant chemical systems on earth, yet its structural details remain poorly understood. Aqueous interfaces, including water, ice, electrolyte, and biological solutions are relevant to a wide variety of fields in chemistry. They play a role in all aspects of our atmospheric and oceanic environments,[1,2] in many technological applications ranging from oil extraction to phase-transfer catalysis,[3] and in most fundamental biochemical processes including respiration, ion transport, and protein folding.[4] The complexity of such interfaces is why this topic has been so widely studied these past decades; however a consensus on the details of interfacial interactions remains elusive.

The unique physical and chemical properties of aqueous interfaces arise from the strong hydrogen bonding network between water molecules, together with the asymmetry introduced by the surface. As a result, the structure of interfacial water is typically distinct from that of bulk water in terms of the distribution of hydrogen bonding species and their coordination.[5] Furthermore, interaction of interfacial water molecules with surface functional groups, for example hydrogen bonding with O–H terminated oxide surfaces, stabilizes the interfacial hydration structure. Many of the properties of water near a solid surface are therefore analogous to the hydration layers around osmolytes.[6] The adsorption

of solvated ions, polymers, solutes, biological molecules, and even cells at the surface add further complexity to these systems. However, in all of these examples, water plays an important role in mediating adhesion to solid surfaces.

1.1.1 Silica–Aqueous Interfaces

The silica–aqueous interface, and its contact with living matter, is ubiquitous in nature due to the abundance of silica in the earth's crust.[7] Silica is a solid material (either crystalline or amorphous) whose chemical formula is SiO_2. Bare silica surfaces are predominately terminated with silanol (Si–OH) groups (from incomplete condensation) and siloxane linkages (Si–O–Si), which are also present in the bulk.[7] Even in ambient conditions, water is always present around the material, leaving protons and hydroxyl (OH) groups to react with exposed Si–O bonds to produce silanols. The surface silanol density varies considerably depending on surface treatment, but has been reported in the range of 4.2–4.9 OH/nm^2.[7] Silanol groups are responsible for the hydrophilicity of silica, as they can interact with polar groups of molecules via hydrogen bonding.[7] Adjacent silanols also participate in intermolecular hydrogen bonding. Unsurprisingly, water prefers to interact with silanols over siloxane bridges.[8] This is because the former is able to both accept and donate hydrogen bonds, while the latter is only a weak hydrogen bond acceptor.[8] Since water is required to react with Si–O–Si bridges in order to produce silanols (termed rehydroxylation), it is more likely that silanol growth occurs in patches rather than homogeneously, due to siloxanes with neighbouring silanols having greater access to the water attracted to those silanols.[8]

The non-uniform distribution of silanols has a significant effect on the adsorption process, since isolated, neighbouring, and groups of mutually hydrogen bonded silanols have differing reactivity.[9] For example, water will more strongly adsorb via two hydrogen bonds to neighbouring OH groups, while a bulkier, monofunctional adsorbate will prefer to bond with an isolated silanol to reduce steric interactions. Surface silanols are integral

to biomolecular adsorption, as they directly interact via strong hydrogen bonds with polar groups on proteins or nucleic acids and with phosphate groups of membrane phospholipids and lipopolysaccharides (LPS).[7]

The point-of-zero charge for silica occurs between pH 2 and 3.[10] At lower pH, silanol groups may abstract a proton to form Si–OH_2^+ while at higher pH, they are deprotonated to form silanolates (Si–O^-). However, the probability of the former occurring is very low.[9] Behrens and Grier report the silanolate density on a glass plate at pH 7 in 5×10^{-6} M NaCl to be 0.003 silanolates/nm^2.[11] This corresponds to a surface charge density of $-0.013(2)$ C/m^2.[12] Others have found comparable values for the surface charge density under similar conditions.[13,14] One can visualize planar silica surfaces near neutral pH to be predominantly comprised of siloxane bridges interrupted by surface silanol sites, some of which are negative silanolate groups and many fewer are positively charged, protonated silanols.

Silica is an ideal surface to study bacterial adhesion due to its prevalence in many biological applications, including chromatography, sensors, assays, metal-ion extraction in aquatic ecosystems, bioremediation, and water treatment.[15–17] Moreover, its reactivity and solvation are sensitive to small changes in ionic strength, especially in the 6–8 range of biological systems.[18] As the pH of the solution is increased, deprotonation of silanol groups to form silanolates results in a more negatively charged surface. Consequently, the structure of water molecules at the silica–aqueous interface is affected by alterations in pH, as the degree to which interfacial molecules are ordered depends on the extent of hydrogen bonding and the surface charge.[19–21] Ions in solution are also known to significantly alter the water structure at silica surfaces.[18,20,22–29] Studies have shown that increasing the ionic strength of the solution results in a decreased ordering of water molecules at the interface. This may occur via two different mechanisms: increased screening of the partially negative surface charge on silica and compression of the electrical double layer; and/or electrostatic interaction of hydrated cations with the negatively charged surface, thereby disrupting

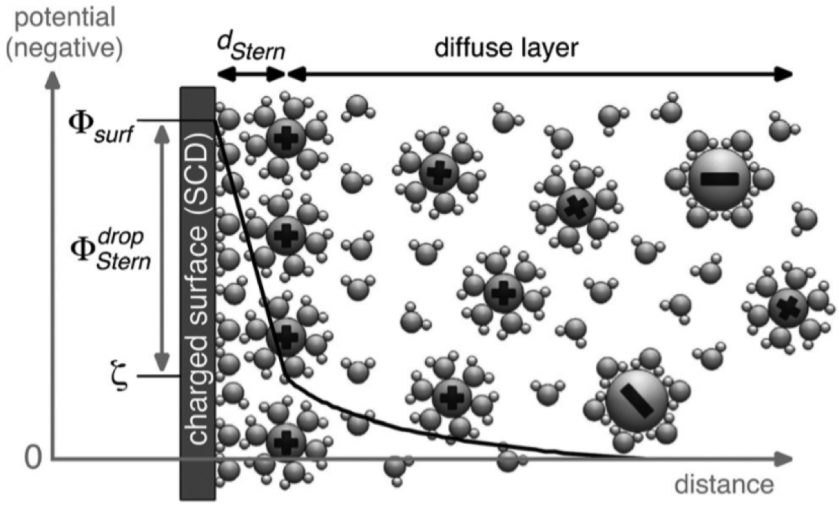

Figure 1.1: Schematic of the electrical double layer at a negatively charged surface. Adapted with permission from Ref. 31. Copyright 2016 American Physical Society.

hydrogen bonding between water molecules.[22]

1.2 The Electrical Double Layer

The electrical double layer (EDL) model is used to describe the ionic environment in the vicinity of a charged particle, colloid, or surface.[30] Negatively charged entities, such as silica, attract positive ions (counterions) in the solution, resulting in a firmly attached layer around the particle. This layer of counterions is termed the *Stern layer*. Additional positive ions are still attracted to the negative particle, however they are repelled by both the Stern layer and other counterions in solution attracted to the negative charge. This equilibrium results in the formation of a *diffuse layer* of counterions. Together, the Stern and diffuse layers form the electrical double layer, as shown in Fig. 1.1. The thickness of the EDL depends on the valency and concentration of the ions in solution. Although the presence of negative ions is scarce nearby the negative particle due to repulsive forces, their concentration gradually increases with distance until equilibrium with the bulk solution is reached. Charge density is greatest near the charged particle and diminishes further into the bulk solution, until the concentration of positive and negative ions becomes equal.

In the case of a negatively charged particle or surface, such as silica, an increase in the pH causes an increase in the number of negative surface sites. This increase in the negative surface charge density in turn increases the Debye length resulting in an expansion of the EDL. Similarly, when the ionic strength of the solution is decreased, there are fewer counterions available to screen the negative surface charge and the EDL is expanded.

Recently, techniques have emerged that enable quantitative measurement of the potential at different layers of the EDL in colloid systems. One study by Brown and co-workers[32] used X-ray photoelectron spectroscopy to measure the surface potential of silica and electrokinetic methods to measure the zeta potential. Comparing these two potentials, the authors were able to determine the thickness of the Stern layer at varying salt concentration. By 100 mM NaCl, the Stern layer contained less than one water molecule between the silica and hydrated sodium ions at pH 10. Studies such as these provide convincing evidence for an EDL model consisting of two distinct layers, as proposed by Grahame and Stern.[33]

1.2.1 Surface and Zeta Potentials

The purpose of the electrical double layer is to neutralize the charge on a surface or particle, which in turn causes an electrokinetic potential to develop between the charged surface and any point in the solution. This difference in voltage is referred to as the surface potential.[34] The magnitude of this surface potential is related to the surface charge and the thickness of the double layer. The potential drop through the Stern layer is roughly linear until the outer Helmholtz plane (OHP), where it switches to an exponential decay through the diffuse layer, until it eventually reaches zero in the bulk solution.

Electrophoresis describes how a charged particle moves with a fixed velocity when a voltage field is applied.[34] The particle's mobility is related to the dielectric constant and viscosity of the liquid medium and to the potential at the boundary between the liquid and moving particle. This boundary is known as the slip plane and is usually defined as

the point where the Stern and diffuse layers meet. Often, the position of the slip plane is approximated by the OHP. The electrical potential at this boundary is related to the particle's mobility—since the Stern layer is firmly attached while the diffuse layer is not—and is called the *zeta potential*. The zeta potential can be calculated from the electrophoretic mobility using the Helmholtz-Smoluchowski model.[34,35]

$$\mu_{\mathrm{EPM}} = \frac{2\varepsilon_0\varepsilon_r\zeta}{3\eta} f_1(\kappa a) \tag{1.1}$$

where η is the viscosity of the suspending solution, ε_0 is the dielectric constant of the liquid medium, ε_r is the electrical permittivity in a vacuum, ζ is the zeta potential, a is the radius of the particle, κ is the inverse of the Debye screening length, and $f_1(\kappa a)$ is a correcting function (the Henry function) that depends on the shape of the particle.

In an electric field, each particle, along with the ions most closely associated with it, move together through the liquid medium. The electrical potential at this surface of shear between the particle and associated ions is the zeta potential. When macromolecules adsorb onto the surface of the particle, it shifts the shear plane farther from the surface and changes the zeta potential. Consequently, the zeta potential depends on the surface charge of the particle, the composition of the liquid medium, as well as any adsorbed species. However, the surface and zeta potentials are not required to have the same sign; adsorbed polyvalent or surface active counterions may alter the zeta potential substantially.[34] Nevertheless, due to the relationship with the effective surface charge, as well as ease of measurement, zeta potential is commonly used to characterize the electrostatic contribution to cell adhesion.[36,37] Many studies have measured the zeta potential of bacteria before and after different surface treatments, as well as mutant strains, in order to comment on the role of electrostatic repulsion during adhesion to surfaces.[38–40] Even when adhesion to a planar surface is of interest, the zeta potential of particles of the same material are often measured,[41] since it is more difficult to accurately determine the zeta potential for a solid surface using streaming potential and electro-osmotic methods.[34] However, whether the zeta potential of the surface and particles is comparable is still a matter of debate.

1.3 Biomolecular Adhesion to Surfaces

Understanding the adsorption of biomolecules onto surfaces is necessary for a diverse array of scientific, engineering, and industrial applications. These may range anywhere from designing novel drug delivery systems and biosensors, to antimicrobial coatings, to biocompatible materials for medical implants.[42,43] Biomolecular adhesion refers to attachment between two biological molecules or, more commonly, between a biomolecule and a synthetic surface.[44] Biomolecules are molecules that are produced by living organisms and include amino acids, peptides, proteins, lipids, carbohydrates, nucleic acids, and metabolites, to name a few. The forces involved in biomolecular adhesion include chemical and hydrogen bonding, intermolecular and electrostatic forces, hydrophobic interactions, wetting processes, as well as steric interactions.[44] Thus the surface-adhered structure depends upon the nature of the molecule, characteristics of the surface, and the solution environment. These considerations therefore lead to three crucial interactions: solvent–biomolecule, substrate–biomolecule, and substrate–solvent.

Numerous studies have utilized a wide variety of techniques to examine biomolecular adsorption at surfaces. These include linear optical spectroscopies, such as Fourier transform infrared (FTIR), Raman scattering, and circular dichroism to identify the molecular composition of adhered biomolecules,[45–47] as well as neutron reflectivity, surface plasmon resonance spectroscopy, and the quartz crystal microbalance.[48–50] Complementary imaging techniques, such as traditional and confocal laser scanning microscopy (CLSM), together with staining and fluorescent tags, enables the distribution of various biomolecular components to be elucidated.[51] However, to obtain information about the interfacial structure, orientation, and even conformation of peptides, proteins, and other biomolecules, a surface-sensitive probe is required. One such family of techniques are based on non linear optical principles. For example, sum frequency generation (SFG) spectroscopy has been used to study the orientation of protein side chains and conformation of protein secondary

structures through alkyl and amide I vibrational signatures respectively.[44,52–54] Others have investigated the interfacial structures of membrane-bound peptides and proteins[55] as well as their function within lipid bilayers.[56] SFG is particularly useful for probing substrate–biomolecule and substrate–solvent interactions as it depends only on the polar ordering of molecules at an interface, and not on the probing depth of the optical fields; thus, there is no response from the bulk solution or substrate to overwhelm vibrational signatures from structured molecules at the surface.[57]

Surface characteristics, such as the terminal functionality, charge, roughness, and hydrophobicity play an important role in dictating both the extent and conformation of adhered biomolecules.[58,59] One study found that the adsorbed protein configuration varied depending on the hydrophobicity of the surrounding media, with preference given to aligning hydrophobic groups.[60] In the case of bacterial cell adhesion, hydrophobic interactions of cell appendages with a surface eventually lead to the formation of chemical bonds; this is because the dehydrating capability of the hydrophobic groups enables displacement of the film of water directly adsorbed to the surface.[61] It has also been shown that there is a significantly greater perturbation of interfacial water structure at hydrophobic surfaces.[62,63] Moreover, when hydrophobic side chains on proteins adsorb on hydrophobic surfaces, the major driving force is the hydrophobic interactions between them; electrostatic interactions only become significant when charged groups are present on the surface.[64,65] Nevertheless, it is generally accepted that the surface chemistry largely dictates both the extent and manner in which biomolecules adhere to surfaces, as well as the conformation of adsorbed proteins. Another important surface characteristic for biomolecular adhesion is roughness. It has been shown that rougher surfaces promote protein and cell adhesion, which has important consequences for designing implant materials.[66]

Solution characteristics, including the pH, ionic strength, and solvation environment, are integral to understanding biomolecular adhesion. Nearly all biological systems involve

interactions with, and solvation by, water molecules. However, little is known about the role interfacial water plays in mediating adsorption and adhesion processes.[67] Although aqueous environments are the most common, substitution of D_2O for H_2O as a solvent is frequently used for investigations of biological systems by magnetic resonance because of their nuclear spin differences,[68] and by IR absorbance and other vibrational techniques in order to eliminate interference in the C–H stretching region. In protein studies, D_2O is preferentially used as a solvent so that the backbone amide I stretching modes of the protein can be studied without interference from H_2O bending modes.[69] The greater strength of the O-D–O bond in D_2O than the corresponding hydrogen bond in water[70] results in greater structural ordering of D_2O.[68] This is significant as the formation and disruption of both intra- and intermolecular hydrogen bonds governs protein dynamics, which in turn dictates the structure of proteins in solution. A stronger hydrogen bond would increase solvent-solvent interactions, but would decrease the ability of the solvent to interact with hydrophilic regions on the protein. Proteins in D_2O also adopt a compressed, less flexible structure and therefore have a greater entropy and enthalpy of unfolding.[68,71] This can be attributed to the less effective solvation of hydrophobic groups at the protein surface, resulting in reduced solvent exposure of these hydrophobic regions.[70] Many studies have demonstrated that even small changes in the solution environment, such as the pH, ionic strength, or an H to D substitution, have significant effects on the stability, interfacial structure, and thermodynamic behaviour of proteins and other biomolecules,[70–73] as well as on bacterial adhesion.[65] As a result, it is critical to understand not only the consequences of such changes on biomolecular solvation and stability, but also its effects on their adsorption capabilities and structure at interfaces.

1.4 Bacterial Adhesion and Biofilms

The manner in which cells interact with surfaces plays a key role in a host of applications ranging from implant biocompatibility and biosensors, to drug delivery platforms and

chromatography.[74] Cell adhesion is a complex phenomenon, governed by interactions between molecules on the cell surface, together with the nature of the substrate and surrounding solution environment.[75] When a surface is placed in contact with a proteinaceous solution, rapid adsorption causes the formation of a conditioning film, which is necessary for subsequent adhesion of cells—an important step in the formation of biofilms.[76–79] A biofilm is a collection of adhered microorganisms and their excretion products at a solid material surface.[80] Biofilm formation is initialized by the absorption of an organic conditioning layer, whose composition changes significantly depending on the local environment of the surface to which species are adhering.[81] This conditioning step is followed by reversible, and then more irreversible adhesion of various bacteria, microbial slimes, as well as other micro- and macrofoulants from the surrounding environment.[80] Subsequent propagation of bacterial colonies and formation of a matrix of extracellular polymeric substances (EPS) results in even greater adhesion to the surface.[81] Secretion of EPS is one of the unique features of bacterial biofilms, improving adhesion and cohesion, and offering enhanced resistance to environmental stresses.[82–84]

Biofilms have significant consequences for industry and public health, due to their central role in marine and industrial equipment fouling, infectious diseases, and bioremediation.[80,85,86] For example, hydrodynamic drag on a ship hull increases exponentially with a micron-scale increase in biofilm thickness. It is estimated that the undesirable accumulation of these organisms causes billions of US dollars of economic losses per year worldwide.[80] Moreover, the growth of biofilms in hospital settings has been implicated in a variety of chronic diseases resulting from contamination of medical devices and the infectious nature of bacterial biofilms themselves, which are more resistant to antibiotics.[81] However, the formation of biofilms is not necessarily limited to negative contexts. In some situations, such as in waste treatment and bioremediation, the formation of biofilms is actually beneficial.[81]

Bacterial biofilms are ubiquitous in nature due to the ease with which they are able to

form on almost any surface.[87] They are comprised of microcolonies that are organized into complex communities, each of which has its own functional purpose.[87] The various structured communities of bacterial cells are enclosed in a polymeric matrix that is produced by the bacteria themselves, which can be adhered onto a variety of inert and living surfaces.[87] Formation of biofilms confers a selective advantage for sessile bacteria since it allows for their survival and growth in otherwise inhospitable environments.[87] As a result of growing in colonies encased in a matrix of carbohydrates and exopolysaccharides, sessile bacteria are protected from environmental hazards such as UV radiation, desiccation, extreme temperatures, nutrient deprivation, and shear forces.[88] Moreover, through biofilm formation, sessile bacteria gain a higher tolerance for antimicrobials and other stresses by forming aggregates, altering their physiology, and taking better advantage of deficiencies in host defense mechanisms.[88] The complexity of these bacterial biofilms is apparent from the various structural and metabolic systems in place, including nutrient circulation channels, consortial metabolism and the ability of different cells to express different genes (gene transfer).[89] The efficacy of certain cellular processes is also increased because of the higher cell density of biofilms compared with planktonic cells.[89]

Cells within a biofilm are distinct from their planktonic counterparts, and grow and respond to changes in their immediate environment.[90] Various triggering mechanisms that cause bacteria to switch from being planktonic to sessile have been proposed. For example, in motile bacteria, which use flagella to facilitate swimming, the trigger to switch to a sessile phenotype happens when the flagellar rotation is impeded by a surface.[91] Nanoscopic cell wall deformation resulting from adhesion forces felt by initially adhering bacteria likely also plays a role.[92] In addition, adhered cells participate in quorum sensing, which involves the excretion of specific signalling molecules that result in the bacteria adopting a phenotype distinct from those in solution.[93] It may also involve the use of cell-associated sensors to determine the immediate cell concentration.[94] Regardless of the trigger mechanism, when bacteria sense a surface and greater numbers of cells nearby, they

begin to produce extracellular polymeric substances (EPS) and fimbriae in larger quantities, which help bacteria adhere more strongly to the surface and each other, eventually lending structural stability to the biofilm matrix.[76,95] At the end of the biofilm life cycle, bacteria can be released back into the planktonic phase via passive (sloughing, erosion) or active (enzymatic degradation) processes.[96] This may occur as a result of a variety of different environmental factors, including the need to colonize new surfaces with greater nutrient or oxygen availability.[97]

Studies varying the surface and solution conditions have concluded that the nature of the surface, including its charge, hydrophobicity, and roughness, as well as pH and ionic strength of the environment, are critical features influencing the amount and conformation of adsorbed proteins and cells.[65,98–102] The solvation environment plays an integral role in both protein and bacterial adhesion, such that changes in the hydration structure at the surface are a sensitive measure of early adhesion events. Water constitutes by far the largest part of the environment in which most bacteria grow, and is also the major component of the EPS matrix. Polymers within this matrix trap ions and water molecules, creating chemical gradients that are distinct from the bulk solution.[103] The formation of these microenvironments, in which water plays a significant role, is important for bacterial adhesion and colony growth. Water molecules may compete for hydrogen bonding opportunities with both proteins and the surface, thereby suppressing protein adsorption.[104,105] On the other hand, dehydration of hydrophobic regions on cell membrane proteins are thermodynamically favourable due to the increased entropy of the displaced waters. This serves to promote protein adsorption and consequently cell adhesion, especially for globular proteins that may alter their conformation and unfold upon adhesion to a surface.[106] The surface charge and presence of co-solvating ions have also been shown to be important factors in mediating protein and cell adhesion.[107] Consequently, the extent of adhesion to charged surfaces is influenced by the pH and ionic strength of the aqueous medium.

1.5 DLVO Theory and Bacterial Adhesion

Derjaguin-Landau-Verway-Overbeek (DLVO) theory describes long-range, macroscopic interactions between charged particles in an aqueous medium.[108] This theory is also commonly used to interpret particle deposition to surfaces. According to the classical DLVO theory, there are two types of interactions that govern adhesion: (1) long-range, attractive Van der Waals forces and (2) medium-range, repulsive electrostatic interactions. The total potential energy of the interaction is given by the sum of the Van der Waals and electrostatic forces. This model has often been used, both qualitatively and quantitatively, to describe biomolecular adhesion to surfaces. More recently, an extended DLVO theory has emerged to better describe the adhesion of bacteria and other microorganisms to surfaces. The inclusion of short-range, specific interactions was needed to account for the observation that bacteria adhere to surfaces despite the fact that the interfacial free energy of adhesion is positive and when there is significant electrostatic repulsion.[61] This extended DLVO, or XDLVO, also includes short-range, Lewis acid-base interactions.[109,110] In addition to the classical DLVO Van der Waals and EDL interactions, it takes into account attractive hydrophobic interactions and repulsive hydration effects.[111] Therefore, the total adhesion energy can be expressed as

$$\Delta G^{\mathrm{adh}} = \Delta G^{\mathrm{vdW}} + \Delta G^{\mathrm{EDL}} + \Delta G^{\mathrm{AB}} \tag{1.2}$$

where ΔG^{VdW} and ΔG^{EDL} are the classical Van der Waals and double layer interactions and ΔG^{AB} represents the acid-base interactions.

A two-step process for bacterial adhesion was first proposed by Zobell in which cells first interact in a reversible manner with a surface, eventually forming more irreversible attachments to specific surface sites.[112] AFM studies have shown that over time, more tethers to the surface become involved in adhesion of a bacterium.[92] In light of this, it is clear why XDLVO theory is needed to account for short-range, covalent or hydrogen-bonding interactions that occur with time, resulting in stronger adhesion of cells to a

surface. Although classical DLVO can account for initial reversible interactions of the cell with the substrate, specific interactions of membrane proteins, lipopolysaccharides, adhesins, and exopolymers on the cell surface are ultimately responsible for overcoming electrostatic repulsion and forming strong, more irreversible attachments that anchor the cell to the substratum.[61]

In accordance with DLVO, bacterial surface charge is well known to affect adhesion to solid surfaces, although its effect is not consistent among different strains and substrata.[61] Most bacteria (including *E. coli*) and surfaces to which they adhere have a negative charge under physiological conditions. This negative charge, resulting from carboxyl and phosphate functional groups, can either be uniformly distributed or may alternate with positive regions due to the presence of amino groups.[61] Moreover, the cell surface of adhered bacteria become more negative as they mature, largely due to the production of exopolymers that help daughter cells aggregate within a surface microcolony.[91] Such biological changes in bacteria upon 'sensing' a surface, as well as inherent complexities of living cells compared with inert particles, may render it impossible to use current physico-chemical models alone to predict bacterial adhesion to surfaces.

1.6 Extracellular Polymeric Substances

Extracellular Polymeric Substances (EPS) primarily consist of polysaccharides, with smaller amounts of proteins, nucleic acids, and lipids. These highly dense biopolymers are secreted from bacteria during cell proliferation.[113] The production of EPS to form a protective extracellular matrix (ECM) is induced by several environmental signals including motility impairment from surfaces, extreme temperatures, low nutrient availability, and oxidative stress.[114] The ECM not only anchors cells to a surface in a protective sheath, but also acts as a nutrient reservoir that is ideally suited to resource capture.[96] This results from both the sorptive nature of EPS constituents and their ability to retain extracellular enzymes for digestion outside the cell. Thus, biofilms are not only able to take up nutrients from the

aqueous environment, but also to digest biodegradable components from the substratum, cell debris after lysis, as well as structural EPS to release cells from the biofilm.[96] The close proximity of cells within the matrix also allows for efficient transfer of nutrients between stationary cells.[115]

With the use of CLSM, together with fluorescence staining, Neu and Lawrence were able to visualize the highly complex, structured nature of the EPS matrix containing distinct components and channels.[116] It is the structure of the EPS matrix that allows for the remarkable properties of biofilms, their high cell densities, and long-term proximity of cells.[96] Cohesion and stability of EPS are a result of inter- and intra-physicochemical interactions of proteins, polysaccharides, nucleic acids, curli, fimbriae, cellulose, and amyloids.[96] Under stagnant or low flow conditions, biofilms are less cohesive and weaker than biofilms formed under high flow conditions, which tend to be stronger, larger, and more viscoelastic.[117]

Even though the EPS matrix is highly hydrated, it has been found to have a slightly different refractive index than water.[118] As a result, EPS scatter photons forward instead of reflecting them. This means that light enters into the biofilm instead of being reflected off its surface. This would be especially important for biofilms containing photosynthetic microorganisms, in which light would need to reach those at the bottom (closest to the surface).[96]

EPS can be categorized into two groups based on their distance from the cell membrane: those that are tightly bound to the cell and those that are more loosely associated. Bound EPS are covalently bonded to the cell, whereas loosely bound, or “free EPS” are secreted by the bacteria, either remaining nearby or dispersing into solution.[103] A combination of centrifugation with a cation exchange resin (CER) extraction process can be used to separate bound and free EPS from the cell surface.[37,119] This extraction process has been reported to be the most effective method to remove bacterial EPS with minimal cell lysis.[120] Thus, using this technique, it is possible to compare the effect that EPS has on adhesion

for the same strain of bacteria. Studies have found that CER treatment either decreased the surface charge density[121] or had little effect on the zeta potential[37] of *E. coli*; however, the former study found EPS removal enhanced *E. coli* adhesion to soil particles (attributed to a decrease in electrostatic repulsion with the surface) while the latter found CER treatment decreased the deposition efficiency of the cells to silica. Despite this discrepancy, numerous studies have shown the important role that EPS play in cell adhesion to surfaces and cohesion in biofilms.[76,96]

The specific composition of EPS surrounding cells in a colony is dependent on the stage of growth and other critical features of the environment, which dictate the formation and proliferation rate of the eventual biofilm.[103] EPS contain a variety of both positively and negatively charged functionalities that enhance the adhesive and aggregative capabilities of bacteria by enabling cells to overcome possible repulsive interactions with the surface and each other.[122] For *E. coli*, the main constituents of the EPS matrix are curli, cellulose, type I pili, flagella, capsule sugars, colanic acid, and β-1,6-N-acetylglucosamine.[114] Nonetheless, nearly all EPS components secreted by bacteria readily bind cations, anions, and other osmolytes, effectively making these polymers "ion sponges".[103] This is necessary not only for structural stability (especially through divalent ionic bridging of structural EPS), but also for the capture of essential nutrients.[96] These exopolymers are also integral to aggregation of daughter cells in order to begin biofilm formation; mutants that are unable to produce EPS can still attach to a surface, but cannot form microcolonies.[123] Thus, EPS may not be essential for initial cell adhesion, but are required to prevent daughter cells from dispersing into solution, which would prevent biofilm growth. It is clear that EPS are more than just the glue holding biofilms together. In fact, they are multifunctional, diverse molecules that make biofilm life successful.

1.7 The Interfacial Environment and Biofilms

The surface-adsorbed structure of biomolecules and cells is governed by the nature of the adsorbate, surface characteristics, and the solution environment. As previously mentioned, there are three critical interactions that govern adhesion: solvent–analyte, substrate–analyte, and substrate–solvent. The last two interactions require a surface-specific probe restricted to a few nanometers or less. This is particularly true of efforts to probe interfacial water structure without being overwhelmed by bulk water signal. Second-order nonlinear optical techniques are ideal probes of such interactions, as their reporting depth is determined by the polar arrangement of molecules (a break in the macroscopic inversion symmetry) rather than the penetration of the optical fields.

One such nonlinear optical technique, SFG spectroscopy, has been used to study the ECM of living cells and mechanisms of early biofilm formation.[124,125] In one study, results from time-lapse SFG spectra on living cells show the accumulation of ordered protein adsorbates of the ECM at the substrate interface (calcium fluoride) only 1 hour after cell inoculation.[124] SFG spectroscopy has also displayed an ability to overcome the need for labelling and fixation to study interfaces buried under a layer of living cells.[125,126] In a study by Diesner et al., SFG spectroscopy was successfully used to detect alkanethiol self-assembled monolayers (SAMs) buried beneath a layer of erythrocytes by identifying vibrational fingerprints characteristic of the SAM and comparing with those in the IR spectrum of these species.[125] In another study, SFG spectroscopy was used to characterize the ECM layer during early biofilm formation adjacent to a gold surface beneath a layer of cells.[126] Results from the SFG spectra were compared with those from infrared reflection-absorption spectroscopy (IRRAS) in the C–H stretching region. The authors found that cells have a random distribution of C–H groups and so do not contribute to the SFG signal, resulting in almost identical SFG spectra for samples with and without cells adsorbed.[126] Similarly, the studies by Diesner et al.[124,125] also reported

little contribution from biological structures in erythrocytes to the SFG spectra, even though many of these structures are known to be ordered. Bulard et al. reported similar results using bacteria.[100,101] Consequently, changes in the interfacial environment as a result of adhesion were observed indirectly through changes in regions of the SFG spectra corresponding to water (O–H stretching) and ODT SAMs (C–H stretching). Results from these studies demonstrate the integral role that the interfacial environment plays in the early formation of biofilms. Moreover, they indicate the usefulness of SFG spectroscopy as an analytical tool in establishing vibrational fingerprints of various cell-conditioned surfaces, even in the absence of spectral signatures from the cells themselves. SFG is also capable of offering information about the molecular structure of biofilm components—including ordered water—at a variety of different interfaces.

1.8 *Escherichia coli*

E. coli is the most widely studied prokaryotic model organism.[127] It is a gram-negative bacterium that can utilize aerobic respiration if oxygen is present, or switch to fermentation in anaerobic conditions.[128] The rod-shaped cells are approximately 0.8–1 μm in diameter and 2–4 μm in length.[129] The cells are bounded by a pair of membranes—an inner, plasma membrane and outer membrane—with a stiff peptidoglycan layer forming the cell wall in between them. Bacteria metabolize nutrients that diffuse through the cell membranes into biomass, becoming larger in size until eventually dividing into two daughter cells. This process is known as binary fission. For *E. coli*, this can happen every 20 minutes under ideal conditions.[128] *E. coli* are primarily comprised of proteins, for which 4288 genes in the DNA sequence encode for.[130] Gene expression occurs when DNA is transcribed to messenger RNA, which is then translated, a process which builds a chain of amino acids that fold into the final protein.[131] Environmental changes or specific signalling molecules can cause bacterial cells to express certain proteins, while turning off the expression of others. This process is known as gene regulation.[131] Most strains of *E. coli* are harmless

and are found in the lower intestine of warm-blooded organisms; however, some strains are pathogenic and can cause serious infections.[130] Other strains (including K12 isolates) are motile, with flagella to facilitate propulsion in liquid media or pili that allow them to crawl along a surface.[132]

It has been shown that adjacent to the bacterial outer membrane lies a nanointerface (on the order of 1 nm) that has unique ionic dynamics, made possible by an assembly of highly ordered water molecules.[105,133] Beyond this nanointerface, there exists an extracellular layer that extends several hundred micrometers above the outer membrane.[133] This "unstirred layer" contains ions, extracellular regions of membrane proteins and their glycans, as well as glycoproteins. This region serves as a diffusion barrier and is not readily mixed with the bulk solution, allowing it to maintain distinct physicochemical gradients of solutes and water.[133] In addition, this unstirred layer is unlikely to exist for highly aggregated bacteria, where the intercellular space between neighbouring cells is too narrow to accommodate its presence.

The bacterial outer membrane undergoes frequent turnover and remodelling in response to changes in the local environment.[134] One example of this is the release of outer membrane vesicles. These vesicles are 20–300 nm in diameter and contain periplasmic and surface constituents from the outer membrane of gram-negative bacteria, including *E. coli*. Their purpose is to allow bacteria to communicate remotely once adhered to a surface (quorum sensing) and to modulate their external environment.[134] Thus, through excretion of both free EPS and outer membrane vesicles, bacteria can have a significant impact on the surrounding environment beyond the immediate area where they are adhered.

In batch culture growth of bacteria, a fixed amount of nutrients is contained within the growth medium and the environmental conditions (temperature, aeration) are controlled such that the increase in cell density can be measured over time. This is known as a growth curve, and is typically measured using the optical density at 600 nm. Three distinct phases are observed in the growth curve: lag, exponential, and stationary phase. Each of these

phases involves a distinct growth rate and set of physiological changes of the cells. In the lag phase, the growth rate is almost zero as the cells adapt their physiology to the culture conditions.[135] The length of the lag phase can range anywhere from minutes to hours and is dependent on the initial cell concentration, type of growth medium, or how long the cells remained in a starved state.[136] For example, if exponential phase cells are diluted in fresh media under the same growth conditions, there may be no noticeable lag phase; however, if the same cells are taken from a stationary phase culture, those cells must shift their physiology to exponential phase cells and so a lag phase will be observed.[135] During the exponential phase, rapid, logarithmic growth occurs. The rate of growth during this phase depends on nutrient availability, temperature, extent of aeration, and other environmental factors. The final stationary phase is characterized by no net growth; cells still divide but this is balanced by an equal number of cells dying. This appears as a plateau in the growth curve. Cells in stationary phase undergo morphological changes. For example, *E. coli* lose their rod shape and become much smaller and rounder as a result of several cell divisions without an increase in cell mass.[137] The hydrophobicity of the bacterial surface also decreases with increased starvation time.[16]

Cells may enter the stationary phase for a number of reasons. The most common is that the main source of carbon, energy, or other vital nutrient is used up. However, cells that lyse (break apart) can provide nutrients to remaining cells to facilitate some growth. Alternatively, cells may enter stationary phase due to a build up of toxic waste products that inhibit cell growth.[135] Regardless of the specific trigger, a combination of nutrient gradients, waste product levels, oxygen level, and signalling molecules all determine whether bacteria grow and proliferate or enter into stationary phase, allowing them to use their remaining resources for maintenance and survival. Throughout the stationary phase, even though cells are starved for nutrients and so cannot divide, many remain viable. They enter a metabolically less active and more resistant state, waiting for more nutrients to become available for growth to resume.[137]

E. coli is an ideal model bacterium because of its rapid growth rate and achievement of high cell densities in inexpensive media.[127] The most common laboratory strain, *E. coli* K12 MG1655, has been widely studied and well characterized. Various *E. coli* K12 isolates are commonly used in molecular cloning and recombinant protein production.[127] As such, they have been bred to survive only under specific culture conditions and would not be able to thrive in their natural environment (e.g. the human intestine). One consequence of this evolutionary adaptation is their reduced ability to produce EPS, since they are not necessarily required to attach to surfaces in order to survive.[138] Consequently, *E. coli* K12 requires more time in order to attach to surfaces and produce biofilms.[114]

Chapter 2

Methods

2.1 Cell Culture

Escherichia coli K12 MG1655 (ATCC 700926) were kept at -80 °C in LB media (Lennox, BD Difco Laboratories) containing 50% (vol./vol.) glycerol. Our Lennox formulation of LB consists of tryptone (10 g/L), yeast extract (5 g/L) and sodium chloride (5 g/L). For SFG experiments, 5 mL of LB in a sterile, vented tube was inoculated with cells and grown at 37 °C with shaking at 200 rpm overnight. This pre-culture was then diluted 1:100 by volume in fresh LB into a sterile 50 mL baffled flask and grown at 37 °C with shaking at 200 rpm until an OD_{600} of 0.25 was reached, corresponding to early exponential phase. This exponential phase liquid culture was then diluted 1:100 by volume with 9 mL sterile LB and placed into a custom-built, Teflon sample chamber in the SFG spectrometer (cell density = 2×10^6 cells/mL). The bacteria were grown inside this chamber at 37 °C and were aerated with stirring. Spectra were collected every hour for approximately 27 h. In earlier experiments, the population growth curve was measured in a baffled flask in a shaker–incubator at 37 °C and 200 rpm. In later experiments, it was measured in the Teflon sample chamber at 37 °C with stirring in order to maintain identical growth conditions to SFG experiments. The optical density at 600 nm was measured at regular intervals using a cell density meter (Fisher Scientific, Model 40).

2.2 Cation Exchange Resin Treatment

The procedure to release bound EPS using a cation exchange resin (CER) was developed by Frolund et al.[119] A pre-culture was inoculated in the same manner as stated in section 2.1. This pre-culture was then diluted 1:100 by volume in fresh LB into a sterile 50 mL baffled flask and grown at 37 °C with shaking at 200 rpm until an OD_{600} of 0.55 was reached, corresponding to mid-exponential phase, to ensure enough cells were present to proceed with the CER treatment. The mid-exponential liquid culture (10 mL) was centrifuged at 3750 rpm (Beckman Coulter Allegra X-12R Centrifuge) for 15 min at 4 °C. The pelleted cells were washed three times with sterile extraction buffer (2 mM $Na_3PO_4 \cdot 12H_2O$; 4 mM Na_2HPO_4; 9 mM NaCl; 1 mM KCl; adjusted to pH 7 with HCl) and then suspended in 10 mL of the same buffer. After soaking in 18.2 MΩ·cm water overnight, 2 g of hydrated CER (Dowex Marathon C Sodium Form, Sigma) was added to the cell suspension, which was stirred at 600 rpm for 1.5 h at 4 °C. The supernatant was then decanted and centrifuged to isolate the treated cells, which were washed three times with extraction buffer. The cells were then suspended in 5 mL of LB and subsequently diluted 1:100 by volume in fresh LB to be placed directly into the SFG spectrometer. The growth of the CER-treated cells was then monitored under the same conditions as untreated bacterial cells.

2.3 Vibrational Sum Frequency Generation Spectroscopy

In recent years, visible–infrared sum frequency generation (SFG) spectroscopy has emerged as a premier technique for studying the structure of adsorbed molecules.[139–141] It is particularly attractive for probing the interface between two centrosymmetric media, such as the solution–isotropic solid interface.[142–144] This is because, under the electric dipole approximation, the second-order nonlinear susceptibility, $\chi^{(2)}$, equals zero in the bulk solution, but is non-zero at the interface where the symmetry is broken. In the case of molecules at interfaces, the requirement that $\chi^{(2)} \neq 0$ necessitates that they be oriented in

a polar manner. As a consequence, molecules can be situated very near the interface but, if they are not adsorbed, they will not be oriented and therefore remain undetected by SFG. In contrast to evanescent-wave techniques such as ATR-IR, or bulk spectroscopic probes that require grazing angles to achieve surface specificity, SFG spectroscopy provides an exquisite sensitivity to the interface since it is the symmetry of the molecular environment that governs its response.

As shown in Fig. 2.1a-c, we use visible–infrared SFG to probe the interfacial water environment, where one of the probe lasers is at a frequency ω_{vis}, typically 18,797 cm^{-1} (532 nm), far from any electronic or vibrational resonance, and the other is tuned from $\omega_{\text{IR}} = 2800\text{–}3800\ \text{cm}^{-1}$ to cover the distribution of O–H stretching frequencies. We detect the light emitted at the sum frequency $\omega_{\text{vis}} + \omega_{\text{IR}}$, and plot its intensity as a function of ω_{IR}. As shown in Fig. 2.1d, one advantage of this particular $\chi^{(2)}$ process is that the emitted light is at a higher frequency than the visible laser beam, so there is no difficulty associated with fluorescence. Furthermore, for the range of frequencies listed above, the SFG appears between 442–463 nm, ideal for low-light level detectors with peak response in the blue/green. These SFG measurements provide a feature-rich description of the structure of molecules adsorbed on surfaces.[145–147]

At neutral surfaces, SFG signal arises from the second-order polarization $P^{(2)}$ as a result of ordering of molecules at a surface. The polarization can be considered as the expansion of both linear and nonlinear terms

$$\begin{aligned} P &= P^{(1)} + P^{(2)} + P^{(3)} + \cdots + P^{(n)} \\ &= \varepsilon_0 \left(\chi^{(1)} E + \chi^{(2)} E^2 + \chi^{(3)} E^3 + \cdots + \chi^{(n)} E^n \right) \end{aligned} \tag{2.1}$$

where ε_0 is the vacuum permittivity, $P^{(1)}$ is the linear contribution and $P^{(n)}$ are the nth-order nonlinear terms. The second-order polarization $P^{(2)}$ is proportional to the second-order susceptibility $\chi^{(2)}$, which arises from the sum of the hyperpolarizabilities ($\alpha^{(2)}$) over all

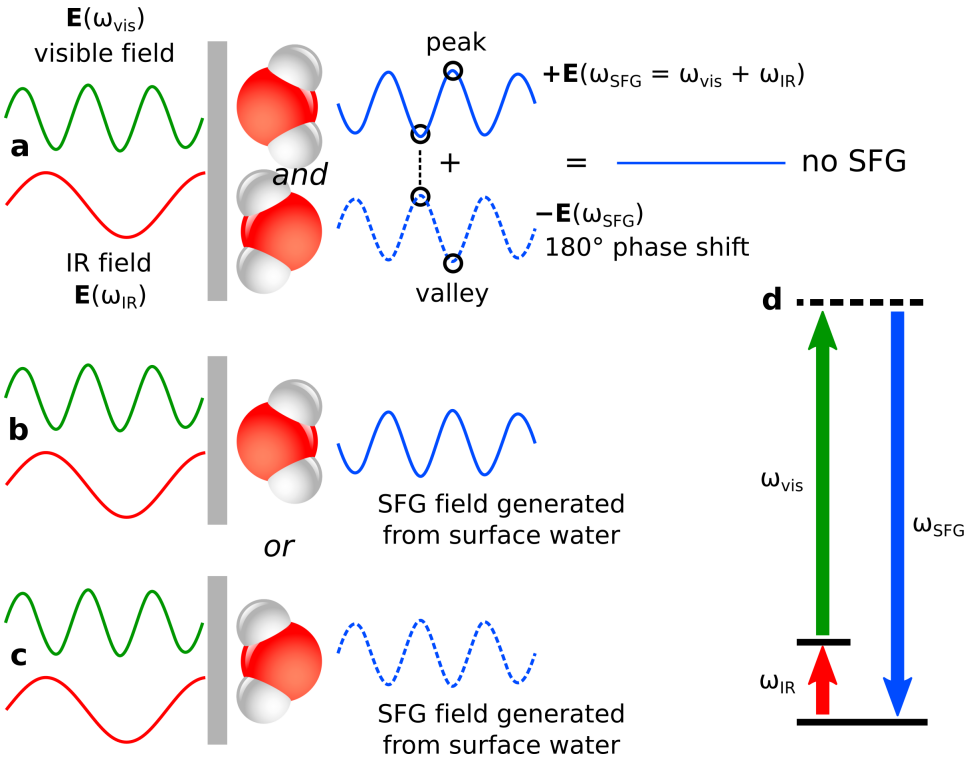

Figure 2.1: (a) In the bulk, light produced from the second order polarization destructively interferes with that from another molecule with opposite orientation, so no SFG can be measured from bulk water. At the surface, water has a preference for its orientation based on hydrogen bonding opportunities, so SFG is detected from these species, and the phase of the emitted field is shifted by 180° for molecules with their (b) oxygen or (c) hydrogen directed toward the surface. (d) An energy level diagram illustrating the process of sum frequency generation. Reprinted with permission from Ref. 57. Copyright 2018 American Chemical Society.

molecular orientations. This can be expressed as the average over participating orientations

$$\begin{aligned}\chi^{(2)}(\omega_{\mathrm{IR}}) &= \frac{1}{\varepsilon_0}\sum_{\text{molecules}} \alpha^{(2)}(\omega_{\mathrm{IR}}) \\ &= \frac{N}{\varepsilon_0}\langle\alpha^{(2)}(\omega_{\mathrm{IR}})\rangle\end{aligned} \tag{2.2}$$

where N is the number of species involved in the second-order process. An increase in ordering results in an increase in $\chi^{(2)}$ and thus an increase in the intensity of the SFG signal. The hyperpolarizability may be expressed as

$$\langle\alpha^{(2)}(\omega_{\mathrm{IR}})\rangle = \sum_q \frac{1}{2m_q\omega_q}\left\langle\left(\frac{\partial\alpha^{(1)}}{\partial Q}\right)_q\left(\frac{\partial\mu}{\partial Q}\right)_q\right\rangle\frac{1}{\omega_q-\omega_{\mathrm{IR}}-i\Gamma_q} \tag{2.3}$$

where ω_{IR} is the infrared frequency, m_q is the reduced mass, ω_q the frequency, Γ_q the line

width, and $(\partial\alpha^{(1)}/\partial Q)_q$ and $(\partial\mu/\partial Q)_q$ are the harmonic approximations to the Raman transition polarizability and transition dipole moment respectively at the q^{th} normal mode.

In the electric dipole approximation, molecules in non-centrosymmetric environments (substrate surface, adsorbates, and aligned interfacial water) contribute to $\chi^{(2)}$ and one measures

$$I_{\text{SFG}} \propto \frac{\omega_{\text{SFG}}^2}{n_{\text{SFG}} n_{\text{vis}} n_{\text{IR}} \cos^2\theta_{\text{SFG}}} \left| (L_{yy}e_y)_{\text{SFG}} \chi^{(2)}_{yyz} (L_{yy}e_y)_{\text{vis}} (L_{zz}e_z)_{\text{IR}} \right|^2 I_{\text{vis}} I_{\text{IR}} \tag{2.4}$$

where I_i are the intensities of the detected SFG beam, and the input visible and IR pump beams, $\omega_{\text{SFG}} = \omega_{\text{vis}} + \omega_{\text{IR}}$, n_i are the refractive indices of the incident medium, and θ_{SFG} is the angle of the reflected SFG beam. In our experiment, we apply s-polarized visible and p-polarized infrared beams, and detect the s-polarized component of the SFG. As shown in Eq. 2.4, this is a measure of $\chi^{(2)}_{yyz}$. Here, it is particularly important to consider not the incident but the surface fields obtained from

$$L_{yy,\text{SFG}} = 1 + r_{s,\text{SFG}} \tag{2.5a}$$

$$L_{yy,\text{vis}} = 1 + r_{s,\text{vis}} \tag{2.5b}$$

$$L_{zz,\text{IR}} = 1 + r_{p,\text{IR}} \tag{2.5c}$$

where r_s and r_p are the conventional s- and p-polarized Fresnel reflection coefficients, and the unit polarization vectors $e_{y,\text{SFG}} = e_{y,\text{vis}} = 1$, $e_{z,\text{IR}} = \sin\theta_{\text{IR}}$. As r_s and r_p are functions of the refractive index, their dispersion must be taken into account.

At charged surfaces, there is contribution from a third order component $P^{(3)}$ to the intensity of the SFG signal, which is proportional to the third order susceptibility $\chi^{(3)}$. This term arises from isotropic bulk water molecules ($\chi_{\text{iso}}{}^{(3)}$) and from oriented molecules due to the surface-originating electric field E_0.[148] The SFG response is therefore a result of both second and third-order processes occurring simultaneously and is given by

$$\begin{aligned} I_{\text{SFG}}(\omega_{\text{IR}}) &\propto \left| P^{(2)} + P^{(3)} \right|^2 \\ &= \left| \chi^{(2)}(\omega_{\text{IR}}) E_{\text{vis}} E_{\text{IR}}(\omega_{\text{IR}}) + \chi^{(3)}(\omega_{\text{IR}}) E_{\text{vis}} E_{\text{IR}}(\omega_{\text{IR}}) \int_0^\infty E_0(z)\mathrm{d}z \right|^2 \end{aligned} \tag{2.6}$$

where E_{vis} and E_{IR} are the 532 nm and infrared pump beam electric fields, E_0 is the surface charge-induced electric field, and z is the distance normal to the interface.

For SFG experiments, a 1064 nm Nd:YAG laser with 25 ps pulse width and 10 Hz repetition rate (Ekspla PL2241) is doubled to produce the 532 nm visible beam, as well as to produce a tunable infrared beam with frequencies ranging from 2700–3800 cm^{-1} with 5–25 cm^{-1} step size in a BBO/$AgGaS_2$-based OPA/OPG/DFG parametric generator (Ekspla PG501). The visible and IR beams are spatially and temporally overlapped at the interface at 68° (or 64.8°) and 60° (or 56.8°) for the visible and IR beams respectively. Beam diameters for the IR and visible beams are 0.5 mm and 1 mm respectively. Cell cultures were grown inside a custom Teflon sample chamber mounted against a piranha-cleaned, fused silica dove prism (Del Mar Photonics) via a fluoropolymer O-ring (Marco Rubber, NH) in order to create a water tight seal. This chamber was enclosed in an aluminum block fitted with a recirculating water bath channel (VWR, Model 1167P) to maintain the system at 37 °C. Cultures in the chamber were aerated via stirring using a custom paddle attached to a DC motor. The resulting SFG signal from the interface was detected by a gated photomultiplier tube (Hamamatsu R7899) after passing through a 532 nm notch filter and monochromator so as to remove any of the reflected light from the pump beams. All SFG spectra were collected with p-polarized IR and s-polarized visible beams by scanning the energy of the IR beam. An increase in SFG signal results from resonance of $\chi^{(2)}$ and $\chi^{(3)}$ when the frequency of the IR pump beam approaches the frequency of the vibrational transitions corresponding to the O-H stretching modes for interfacial water or C–H stretching modes for leucine.

2.4 Quartz Crystal Microbalance with Dissipation Monitoring

The quartz crystal microbalance with dissipation monitoring (QCM-D) is a high resolution mass-sensing technique. A QCM sensor oscillates at a specific frequency when a voltage

is applied, which is directly related to the mass of adsorbed molecules, according to the Sauerbrey relation.[149] For rigid films in a vacuum, the Sauerbrey equation is sufficient to relate such changes in frequency to the mass of the adsorbed layer; however, it fails for soft, viscoelastic films or under liquid conditions. In these cases, another model, such as the Kevin–Voigt model, must be used. In addition to measuring frequency changes, QCM-D instruments can also measure dissipation (energy loss) in the film, which is related to the viscosity and elasticity of the molecular layer.[149] By measuring both the frequency and dissipation shifts for several harmonics, the Voigt model can be applied in order to obtain the adsorbed mass and viscoelastic properties of the film.[150] Within the last decade, QCM-D has become integral to studying molecular systems at solid–liquid interfaces, including the adhesion of complex polymer and biochemical systems.[151,152] In recent years, its capabilities have been combined with optical techniques such as ellipsometry,[153,154] IR absorption,[155,156] and SFG spectroscopy.[157–161]

The quartz crystal microbalance measures changes in an oscillating quartz crystal's resonant frequency when an AC voltage is applied. For rigid films, the Sauerbrey relation may be used to directly relate frequency changes to the mass of the adsorbed layer. However, for viscoelastic deposition in liquids, i.e. the adhesion of soft films, the resonant frequency of the crystal is altered by acoustic–fluid damping of the viscoelastic medium.[162] As a result, the shear wave decays very rapidly and the QCM probes only objects that are within a micron of the crystal surface, making it a surface-sensitive technique. Due to energy losses from the shear wave when travelling through less rigid adsorbed films, large changes in dissipation and resonant resistance also arise. Combining frequency shift measurements with changes in the dissipation factor have been termed QCM with dissipation (QCM-D). As a result, in addition to detecting mass changes, QCM-D sensors provide information about interactions with soft matter, in which changes in the density and viscoelastic properties of the film can be determined. When using QCM-D under liquid conditions, the density and viscosity of the solution, together with the softness of the

adsorbed film, cause significant energy losses that must be taken into account.

In a damped environment, the Sauerbrey equation underestimates the adsorbed mass from the measured frequency shift.[163] As a result, the frequency changes alone are rarely able to characterize the entire system. With access to both the frequency shift Δf_n and the dissipation shift ΔD_n for multiple harmonics n in a QCM-D experiment, models such as Kevin–Voigt may be applied to characterize the viscoelastic parameters and provide a more accurate adsorbed mass.[149,150,164]

When the viscoelastic layer is thin and the oscillator is immersed in the leucine solution, the frequency and dissipation shifts are approximately given by

$$\Delta f_n^{\text{soln}} \approx -\frac{1}{2\pi\rho_0 h_0}\left[\frac{\eta_2}{\delta_2} + h_1\rho_1 n\omega_0 - 2h_1\left(\frac{\eta_2}{\delta_2}\right)^2 \frac{\eta_1 n^2\omega_0^2}{\mu_1^2 + (n\omega_0\eta_1)^2}\right] \tag{2.7a}$$

$$\Delta D_n^{\text{soln}} \approx \frac{1}{\pi n f_0\rho_0 h_0}\left[\frac{\eta_2}{\delta_2} + 2h_1\left(\frac{\eta_2}{\delta_2}\right)^2 \frac{\mu_1 n\omega_0}{\mu_1^2 + (n\omega_0\eta_1)^2}\right] \tag{2.7b}$$

where the acoustic wave penetration depth is

$$\delta_2 = \sqrt{\frac{2\eta_2}{\rho_2 n\omega_0}}. \tag{2.8}$$

In the above equations, $f_0 \approx 5$ MHz is the fundamental vibration frequency of the crystal, $\omega_0 = 2\pi f_0$, and n is the harmonic number. $\rho_0 = 2148$ kg/m^3 is the density of the quartz crystal, ρ_1 is the density of the adsorbed layer, and ρ_2 is the density of the leucine solution. The viscosities of the layer and solvent are given by η_1 and η_2, respectively. The adsorbed layer of thickness h_1 has a shear elastic modulus μ_1.

In typical QCM-D experiments, the frequency and dissipation changes resulting from adsorption of a solute in dilute solution are compared to the values measured in the absence of the solute (pure solvent or buffer). In such cases, Eq. 2.7 is simplified in practice since the shifts can be measured with respect to the solvent baseline, and all subsequent changes in Δf and ΔD may be attributed to adsorption. In other words, in the limit of infinite dilution, the bulk solute and reference solvent have the same effect on the sensor surface. In our experiment, however, we are dealing with concentrated solutions and so the analysis

is not as straightforward, since the reference solvent and bulk solution do not result in the same measured shifts prior to adsorption. We therefore perform an initial measurement with either pure water or pure D_2O, where the frequency and dissipation factor shifts (with respect to air) are given by

$$\Delta f_n^{\text{solvent}} \approx -\frac{1}{2\pi\rho_0 h_0}\frac{\eta_2}{\delta_2} \tag{2.9a}$$

$$\Delta D_n^{\text{solvent}} \approx \frac{1}{\pi n f_0 \rho_0 h_0}\frac{\eta_2}{\delta_2}. \tag{2.9b}$$

The subscript 2 now refers to the water or D_2O in the absence of any leucine. Our reported data, and subsequent modelling of the viscoelastic properties of the adsorbed layer, is then represented by

$$\Delta f_n = \Delta f_n^{\text{soln}} - \Delta f_n^{\text{solvent}} \tag{2.10a}$$

$$\Delta D_n = \Delta D_n^{\text{soln}} - \Delta D_n^{\text{solvent}}. \tag{2.10b}$$

QCM-D experiments were performed with temperature-controlled sensor chambers (Q-Sense, Gothenburg, Sweden) and a peristaltic pump, in order to maintain a constant temperature of 23 ± 0.02 °C and 0.1 mL/min flow rate. Polystyrene-coated quartz crystal sensors of 0.3 mm thickness and 14 mm diameter were initially cleaned by rinsing and soaking with water, rinsing with ethanol, dried under nitrogen, and then plasma-cleaned for approximately 10 min. The pure solvents (H_2O and D_2O) were pumped through until each liquid filled the chamber, and then resonant frequencies of the fundamental and harmonics were measured in the presence of the solvent. Once a baseline was established after approximately 30 min, an unbuffered 0.17 M solution of L-leucine (Sigma Aldrich) in 18.2 MΩ·cm H_2O or D_2O (Sigma Aldrich) was flowed through the chamber. Frequency and dissipation versus time curves were collected. After Δf_n and ΔD_n reached a stationary state, pure solvent was used as a rinse to remove any leucine adhered reversibly to the sensor surface. The sensor chamber and pump tubes were cleaned between replicate experiments

by pumping a 2% Hellmanex solution (Sigma Aldrich Z805939) for 15 min, followed by 18.2 MΩ·cm H_2O for 15 min. For experiments using LB, the same procedure was followed, except 0.02 M NaCl was used to obtain a baseline before LB was flowed through the chamber, followed by rinsing with the NaCl solution in order to obtain the adsorbed mass.

2.5 Electrophoretic Light Scattering and Zeta Potential

Zeta potential is defined as the electrokinetic potential at the shear plane of the electrical double layer. The zeta potential at a solid–liquid interface depends on the ionic strength, ion valency, pH, and temperature of the suspending solution.[34] Thus, it is important to compare zeta potential measurements performed under similar solution conditions. Since it is not possible to probe the zeta potential directly, for particles in a liquid medium it is determined indirectly through electrokinetic measurements.

Electrophoresis refers to the movement of a charged surface relative to a stationary liquid under an applied electric field.[34] For spherical particles the velocity is given by

$$u_E = \mu_{\mathrm{EPM}} E \tag{2.11}$$

where μ_{EPM} is the electrophoretic mobility (EPM) of a particle in solution and can be determined using electrophoretic light scattering (ELS). This analytical technique is related to dynamic light scattering (DLS) and measures light scattered from dispersed particles moving in an electrolyte solution. Unlike DLS, which utilizes only random Brownian motion, in ELS an electric field (E) is applied that causes a directed motion of the particles based on their charge.[165] The frequency or phase shift—often termed phase analysis light scattering (PALS)—of an incident beam depends on the mobility of the particles. The relationship between the frequency shift and EPM depends on the scattering angle and the applied electric field.[165] Once the EPM is known, Eq. 1.1 can be used to calculate the zeta potential (ζ). This Helmholtz–Smoluchowski equation is suitable when the EDL is

thin relative to the particle's size (i.e. when $\kappa \gg 1$ where κ is the reciprocal of the Debye length). Since the Debye length in our experiments is on the order of 1 nm in 0.02 M NaCl, this equation holds true for our approximately 10 μm diameter spherical silica particles.

In ELS, particles are placed between two electrodes such that when an electric field is applied, the particles migrate toward the electrode of opposite charge and their velocities are measured. In PALS, as the applied field shifts between positive, zero, and negative values, the scattered light is collected and a fourier transform converts the signal into a frequency spectrum. Switching the direction of the electric field gives rise to synchronized phase changes; thus, the phase spectrum tracks the frequency shift. PALS uses this phase shift to calculate the mean electrophoretic mobility.[165] As a result, it is also more sensitive than the laser Doppler method.

For ELS experiments, the EPM was measured using a phase analysis light scattering (PALS) Zeta Potential Analyzer (ZetaPALS, Brookhaven Instruments, UK). In two separate experiments, a liquid culture of normal and CER-treated *E. coli* was prepared as per the cell culture procedures described in section 2.1. Both cultures were incubated with silica spheres (9-13 μm particle size, Sigma) overnight. The spheres were separated from planktonic stationary phase cells via centrifugation at 13.4 rpm (Eppendorf mini spin) followed by decanting of the supernatant. This was repeated until no planktonic bacteria remained, leaving only particles with adhered bacteria. The beads were washed with filtered 0.02 M NaCl (0.45 μm, cellulose acetate) three times and then suspended in the same 0.02 M NaCl to yield a 0.01% by volume solution. This solution was transferred to a clean cuvette fitted with a platinum electrode (AQ-1207, #24). The reported EPM values represent the average of ten successive runs (with 30 electric field-switching cycles per run). The zeta potential was calculated using the measured EPM and Eq. 1.1 (n=1.337; ε=80 F/m; η=0.893 Pa·s for 0.02 M NaCl) by the PALS Zeta Potential Analyzer software (Brookhaven Instruments, UK). The zeta potential of a 0.01 % by volume solution of pure silica beads was also measured after washing the beads five times in 18.2 MΩ·cm water

and suspending them in the same filtered 0.02 M NaCl.

2.6 White Light and Fluorescence Microscopy

Images of adhered *E. coli* were acquired using a Cytation5 Automated Microscope (BioTek, U.S.A.). For lag and exponential phase cells, a pre-culture of *E. coli* was diluted 1:100 by volume with fresh LB in a baffled 800 mL beaker and incubated at 37 °C while shaking at 200 rpm for 2.5 h. The beaker contained 11 piranha-cleaned (3:1 sulfuric acid and hydrogen peroxide) coverslips (22 mm × 30 mm No. 1.5, ThermoFisher) vertically mounted in a custom holder 3D-printed from polylactic acid. The glass substrates were mounted in this way so as to most closely match the prism geometry in our SFG experiments. Coverslips were removed at OD_{600} values of 0.03 (5 replicates) and 0.21 (6 replicates). Stationary phase cells were imaged using the prism at the end of each SFG experiment (10 replicates). Cells on all coverslips and prisms were dip-rinsed with deionized water, fixed with methanol, and stained with congo red (dye content $\geq$ 35%; Sigma) for at least 30 min. Congo red is a non-specific stain for polysaccharides, commonly used to visualize EPS.[123] For each coverslip and prism, approximately 24 tiles were imaged in brightfield mode to obtain the cell count, and using the Texas Red filter to obtain fluorescence images to determine EPS coverage. The same growth and imaging procedures were carried out for CER-treated cells.

Chapter 3

Characterization of the Silica–Water Interface[1]

3.1 Introduction

Fundamental studies of water next to model surfaces are important not only for understanding the neat water interfaces, but also for characterizing perturbations in the water structure upon addition of solutes. Thus, in order to understand the role of interfacial water on bacterial adhesion to silica surfaces, a clear picture of the neat silica–water interface is needed.

In biological media that contain an abundance of ionic species, an EDL exists around the cell membrane, as well as at the charged surface being adhered to.[133] Silica in particular is known to be sensitive to perturbations in the pH and ionic strength of the surrounding solution. Studies have shown that the presence of salt disrupts the interfacial water structure, with increasing salt concentration leading to a decrease in the number of ordered water molecules.[144] This is due to increased screening of the negative surface charge, thereby decreasing the electrostatic field aligning water dipoles, consistent with the EDL model. Sum frequency generation, with its inherent surface specificity, is well

[1]This was a collaborative project between our group and the Gibbs group at the University of Alberta. Akemi Darlington and M. Shafiul Azam performed some of the SFG experiments on a broadband SFG system; I performed analogous SFG experiments on our scanning picosecond system. Sandra Roy performed the electronic structure calculations and molecular dynamics simulations. Dennis Hore carried out the spectral modelling. I contributed to the data analysis and interpretation of the results.

suited to probe structured water in both the compact and diffuse layers of the EDL. Studies utilizing SFG to probe the silica–water interface have shown an ion identity-dependent structuring of interfacial water molecules.[25] However, the structure of water molecules in the Stern and diffuse layers adjacent to silica, and how they are affected by changes in salt concentration and pH, remain elusive.

SFG experiments at the silica–water interface while varying the pH and the ionic strength were carried out to better understand the relationship between surface charge density and high salt concentration on the structure of the EDL. By keeping the sodium chloride concentration at 100 mM or above, the compact (Stern) layer of the EDL was kept intact with a Debye length less than 1 nm.[21]

3.2 Results and Discussion

3.2.1 Density and Structure of Interfacial Water Molecules

It has been established that the nature of the solution environment (temperature, pH, ionic strength) has consequences on the bulk solubility and three-dimensional structure of solutes.[166] In the bulk, each water molecule makes on average 3.6 hydrogen bonds with other water molecules.[167] It is this dynamic network of hydrogen bonds that gives water its unique chemical and physical properties, and in turn affects the solute environment. When it comes to studying molecules at surfaces, it therefore makes sense to start with an investigation of the solvent environment at those surfaces. Fig. 3.1a illustrates the density and (Fig. 3.1b) tilt order parameter (degree of orientation of the molecule's C_{2v} axis with respect to the surface normal) as a function of distance from a model hydrophobic and hydrophilic surface (full details in Ref. 168). For a hydrophobic surface, a monotonic increase in water density is observed in moving towards the bulk water phase, with an orientation distribution that becomes isotropic after about 1 nm or 2–3 molecular layers. For water adjacent to a hydrophilic (OH-terminated surface), the density oscillates about the bulk value, and the accompanying orientation profile is much more complex. It should

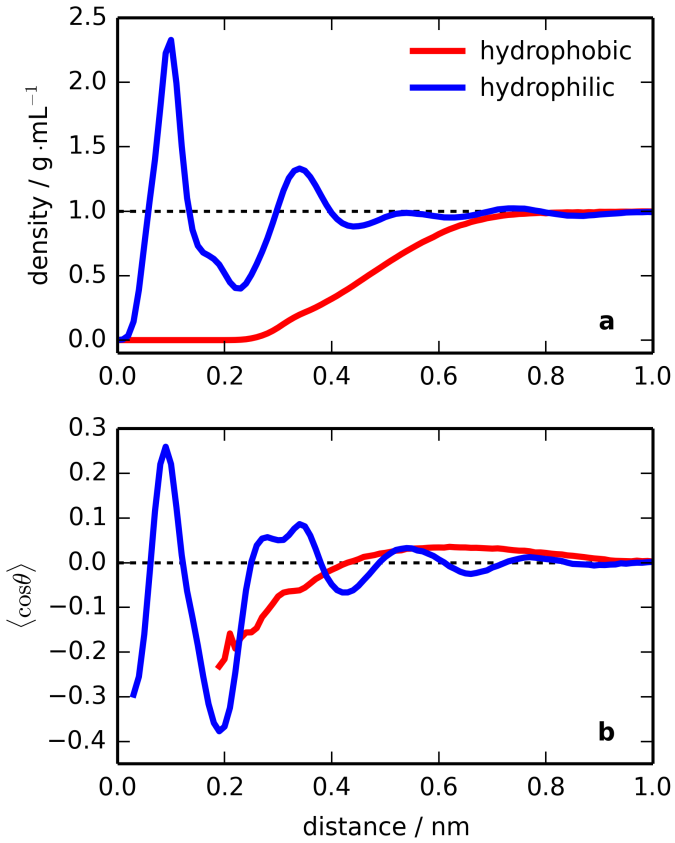

Figure 3.1: (a) Density and (b) average value of the tilt angle $\langle \cos\theta \rangle$ for water molecules adjacent to a hydrophobic (red) and hydrophilic (blue) surface. Adapted from Ref. 168. Copyright 2012 American Chemical Society.

be noted that the fine details of the results are dependent on the choice of interaction potential. In particular, the width of the hydrophobic water depletion region for simple models tends to be slightly larger than what would be obtained for more realistic surfaces. However, the distinguishing features of hydrophilic and hydrophobic surfaces remain apparent.

Fig. 3.2 illustrates example SFG spectra as collected from a hydrophobic (air) and hydrophilic (glass) surface, superimposed on the IR absorption spectra of bulk water and ice. One can see that the 3.6 hydrogen bonds per molecule in the bulk liquid takes the form of a wide distribution of hydrogen bonding environments, with a peak intensity near 3400 cm^{-1}. Ice has a tetrahedral structure, and correspondingly the absorption maximum

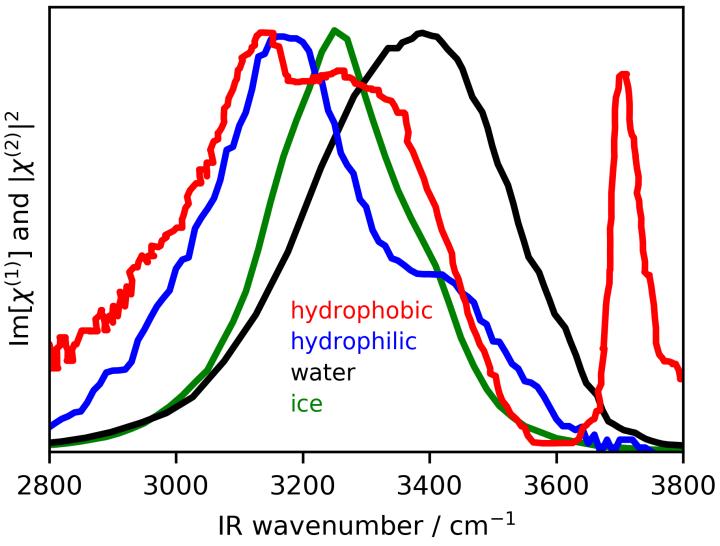

Figure 3.2: Im[$\chi^{(1)}$] for water (black)[171] and ice (green),[172] superimposed on $|\chi^{(2)}|^2$ for water at a hydrophobic (red)[5] and hydrophilic (blue)[173] surface. All spectra have been normalized to their highest intensity in this wavelength region in order to facilitate comparison of their shapes. Reprinted with permission from Ref. 57. Copyright 2018 American Chemical Society.

is shifted to approximately 3200 cm^{-1}. SFG spectra of the hydrophobic and hydrophilic surfaces reveal the complexity of the interfacial hydrogen bonding environments, and the drastic differences between the two surfaces. This is a consequence of the substantial difference in density and orientation, as revealed in MD simulations.[57] Water next to the hydrophilic surface exhibits significant intensity at 3200 and 3400 cm^{-1}, and the relative intensity of these O–H stretching bands is sensitive to the detailed surface characteristics.[169] At the hydrophobic surface, a sharp feature near 3700 cm^{-1} originates from uncoupled OH oscillators: water molecules with one OH bond directed towards a surface with no opportunity for hydrogen bonding.[63,170]

3.2.2 pH Variation Experiments at Different NaCl Concentrations

When sodium chloride is present in solution at a concentration above 100 mM, the compact part of the EDL is present. The SFG spectra of 500 mM NaCl as a function of pH are shown in Fig. 3.3A. There is a non-monotonic increase in intensity with a minimum intensity

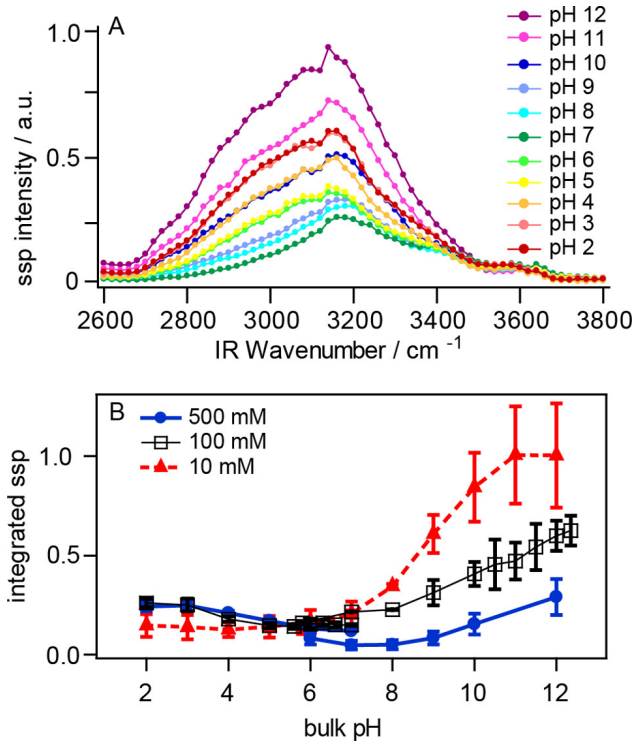

Figure 3.3: (A) Representative scanning SFG titration of the silica–aqueous interface in 500 mM NaCl. (B) Average integrated broadband SFG intensity as a function of pH in 500 (blue circles), 100 (black squares), and 10 mM (red triangles) NaCl. Error bars are the standard deviation from two or more experiments. Reprinted with permission from Ref. 21. Copyright 2017 American Chemical Society.

observed at pH $\sim$ 7. The same trend is observed at 100 mM salt concentration, although the minimum shifts to pH $\sim$ 5 (Fig. 3.3B). This is in contrast to previous SFG experiments performed at lower salt concentrations, which observed a minimum intensity at the point-of-zero charge of silica (pzc between 2 and 3).[21] To test if this is due to a lower salt concentration, we performed the same SFG experiment using 10 mM NaCl. As seen in Fig. 3.3B, the minimum in intensity again shifts to a lower pH value. In addition, at pH values above 8, we observe that SFG intensities increase with decreasing salt concentration. This is consistent with greater screening of the negative surface charge on silica by sodium cations at greater salt concentrations and has been observed in previous SFG studies.[144] However, at low pH, the 100 and 500 mM spectra both had greater intensity than the 10 mM case.

To elucidate whether this unexpected pH-dependent behaviour is a result of the average orientation of water molecules, we collected spectra using a pss polarization combination, which probes a different $\chi^{(2)}$ tensor element. This is shown in Fig. 3.4B where a monotonic increase in intensity with pH is clearly observed. This is in contrast to the trend in ssp (Fig. 3.4A) and ppp (Fig. 3.4C) spectra in which there is first a decrease and then increase in intensity with increasing pH. Moreover, the shape of pss spectra are different than ssp spectra: the former is dominated by the 3400 cm^{-1} mode while the latter by the 3200 cm^{-1} mode. Since the evolution of these two bands with pH is quite different, it is possible that the two distinct water populations responsible for these modes are changing orientation differently.

3.2.3 SFG Spectral Simulations

To test whether systematic changes in tilt angle could account for the pH-dependent behaviour, we simulated SFG spectral intensity as a function of the water molecule orientation (Fig. 3.5). This simulation requires knowledge of the vibrational hyperpolarizability, $\alpha^{(2)}$. Since we are dealing with condensed phase water, such information is not as readily accessible due to the intramolecular coupling being sensitive to the hydrogen-bonding environment at the surface. As mentioned, the spectral intensity at 3200 and 3400 cm^{-1} has contributions from many types of OH oscillators, including modes that are coupled and those that are uncoupled. We have addressed this by performing molecular dynamics simulations of water next to a model hydrophilic interface, which allows us to capture all of the different species as well as coupled modes contributing to these two spectral regions.

As shown in Fig. 3.6A and B, the ssp and pss intensity as a function of the water tilt and twist angles for the 3200 cm^{-1} mode are nearly anticorrelated, such that orientations that yield significant ssp signal at 3200 cm^{-1} lead to no pss signal. Hence it is likely that the waters corresponding to the 3200 cm^{-1} mode are oriented such that they are not probed by the pss polarization combination. In contrast, the ssp and pss intensity

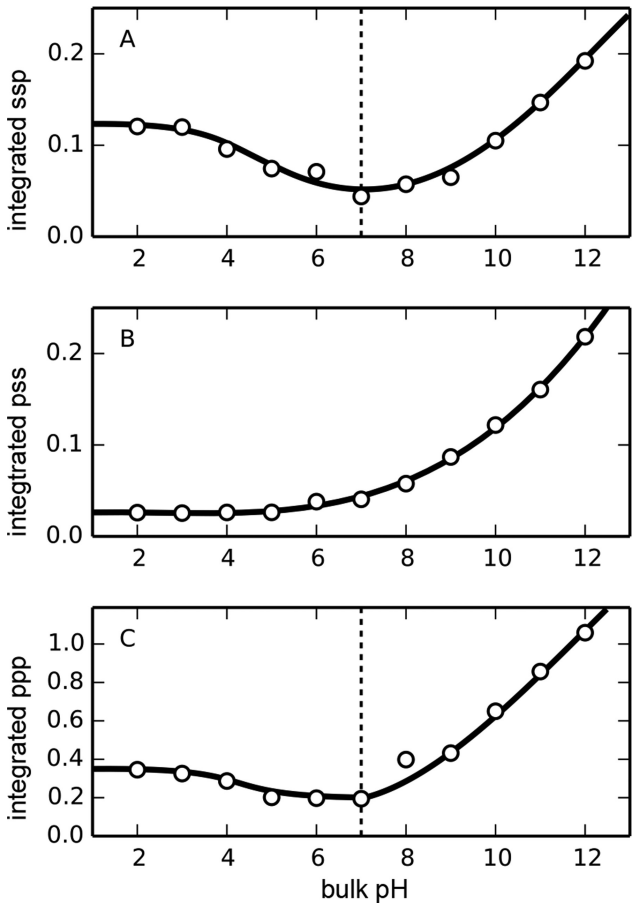

Figure 3.4: Integrated SFG intensity of all 500 mM titrations using (A) ssp, (B) pss, and (C) ppp polarization combinations. Reprinted with permission from Ref. 21. Copyright 2017 American Chemical Society.

maps of the 3400 cm^{-1} mode (Fig. 3.6D and E) are not mutually exclusive, so there are multiple orientations that lead to signal intensity in both polarization combinations. This is consistent with the appearance of the 3400^{-1} mode in both ssp and pss spectra, although the former is dominated by the 3200 cm^{-1} mode.

The minimum in SFG intensity in ssp and ppp spectra is suggestive of a flip in the water molecule orientation as a function of pH, which in this reorientation model would involve a tilt angle change that passes through $\theta = 90^{\circ}$. Therefore, we asked, within the constraints of this model, could the same change in orientation for the two different populations explain the pH-dependent trends for the different polarization combinations? If the differences observed cannot be attributed to the same change in twist and tilt angles, then it provides

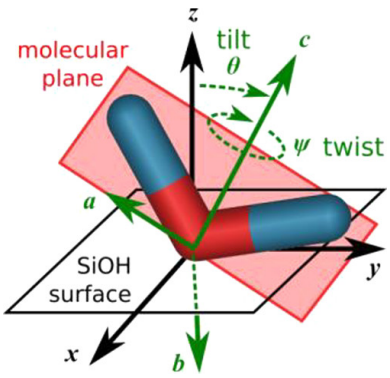

Figure 3.5: Illustration of the water molecule orientation with respect to the (x,y) plane of the surface, where z is the outward-facing surface normal, pointing into the bulk water solution. The tilt angle θ is defined with respect to the H–O–H bisector and the molecular symmetry axis, c (θ is the angle between c and z). The twist angle (ψ) represents the rotation about c. Reprinted with permission from Ref. 21. Copyright 2017 American Chemical Society.

evidence that the two modes (3200 cm^{-1} and 3400 cm^{-1}) are experiencing different orienting forces such that each water population is being ordered to a different extent or oriented in a different direction. From the simulations we see that for water molecules in the 3200 cm^{-1} region, the ssp and ppp polarized spectra show similar trends for a given set of orientations (Fig. 3.4A and C). Moreover, for twist angles between 90 and 140° and an initial tilt angle of $\sim 40°$, there is a continual decrease in spectral intensity for ssp and ppp with increasing tilt angle, until a minimum is reached, followed by an even greater increase in intensity. This nonmonotonic change in spectral intensity as a function of tilt angle is consistent with the ssp and ppp experimental spectra at high salt concentrations, which also show a decrease then increase in spectral intensity with increasing pH. Accordingly, the trend in the ssp and ppp experimental spectra could be explained by a small initial tilt angle of these water molecules, which then increases systematically with pH such that a flip in orientation is observed (i.e. the tilt angle increases beyond 90°). Since the pss spectra are not sensitive to the 3200 cm^{-1} mode, the relatively constant intensity observed at these twist angles is also consistent with the data (Fig. 3.4B).

For the 3400 cm^{-1} mode, the pss polarization scheme is the most sensitive probe

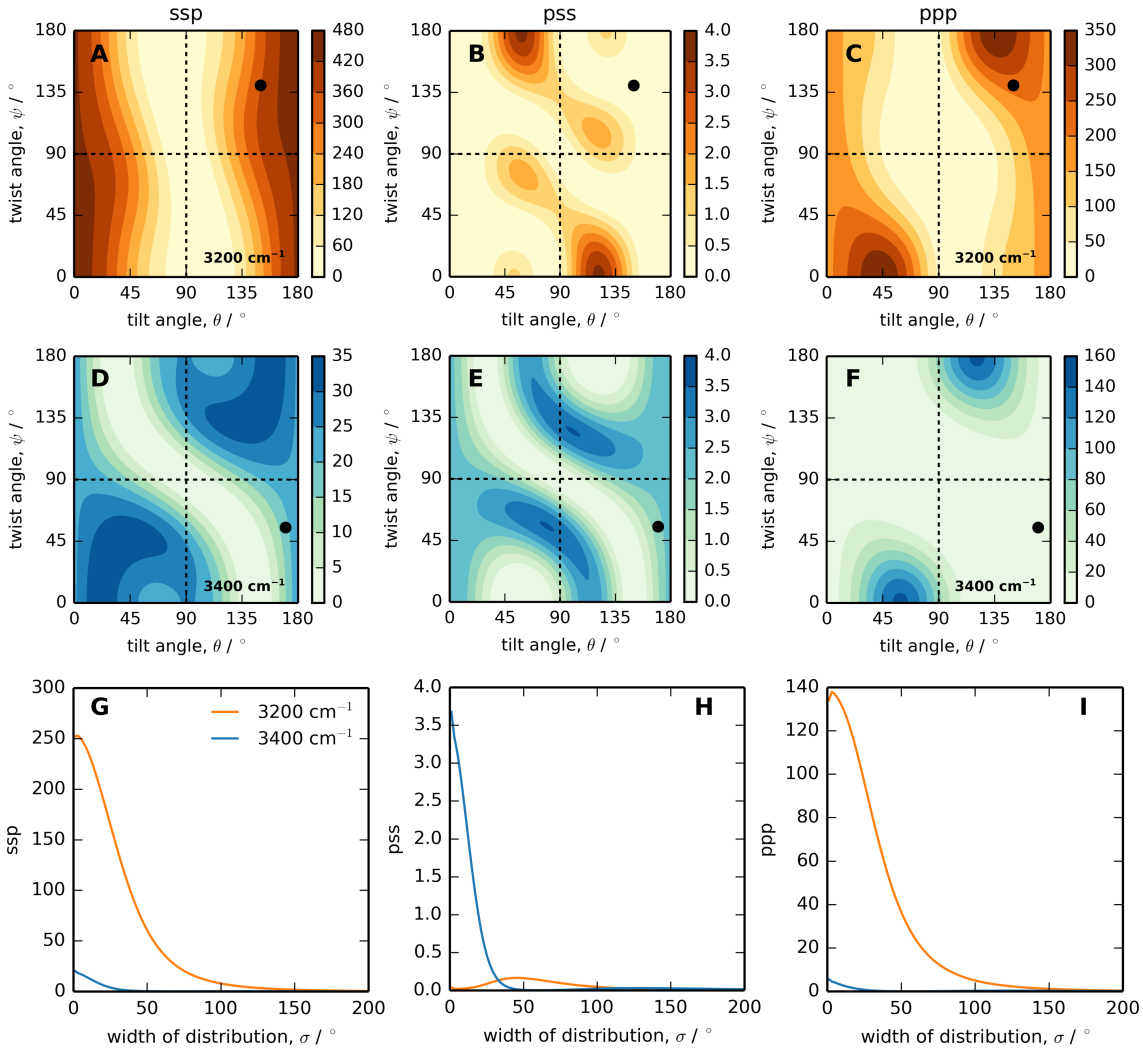

Figure 3.6: Predicted SFG intensity for water next to an OH-terminated surface in the (A) ssp, (B) pss, and (C) ppp polarizations for the mode at 3200 cm^{-1} as a function of the molecules tilt and twist angles (as illustrated in Fig. 3.5), assuming a narrow distribution about these angles. For a 3400 cm^{-1} water species, the results of these same polarizations are shown in panels D–F. Considering a ($\theta = 150°$, $\psi = 140°$) orientation for the 3200 cm^{-1} species (as indicated by the black dot in the top row, which corresponds to θ, ψ at pH 12) and a ($\theta = 170°$, $\psi = 55°$) orientation for the 3400 cm^{-1} species (black dot in the middle row), we can predict the variation in SFG intensity as the width of the tilt and twist angle distributions (assumed to be the same) increases. This is shown in the bottom row (panels G–I). Reprinted with permission from Ref. 21. Copyright 2017 American Chemical Society.

as it nearly excludes the 3200 cm^{-1} water population. Thus, we examined our water orientation model to determine if the same changes in orientation of the 3400 cm^{-1} water are consistent with increasing SFG intensity with increasing pH. However, there are no twist angles that lead to a systematic increase in intensity upon changing the tilt angle through 90°, consistent with a flip in orientation. Instead, for the mode at 3400 cm^{-1}, assuming a twist angle between 45° and 55°, a systematic increase in the tilt angle from $\sim$ 140° toward 180° would result in an increase in intensity with increasing pH. These tilt and twist angle combinations were chosen based on similar (within 10°) values reported in previous experimental data at fused silica and MD simulations of water adjacent to a hydrophilic solid surface at increasing distance from the interface.[144] This change is consistent with the molecular coordinate system (Fig. 3.5) and an increasingly negative surface charge with increasing pH because increases in θ beyond 90° correspond to the hydrogen atoms becoming more aligned at the surface. From this comparison we conclude that the orienting forces felt by each water population are very different. Moreover, if the changes in SFG intensity are due to changes in the average tilt angle, then the results suggest the water populations that correspond to the 3200 cm^{-1} mode are flipping their orientation upon increasing the pH from pH 2 to 12, whereas those water molecules that correspond to the 3400 cm^{-1} mode are not.

In the above model, we have considered a narrow distribution of tilt and twist angles. In reality, these distributions have some width, and it is also likely that the width could change as the interfacial environment changes. We now explore this scenario, where the flipping of water in the diffuse layer is accomplished by a widening of the orientation distribution until the point where it is isotropic when the potential reaches zero, followed by a renarrowing of the distribution (but with opposite orientation) as the potential increases again with increasing pH but with opposite sign. Fig. 3.4G and I illustrates that for the 3200 cm^{-1} species at a tilt angle of 150° and a twist angle of 140°, the intensity decreases as the width distribution (σ) increases. This is also consistent with trends in the experimental

spectra if the width distribution increases from $\sim 45^{\circ}$ with increasing pH until a minimum is reached, at which point water molecules in the diffuse layer flip, and the intensity again increases but with decreasing σ values, reaching a maximum near zero distribution. For the 3400 cm^{-1} species at a tilt angle of 170° and a twist angle of 55°, the intensity increases with decreasing σ values, reaching maximum intensity at zero width distribution. This is consistent with the monotonic increase in intensity observed in the pss spectra if the width distribution decreases from $\sim 30^{\circ}$ toward 0°. Finally, it is worth noting that the plots in Fig. 3.4G–I are consistent with the dominance of the 3200 versus 3400 cm^{-1} species seen in the experimental SFG data: in the ssp and ppp polarizations, the 3200 cm^{-1} species has significantly greater intensity than the 3400 cm^{-1} species, while in the pss scheme, the 3400 cm^{-1} species clearly dominates.

Previous work has shown that the 3200 cm^{-1} peak corresponds predominantly to water molecules farther from the surface (in the diffuse layer) while the 3400 cm^{-1} peak corresponds to water molecules located closer to the surface, since the former showed a greater salt dependence.[32,144] In light of this, we propose two scenarios that could account for diffuse layer water (contributing to the 3200 cm^{-1} mode) flipping with increasing pH while water closer to the surface (contributing to the 3400 cm^{-1} mode) does not.

3.2.4 Scenario 1: Overcharging of the EDL

In this scenario, at low pH, overcharging of the Stern layer can occur when there are more cations in this layer than there are negative surface sites on silica, causing the Stern layer to have a positive potential, while the surface maintains its negative potential. Since these two potentials are opposite in sign, they would align the two distinct water populations (through the $\chi^{(3)}$ term) in opposite directions (see Fig. 3.7A). As the pH is increased, deprotonation of surface silanols leads to an increase in the negative surface charge. Eventually, the Stern layer potential (at the OHP) would equal zero, causing little order in the diffuse layer but significant ordering of Stern layer waters. As the pH is increased further, negative

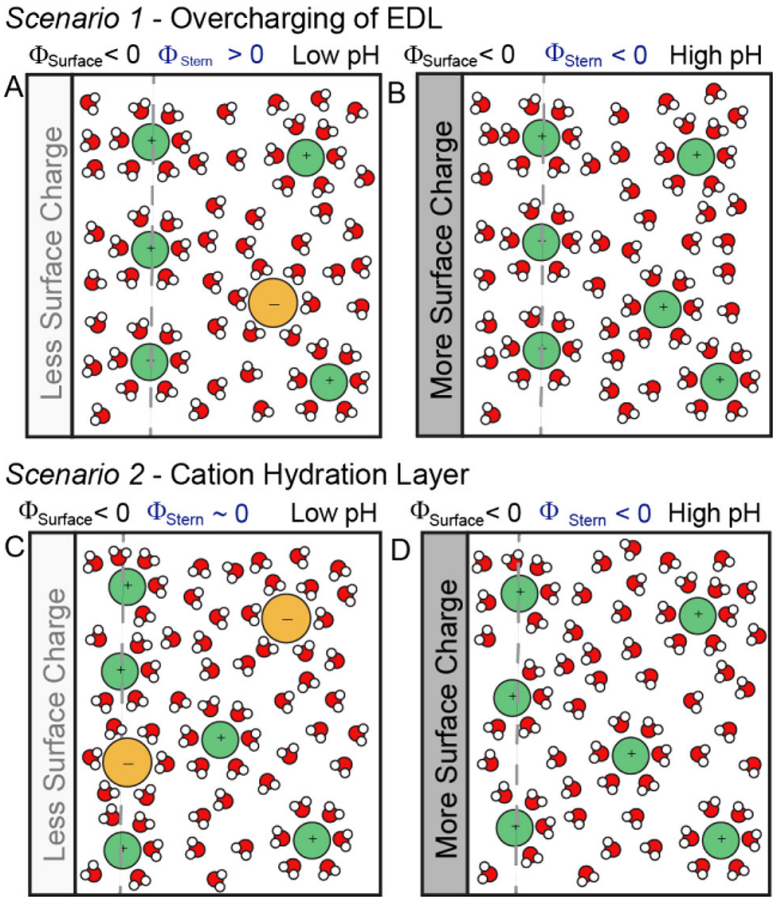

Figure 3.7: Scenario 1 involves overcharging of the EDL at low pH (A) and high pH (B). Scenario 2 depicts the cation hydration layer contributing to the SFG at low pH (C) while the diffuse layer contributes at high pH (D). Reprinted with permission from Ref. 21. Copyright 2017 American Chemical Society.

surface sites would dominate leading to negative potentials for both the surface and Stern layer. Thus, both water populations would be oriented in the same direction (Fig. 3.7B). This is consistent with the shift in the ssp/ppp SFG minimum with pH at higher salt concentrations, as having more ions in solution would require a larger pH to reach the pzc. The interactions described by the $\chi^{(3)}$ term assume the potentials acting on the water in the Stern layer or diffuse layer lead to alignment of the dipole moment of water with the surface normal (corresponding to a tilt angle of 0 or 180° depending on the sign of the potential). Accordingly, this overcharging scenario is consistent with the molecular model proposed above. For the waters contributing at 3200 cm^{-1}, the assembly begins with a tilt

angle nearer 0° at low pH owing to the positive Stern layer potential. This corresponds to the oxygen atoms pointing toward the surface (refer to Fig. 3.5). The tilt angle then systematically increases with increasing pH until it passes through 90° (corresponding to a zero Stern layer potential) and then approaches 180° at higher pH when the Stern layer potential is large in magnitude and negative. As a result of this flip in orientation, the hydrogen atoms are instead pointed toward the surface, which is consistent with the increased negative charge on the silica surface at high pH. In contrast, for 3400 cm^{-1} waters, the dipole moment becomes more aligned with the surface normal with increasing pH as the surface potential goes from zero to large negative values, consistent with the systematic increase in the tilt angle with pH above 90° toward 180°. This means that water molecules closer to the interface have their oxygen atoms pointing away from the surface at low pH.

3.2.5 Scenario 2: Cation Hydration Layer

In this scenario, if sodium cations specifically adsorb to silica, then distortion of their hydration shell could result in those water molecules contributing to the $\chi^{(2)}$ signal, due to their lack of centrosymmetry. This could result either from partial dehydration upon adsorption or as a result of hydrogen bonding between hydration waters and the surface.[23] As a result, these hydration waters would be mainly oriented with their oxygen atoms pointing toward the surface. Water in the sodium hydration sphere resonates at 3150 cm^{-1} and contributes to the $\chi^{(2)}$ term, which interferes with the $\chi^{(3)}$ response of water in the diffuse layer, polarized by the Stern layer potential (Φ_{Stern}).[174] This results in a cancellation of the overall SFG signal. The minimum in the SFG intensity would then correspond to the pH where the most cancellation between hydration and diffuse layer waters occurs. As the pH is decreased, the Stern layer potential becomes smaller and so waters in the hydration shell start to dominate the SFG signal, leading to an increase in intensity (Fig. 3.7C). At higher pH, the greater magnitude of the negative surface and Stern potentials is able to

align more waters in the diffuse layer, which now dominate the signal over the hydration shell waters. This would again lead to an overall increase in SFG intensity with increasing pH (Fig. 3.7D). As in scenario 1, the pH value where the minimum occurs is dependent on electrolyte concentration since a higher concentration leads to a compression of the diffuse layer. Thus, optimal cancellation of the two water populations (hydrated cations and diffuse layer) would shift to higher pH with increasing salt concentration.

It may be that both scenarios contribute to the observed trends in SFG. The fact that there is still signal intensity at 3200 cm^{-1} at the minimum in ssp and ppp spectra indicates that there is some structured water at all pH values, even when the Stern potential is zero. However, both scenarios suggest water molecules contributing to the 3200 cm^{-1} mode flip orientation. This is confirmed by phase-sensitive SFG studies at silica–water, which also revealed a flip in orientation only for waters contributing to the low wavenumber region.[175,176]

3.3 Conclusions

The SFG data revealed two different populations of water molecules within the electrical double layer that exhibit pH dependent behaviour when a Stern layer is present. By varying the polarization combination of the incoming visible and IR beams, as well as the outgoing SFG beam, it was seen that the ssp/ppp combinations were sensitive to water molecules contributing to the 3200 cm^{-1} peak in the spectrum, located further from the surface in the diffuse layer, while the pss polarization combination probed water molecules near the surface in the Stern layer, contributing to the 3400 cm^{-1} peak. For water molecules adjacent to the surface, a continual increase in alignment of water molecules was observed as the pH was increased from the point-of-zero charge of silica (pH 2) to pH 12, consistent with a more negative surface charge with increasing pH. However, waters further from the surface appear to undergo a flip in orientation as the pH is increased over the same range, which is attributed to the presence of a Stern layer and overcharging of the EDL

with sodium cations at lower pH values.

These results have a significant impact on previous interpretations of high electrolyte concentration data in nonlinear optical experiments because they reinforce that different water populations can reside in very different proximity to the surface. They also show the importance of the structure of the EDL—specifically whether or not a Stern layer is present—on the local environment experienced by different populations of water molecules. These differing local environments would in turn influence the manner in which other molecules adhere to silica surfaces in particular, including biomolecules and cells.

Chapter 4

Water as a Reporter of Surface Conditions during Bacterial Adhesion to Silica

4.1 Introduction

It is increasingly recognized that early protein conditioning and cell–surface interactions are prerequisites to the attachment of bacteria and formation of biofilms. Although scientists have amassed considerable knowledge of the growth, composition, and structure of mature biofilms,[177–179] the details of such a conditioning layer and early bacterial adsorption are not clear.[77,84,180–183] The role of the interfacial environment, including water structure, pH, and ionic strength, on initial bacterial adsorption and aggregation are acknowledged as being critical factors, yet remain largely unknown.[184–186] This is partly owing to the complexity of the interfacial environment (surface roughness, charge, hydrophobicity; solution ionic strength, pH, composition of osmolytes), and partly a result of the paucity of in situ, label-free techniques that can probe the interfacial environment with sufficient selectivity and structural sensitivity. The physical and chemical nature of the substrate, and hence conditioned surface, including the structure of interfacial water molecules and the role of ions, are key aspects that need to be better understood.[187,188] Thus, a more sensitive and surface-specific technique, capable of in situ characterization of the solid–aqueous interface is needed. Among the probes available for surface analysis,

visible–infrared sum frequency generation (SFG) spectroscopy is unique in its ability to provide quantitative molecular level information at buried interfaces with extreme surface-specificity.[189–192] This is a result of the second-order nonlinear susceptibility tensor $\chi^{(2)}$ vanishing in centrosymmetric materials, such as the bulk solution phase. Therefore, this second-order nonlinear vibrational technique is ideal for monitoring alterations in surface-bound water structure, in order to serve as a predictor for interfacial environmental conditions that lead to adhesion.

Here, we use SFG spectroscopy, in combination with imaging and solution characterization techniques, to monitor how early protein conditioning and *E. Coli* adhesion influence the interfacial environment at silica surfaces. We illustrate that SFG spectroscopy is a sensitive probe of the local ionic strength, which is reduced as a result of ion adsorption by EPS, and local pH, which is increased as a result of metabolic activities of bacteria at the surface.

4.2 Results

4.2.1 SFG Response to Online versus Offline Growth Conditions

The population of *E. coli* was monitored by measuring the optical density at 600 nm. As shown in Fig. 4.1a (points), this followed a logarithmic behaviour, enabling the data to be fit by

$$f(t) = \frac{A}{1 + e^{-k(t-t_m)}} + b \tag{4.1}$$

where A is the amplitude, k is the growth rate, t_m is the mid-point of the exponential phase, and b is any offset. Fitting the data to this equation resulted in $k = 0.87$ h^{-1} and $t_m = 8.1$ h, as indicated by the line in Fig. 4.1a. Based on this data, we consider the lag phase to exist up to 4 h, the exponential phase from 4–15 h, and the stationary phase after 15 h. We refer to this as the offline growth, as no vibrational spectra were recorded during this period.

We then perform the same experiment, but inside the thermostated sample chamber of our SFG spectrometer, referred to as online growth. The intensity of the SFG signal

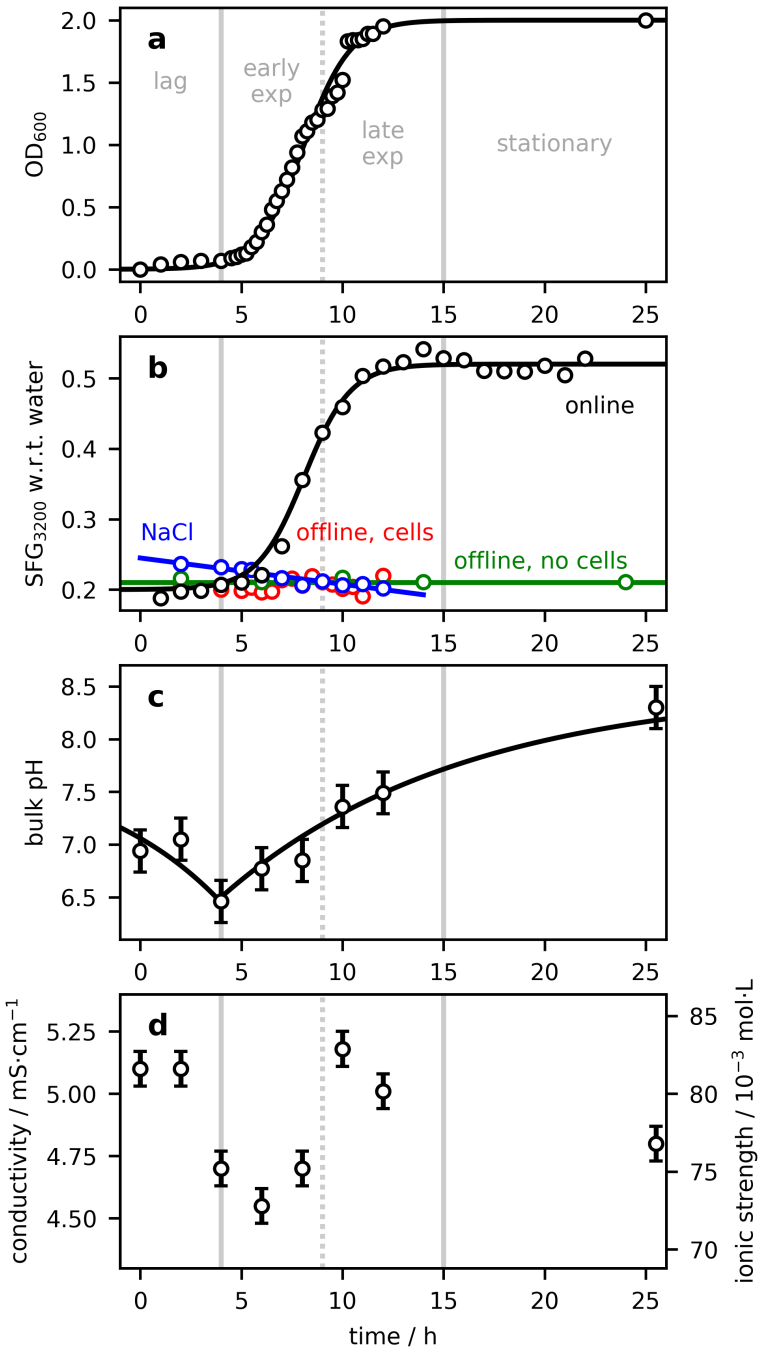

Figure 4.1: (a) *E. Coli* K12 growth curve as determined from the optical density at 600 nm (points) and fit to the model in Eq. 4.1 (line); (b) online growth SFG intensity (black points) at 3200 cm^{-1} with respect to the neat water–silica interface, superimposed on the same growth model (black line); signal from cells grown offline (red) followed by centrifuged fractions (green); 0.08 M NaCl rinse (blue); (c) bulk solution pH; (d) bulk solution conductivity. Reprinted with permission from Ref. 173. Copyright 2018 American Institute of Physics.

is proportional to the square of the sum of second- and third-order contributions to the polarization. As we are in the ssp polarization scheme, we probe only a single element of $\chi^{(2)}$ and $\chi^{(3)}$,

$$\begin{aligned} I_{\mathrm{ssp}} &= |P^{(2)} + P^{(3)}|^2 \\ &= \left| L_y L_y L_z \chi^{(2)}_{yyz} E_{\mathrm{vis}} E_{\mathrm{IR}} + L_y L_y L_z \int_0^{\infty} \chi^{(3)}_{yyzz} E_{\mathrm{vis}} E_{\mathrm{IR}} E_0(z)\, dz \right|^2 \end{aligned} \tag{4.2}$$

where E_{vis} and E_{IR} are the electric components of the fields from the laser approaching the sample, and $E_0(z)$ is the distance-dependent static field originating at the silica surface. The integration in Eq. 4.2 results in an interference between the $\chi^{(2)}$ and $\chi^{(3)}$ terms that is modulated by the ionic strength and wavevector mismatch.[193,194] The local field correction factors L provide the laser fields at the silica–aqueous interface, and are calculated according to the refractive index and beam angles.[195] As we will describe later, these factors are especially important when near the critical angle, as small changes in the refractive index can have a marked effect on the SFG signal.

As shown in Fig. 4.2, we first collect the signal of water adjacent to silica from 2800–3550 cm^{-1} (blue trace), corresponding to the O–H stretching vibration. We then remove the water and fill the chamber with fresh LB growth medium. The resulting spectrum (red trace) shows essentially the same shape, but with only 21% of the intensity. For all subsequent SFG data, we will display the intensity relative to that of water at 3200 cm^{-1}. When the LB is now replaced with growth media that is inoculated with cells, spectra obtained (grey traces) for the first few hours have the same shape and intensity as the initial LB spectrum. After some time, however, the spectra increase, and then reach a plateau. The trends in this data are more clearly observed in Fig. 4.1b, as the points display a logarithmic growth. The line is a plot of Eq. 4.1, with the same values of k and t_m as were obtained for the OD_{600} data. Here only A and b have been adjusted to match the scale of the SFG data, normalized with respect to the water signal. It is curious that the signal increases to such a large extent (more than 250%), and that the trend so closely matches the population growth curve. In order to further investigate the origins of this effect, we

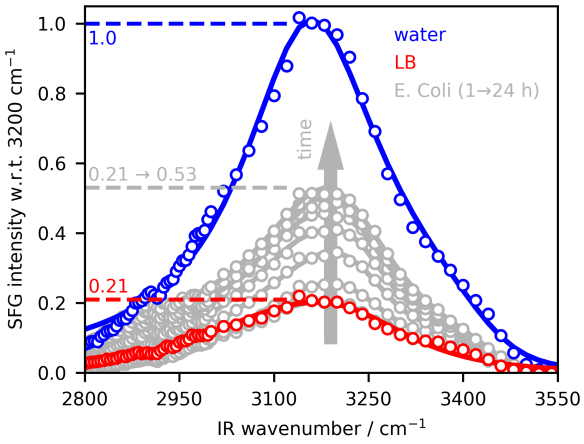

Figure 4.2: SFG spectra collected at the aqueous-silica interface for water (blue), LB growth medium (red), and *E. Coli* K12 (grey). During the bacteria growth, SFG intensity increases from 21% of the initial silica-water signal to 53% of this level. The intensity at 3200 cm^{-1} is plotted in Fig. 4.1b (black points). Reprinted with permission from Ref. 173. Copyright 2018 American Institute of Physics.

perform a separate experiment in which fractions of the population (as monitored in an OD_{600} measurement) are isolated, centrifuged and filtered to remove the cells, and then introduced to the SFG spectrometer. We have selected one snapshot from the lag phase, one from early and two from late exponential phase, and one from the stationary phase. As shown in Fig. 4.1b (green points), all fractions have the same SFG response throughout the lag, exponential, and stationary phases, with no increase observed. As it would appear that the dramatic difference between these two data sets may be the result of the cells being present, a final experiment studied the collected fractions without separating the cells and introduced them into the SFG spectrometer. The data (red points in Fig. 4.1b) shows only small changes in SFG signal intensity throughout each phase of growth, indicating that there is little difference between the presence and absence of cells in the offline SFG data.

We then investigate whether the increase in signal for online growth is due to the change in composition of the surface or bulk environments, or whether it has its own time dependence. We return to the centrifuged fractions, and introduce them in succession onto clean silica surfaces. Before the introduction of the solution, the water signal is measured

as a reference, and the surface is then pre-conditioned with LB. We have confirmed that the LB signal does not change with time, even over a 24 h period (Fig. 4.3b). The signal obtained from each fraction is then monitored for 4 h, as shown in Fig. 4.3a. Consistent with the data shown in Fig. 4.1b (green points), the SFG signal corresponding to the initial exposure to the solutions is fairly constant at 21% of the water value. Here it is noted that, as in the case of LB, there is also no change over time throughout the lag and exponential phases. However, the late exponential 14 h fraction ($OD_{600} = 1.76$) exhibits a more than 50% increase in signal over the 4 h monitoring period. Further into the stationary phase, the signal also increases with time, but to a lesser extent. It can also be seen in Fig. 4.3a that the 25 h fractions grown both on- and offline show identical increases over the 4 h period, reaching a plateau at the same time and intensity. However, a repeat experiment using a different, centrifuged 14 h fraction collected and treated in the same manner, but from a different *E. Coli* culture, showed no increase in SFG intensity over a 6 h period (Fig. 4.4).

4.2.2 Solution Conditions during Cell Growth

The bulk pH and conductivity of the LB fractions after supporting varying amounts of *E. Coli* growth were measured, as shown in Fig. 4.1c and d respectively. Starting from a neutral pH of 7.0, the pH decreases to 6.5 by the end of the lag phase and then abruptly increases during the exponential phase, reaching a plateau at pH 8.4 in the stationary phase. The conductivity γ, however, remained relatively constant throughout the *E. Coli* growth phases, with the ionic strength varying by only 10%. As the major ions in the initial LB are Na^+ and Cl^-, we can estimate the ionic strength I assuming a 1:1 electrolyte from the linearized relationship,[196,197]

$$I = a\gamma \tag{4.3}$$

where $a = 16 \times 10^{-3}$ mol·cm·mS^{-1}·L^{-1}, I is in mol·L^{-1}, and γ is in mS·cm^{-1}. The results of this ionic strength estimation using Eq. 4.3 are shown on the right axis of Fig. 4.1d.

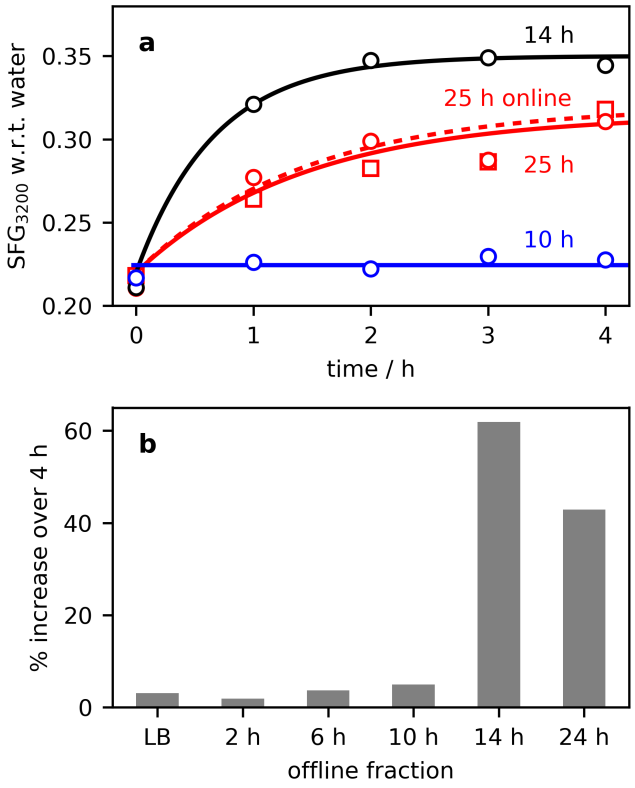

Figure 4.3: (a) Evolution of SFG signal at 3200 cm^{-1}, normalized with respect to the water–silica interface, for different centrifuged fractions collected during offline cell growth (circles). This displayed constant signal level over 4 h for all fractions up to 10 h, followed by exponential rise in SFG with time (solid lines) for the 14 h and 25 h fractions. For comparison, a 25 h fraction from online growth (squares, cells removed) was monitored and displayed the same exponential increase (dashed line). (b) The relative increase for the initial LB medium and all offline fractions. Reprinted with permission from Ref. 173. Copyright 2018 American Institute of Physics.

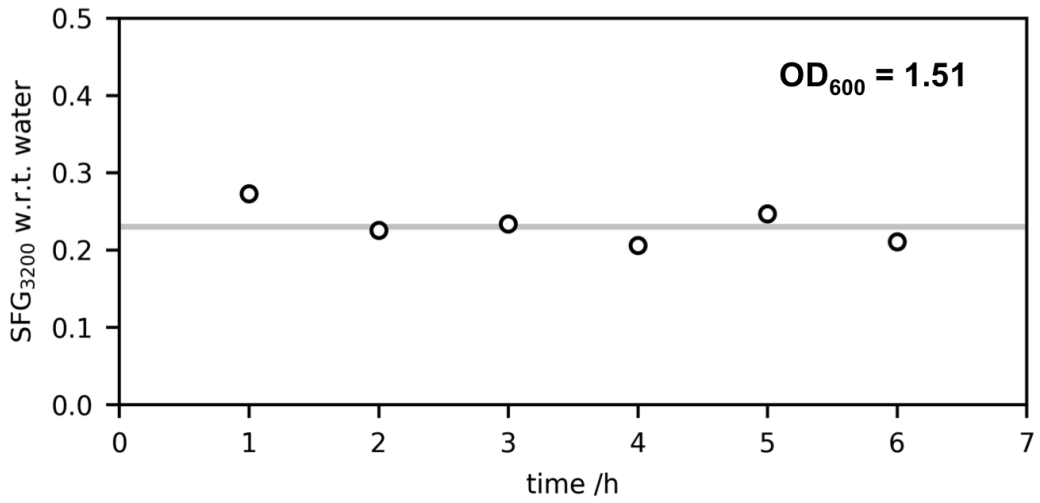

Figure 4.4: Evolution of SFG signal at 3200 cm^{-1}, normalized with respect to the water–silica interface, for a new 14 h centrifuged fraction ($OD_{600} = 1.51$), which displayed a constant signal level over a 6 h period.

4.2.3 Adherence and Surface Conditions during Cell Growth

Two representative images acquired after 24 h at 37 °C followed by rinsing and crystal violet staining are shown in Fig. 4.5a and b. The RGB color maps were flattened to create greyscale images, which were then further flattened to binary images (Fig. 4.5c and d) using an automatically-generated threshold value. This enabled counting of colonies and measuring their size distribution (Fig. 4.5e and f). We have determined that the average colony surface area was less than 5 μm^2, and the surface coverage was between 5–15%. We note that, in our SFG experiment the IR beam limits the probed area, and was focused to a diameter of approximately 500 μm, large on the scale of the heterogeneity of the adhered cell colonies. This accounts for the consistency in the trends observed for repeat SFG data. The experiments performed are probing relatively homogeneously colonized silica surfaces and the collected data reflects what is occurring when these cells and small colonies are present.

We are also interested in understanding the surface environment in the absence of cells, through pre-conditioning with LB and exposure to the growth medium over time. Although there are many techniques that are capable of characterizing the roughness

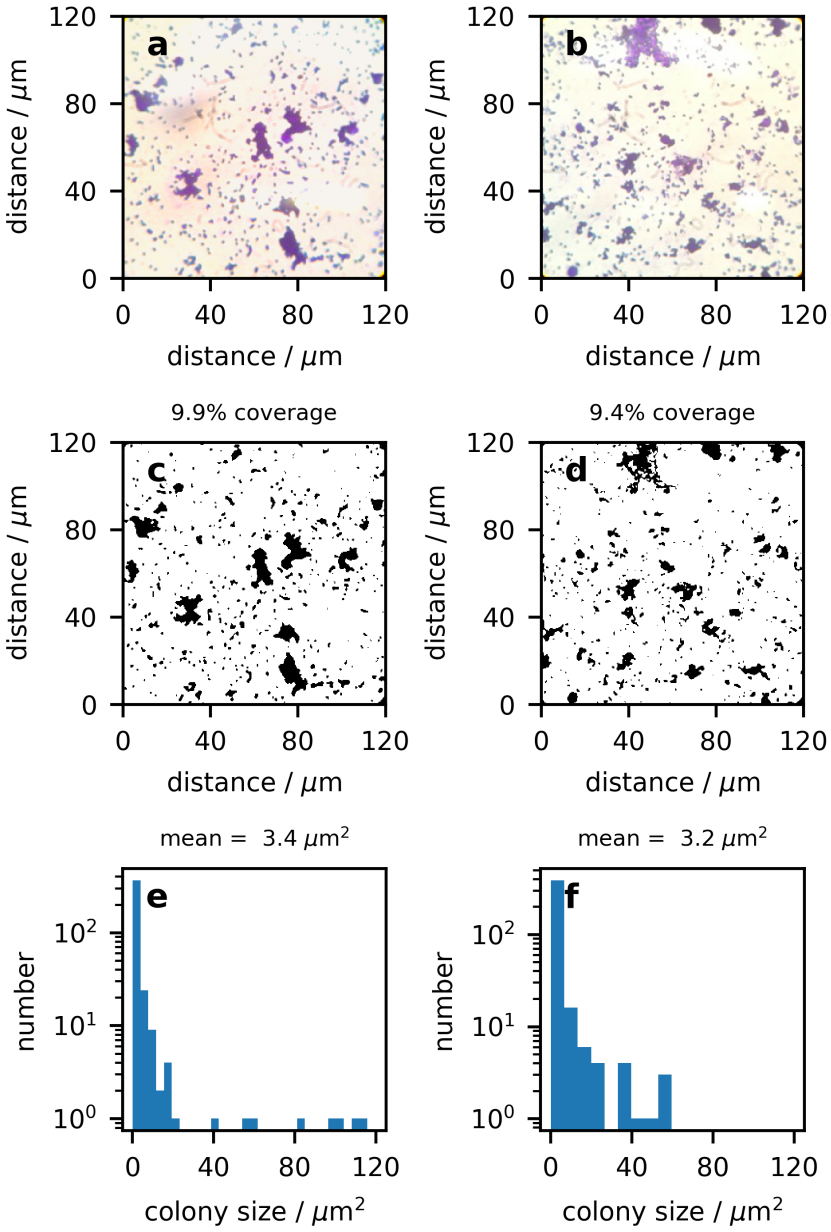

Figure 4.5: (a, b) Representative images of silica surfaces following exposure to *E. Coli* K12 for 24 h at 37 °C following rinsing and staining with crystal violet. After thresholding, a binary map was created for the purpose of (c, d) area calculation and (e, f) colony counting. Reprinted with permission from Ref. 173. Copyright 2018 American Institute of Physics.

(profilometry, atomic force microscopy), adsorbed layer thickness (ellipsometry, QCM-D, surface plasmon resonance, dual waveguide interferometry), and composition (secondary ion mass spectrometry, energy-dispersion X-ray spectrosopy), it is important for us to know that we are reporting on the same spot that the visible and infrared lasers are spatially overlapped at during the SFG measurement. Our QCM-D measurements indicate that, when exposed to fresh LB, the adsorbed mass reaches 85 ng/cm^2. Note that this value is determined post-rinsing, and that the dynamic mass is likely even greater. We are therefore interested in an in situ probe that can be performed simultaneously with the SFG measurements. Using the offline fractions with cells removed, we rinse the sample holder with water three times after each fraction is measured, then replace the water with 0.08 M NaCl solution (to match the ionic strength of the growth medium), and monitor the SFG signal at 3200 cm^{-1}. This is plotted with respect to the initial (clean silica surface) water signal in Fig. 4.1b (blue). We observe very little change throughout the growth period. This confirms that the increase in intensity observed during cell growth is not a result of molecules from the bulk being continually deposited on the surface, since the constant composition of the NaCl solution allows us to discriminate between surface and bulk effects. The slight negative slope of the NaCl rinse data indicates that the surface waters are becoming progressively less ordered.

4.3 Discussion

4.3.1 The Effect of Bulk Solution Conditions on Interfacial Water Structure

The influence of the nature of surfaces and interfacial environments on water structure is a complex phenomenon, especially in biologically active systems. How bacteria and other microorganisms affect and interact with the surface is poorly understood. Here we report on changes in interfacial water structure in the presence of growing *E. coli* at a silica–aqueous interface. From previous studies of this surface, it is known that the

water signal increases with increasing pH, as the surface becomes more negatively charged, and decreasing ionic strength, which reduces screening and expands the electrical double layer.[21,28,142,144,148,169] These same trends were observed in our SFG data (Fig. 4.1), but subsequent exploration of the bulk environment did not explain the extent of the signal increase.

Acidification and then alkalinisation of the bulk solution was not sufficient in magnitude to explain the increase in water O–H stretching signal observed. Darlington et al. recently reported SFG intensity as a function of pH at the silica–aqueous interface with 100 mM NaCl.[21] They observe the SFG water signal at 3200 cm^{-1} to increase approximately 1.5 times from pH 6 to 8, whereas in the online growth experiment presented here, the signal intensity increases more than 2.5 times the initial value (Fig. 4.1b). Thus, changes in the bulk pH alone cannot fully account for the increase in SFG intensity observed during *E. Coli* growth.

Ionic strength effects on the silica–water interface are typically observed over many orders of magnitude. In our online growth experiments, the signal increases by 250% from lag to stationary phase. When varying only the NaCl concentration, such an increase accompanies a thousand-fold reduction in ionic strength.[148] The data in Fig. 4.1d shows that the ionic strength changes by only 10%, as expected due to the high baseline ionic strength of the selected LB growth medium. We note that it has been established that the SFG signal does not change much with ionic strength in this region, making a 5 g/L NaCl growth medium ideal for this study.[148] Thus, changes in bulk ionic strength can only account for a small fraction of the increase in SFG intensity observed.

As we are working so close to the critical angle of the visible and SFG beams, we must concern ourselves with so-called optical (refractive index) effects as a possible cause for the variation in SFG signal. These effects manifest themselves in the L factors appearing in Eq. 4.2. As the product of the three local field corrections (for the SFG, visible, and infrared beams) is common to the second- and third-order terms in Eq. 4.2, we note that the intensity

is proportional to $|L_y L_y L_z|^2$. Frequency and concentration dependent refractive index data for NaCl solutions in the visible and mid-infrared[171,198,199] show that the real part of the refractive index increases with increasing salt concentration (Fig. 4.6a), and the imaginary part of the refractive index decreases with increasing salt concentration (Fig. 4.6b). This has the combined effect of substantially reducing the SFG signal through the local field factors, particularly at low ionic strength as shown in Fig. 4.6c. Note that this is the opposite trend from what is observed here. If we now consider biomolecules in solution, this would increase the bulk refractive index by approximately 0.19 for each g/mL in the bulk solution.[200] At the surface, the refractive index due to adsorbed molecules depends on their coverage and degree of hydration,[201] but is also higher than that of the non-adsorbed surface. We conclude that none of our observations can be explained by optical effects.

4.3.2 The Surface Microenvironment during Cell Growth

Since the increase in SFG signal so closely matches the growth curve, the biological component of our system must be considered. It is well known that during aerobic growth, *E. Coli* consume sugars and amino acids to produce a variety of metabolites. In LB broth, the sugar content is low, and instead consists predominantly of amino acids and small peptides.[202] During growth, preference is given to catabolizing sugars, which results in the production of carbonic acid during respiration.[203] This, in combination with exposure to atmospheric carbon dioxide, causes acidification of the surrounding environment, and is observed as the initial decrease in pH during lag phase (Fig. 4.1c). If sugars or other carbohydrates are not present in sufficient quantity, metabolism switches to the use of amino acids, followed by peptides, both of which result in the production of ammonium and increase the pH of the environment. This, too, can be seen over the course of exponential to early stationary phases in our results.

As bacteria interact with surfaces, they express a distinct sessile phenotype and begin to form colonies at the surface, eventually producing a complex network of extracellular

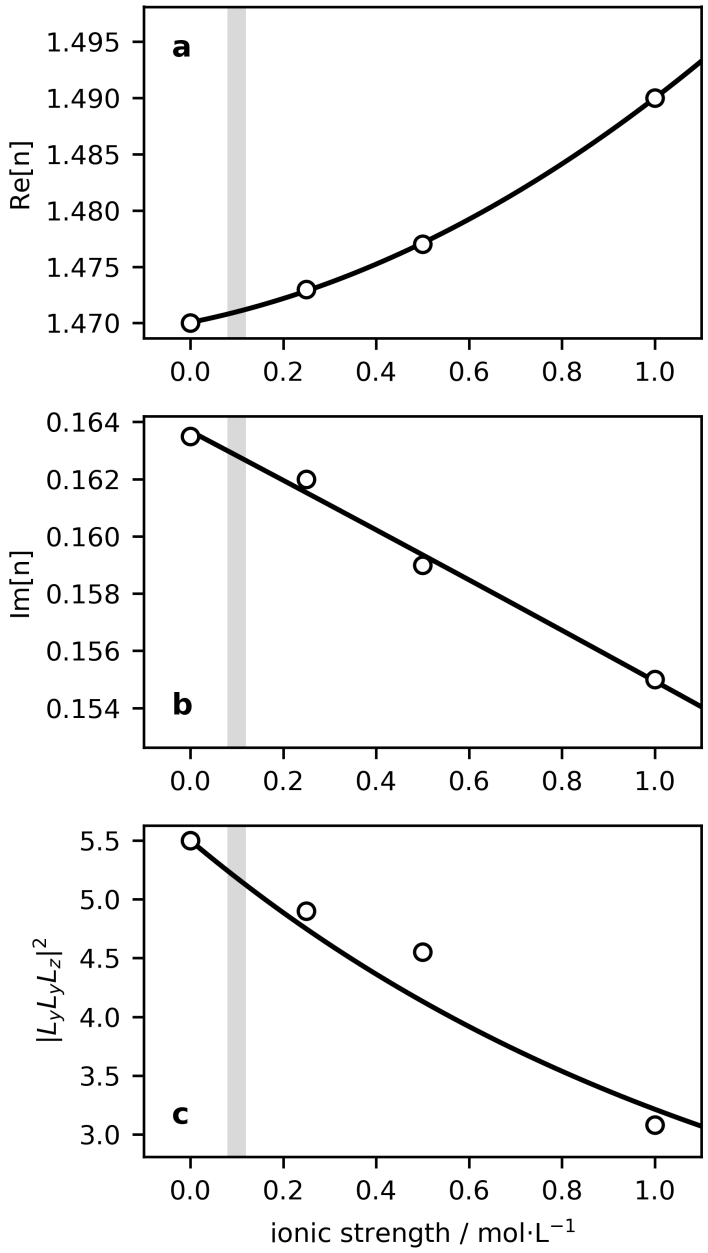

Figure 4.6: Literature values of the (a) real and (b) imaginary components of the refractive index of salt water at 3200 cm^{-1} as a function of ionic strength. (c) The effect of these optical constants on the local field correction factors. The shaded region highlights the behavior for ionic strengths in the vicinity of 100 mM. Reprinted with permission from Ref. 173. Copyright 2018 American Institute of Physics.

polymeric substances (EPS) that are characteristic of biofilms.[90] A key factor in this process is the presence of a conditioning film, which forms on the surface from deposition of proteins or cell debris from the surrounding environment, and whose purpose is to regulate cellular adherence.[204] As cells adhere to the surface and continue to divide, they enclose themselves in an EPS matrix.[205,206] At this stage, the cells produce a diverse range of proteins and biopolymers, including negatively charged exopolysaccharides, which accumulate cations and hydration waters. This EPS framework aids in keeping nutrients readily available for replicating cells and imposes sharp chemical gradients on the surroundings.[76,207] EPS contain polar and apolar regions, as well as groups with hydrogen bonding potential, which allow them to sequester ions from the aqueous environment.[76] During early cell adhesion and colony formation, bacteria can enhance chemical gradients by depleting nutrients from the local environment, and produce a variety of charged metabolic byproducts that accumulate in their place.[202] In addition, bacteria require various ionic species, especially K^+, Ca^{2+} and Mg^{2+}, for proton transport and to neutralize or bridge polyanionic lipopolysaccharides on their outer membrane.[208,209] As a consequence of these processes, there can be significant changes in the immediate extracellular conditions, including pH, ionic strength, and osmolarity. It is also known that there is no contribution to the SFG signal that arises directly from the adherence of cells to the surface.[100,101,125,126,210] One possibility is that EPS bind directly to the silica surface, without any intervening water layer. We suspect that we are not probing water surrounding EPS, due to the need for solvating the high concentration of ions and other osmolytes in the matrix, leading to a disruption rather than enhancement of the polar alignment of water molecules. Therefore, we propose that when the bacteria are introduced into the SFG setup, cells accumulate near and adhere to the silica surface, creating a microenvironment in the process, wherein water molecules and other hydrated ionic species attracted to the surface become trapped between the surface and the EPS matrix, resulting in a local pH and ionic strength that differs significantly from the bulk solution. A schematic illustrating

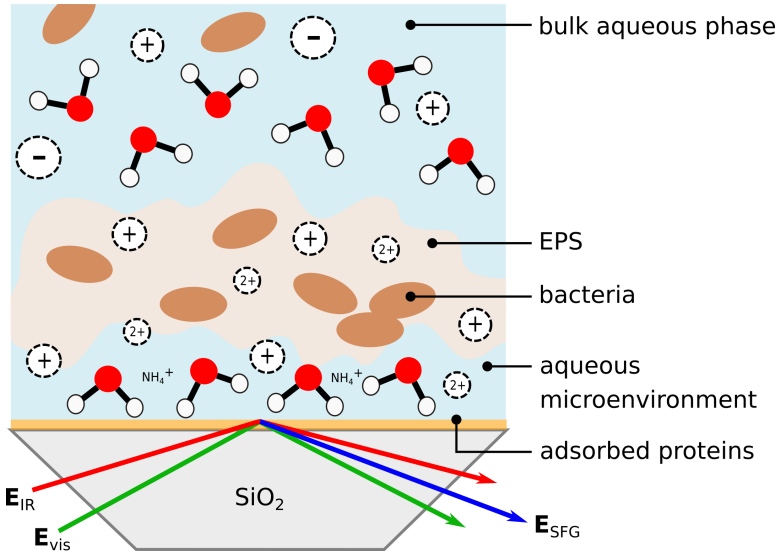

Figure 4.7: Illustration of the surface microenvironment created during bacterial growth and adhesion.

this microenvironment is shown in Fig. 4.7.

4.3.3 Effects of the Interfacial Microenvironment on Surface Conditions

At near-neutral pH, where these experiments were performed, the effect of salt on silica surface charge and dissolution rate is enhanced.[18] This is due to the low buffering capacity of the surface groups, which leads to a large sensitivity of water molecules at the interface to the introduction of cations. Such heightened sensitivity could account for the increase in SFG signal intensity observed in the presence of growing *E. Coli* in this interfacial microenvironment. If ions were removed from the surface through attraction to EPS, the ionic strength in the Stern layer would be reduced. This would cause an increase in ordering of water molecules in the EDL and/or a reorientation of those waters, resulting in an increase in the SFG intensity. Moreover, waters in the hydration shell of alkali cations attracted to the negatively charged silica can dissociate, leading to an accumulation of hydroxide anions at the surface and thus an increase in the local pH. Results from Darlington et al.[21] indicate that the pH of the microenvironment would have to increase to a pH between 10 and 11 in order to account for the 250% increase in SFG intensity. This

was not observed in the bulk solution, which ranged from pH 6.5 to 8.4 (Fig. 4.1c). Such an increase is plausible, however, given that increasing concentrations of metabolic waste products like ammonium would migrate to the negatively charged silica, enhancing local pH increases. This would result in greater alignment of (more) interfacial water molecules (through the $\chi^{(3)}$ term) that in turn causes the SFG signal to increase. Any remaining trapped cations would also have this effect, increasing local pH through dissolution of their solvation waters, although this would be a small contribution. The combination of these processes could result in the required combination of pH increase and ionic strength decrease, since the diffusion rate of the bulk solution into the EPS matrix is low.[211]

The increase in spectral intensity closely follows the growth curve and is consistent with the proposed changes in the interfacial pH and ionic strength of the microenvironment. The concentration of ammonium is closely linked to bacterial growth rate and physiology,[202] as is the formation of EPS.[90] During the lag and early exponential growth phases, *E. Coli* have a predominately negative surface charge and so experience electrostatic repulsion with each other and negatively charged regions of silica.[212] As a result, fewer cells adhere to the surface and very few colonies form. During this time, little EPS is produced. As growth progresses, polysaccharide concentrations on the outer membrane increase, displacing the previously uniform charge distribution.[137] This results in less electrostatic repulsion and greater adhesion and cohesion. As the bacteria divide, it becomes an exponential pattern as more cells are available for interaction with other cells and the surface. A consequence of this increase in metabolism is the compositional changes in the immediate environment, resulting in reorientation of proteins near the surface. Such reorientation has been shown to result in greater orientation of interfacial water molecules.[213] As the cells reach stationary phase, they are secreting metabolites at a fraction of the rate they were during exponential growth, since there are fewer cells dividing at this stage.[137] This is reflected in the SFG spectra, which also plateau as a result of the relatively constant solution composition, pH, and ionic strength in the microenvironment, as well as in the bulk growth medium.

All of the changes in pH and ionic strength that occur in the microenvironment happen as a result of cell growth. This explains why they are only observed in the online growth experiments. Despite the same metabolic processes occurring in each fraction taken from offline and online conditions and given that both experiments were sampled at the same time points, the increase in SFG water signal was only observed if cells were given prolonged access to the surface, as in the online experiments. This allows for bacteria to adhere and EPS to accumulate. In light of this, when fractions containing cells interact with the surface only during the brief period of measurement (10 min), the cells and their EPS do not have sufficient time to establish an increase in pH and decrease in ionic strength in the microenvironment, as would be observed with cells exponentially growing in situ. Thus, only the small increase in bulk pH exists for these later fractions, which, as stated previously, is not enough to account for the increase in SFG intensity.

A small amount of signal increase did occur when growth media devoid of cells was monitored spectroscopically in the sample holder over time, but only those fractions from a mature culture. As seen in Fig. 4.3, when media interacted with the silica surface over time, fractions from late exponential phase (collected at 14 h) displayed a 60% increase, and from stationary phase (collected at 25 h) a 45% increase. Yet, a repeat experiment with a different 14 h fraction showed no increase in the signal intensity. The most likely explanation for these conflicting results is that for the 14 and 25 h fractions in Fig. 4.3, the increase in signal was due to some viable cells remaining in the fraction after filtration. Only one viable cell would have to be present in order to propagate a new culture, which would then show the same characteristic increase in SFG intensity with growth. This would be more likely to occur in these later fractions since the cell density is much higher, giving rise to a greater probability of some cells remaining behind even after centrifugation and filtration. For the 14 h fraction in Fig. 4.4, presumably all cells were removed before being monitored spectroscopically, and so no signal increase was observed. This would mean that the SFG trend is not simply due to accumulation of extracellular components at the

surface. Instead, cells must be present and in steady-state growth to actively produce EPS, as well as metabolic byproducts like ammonium, in order to increase the pH and decrease the ionic strength at the interface.

4.4 Conclusions

We have observed that water is a sensitive reporter of interfacial conditions during bacterial growth. Although the silica–water surface structure in the presence of the initial growth medium is substantially altered from that of the neat surface as a result of the osmolytes and high ionic strength, this structure does not change as a function of time. However, when cells adhere onto the surface and their metabolic byproducts enter the solution, those molecules enhance the interfacial water signal, attributed to a reduction in the local ionic strength as extracellular polymeric substances deplete ions from the interface. When cells are present, the increasing pH of the immediate environment due to respiration causes a further increase in the surface water response. Further work is needed to confirm these processes as the primary cause of the SFG response, which may also be affected by ordered water in the outer membrane of cells near the surface, changes in surface charge density upon cell adhesion, and by differences in the pH and ionic strength in the unstirred layer surrounding the bacterial outer membrane.

Chapter 5

Investigating the Silica–Water Interfacial Microenvironment during Bacterial Growth and Adhesion

5.1 Introduction

SFG data in the previous chapter revealed a monotonic increase in the signal intensity with *E. coli* growth that closely matched that of the population growth curve. It was also discovered, based on monitoring fractions of growth medium both with and without cells, that *E. coli* must be present and growing over an extended period of time in order to see the observed increase in the SFG intensity. As a result, it was posited that this trend in the SFG response is due to the formation of a microenvironment in the vicinity of the silica surface, which has a distinct ionic strength and pH compared with the bulk solution. These differences arise from the production of EPS upon cellular interaction with the surface and from metabolic byproducts during cell division, including ammonium. The charged moieties on EPS—particularly the numerous negatively charged regions on these molecules—require counterions for neutralization; thus, they act as a sort of ion sponge that scavenges nearby ionic species, including those in the Stern layer near the surface.

Although the above hypothesis is reasonable based on what is known about sessile bacteria at surfaces, there are three additional possibilities that could account for the observed trend in the SFG response: (1) bacteria possess ordered water in their outer

membrane that could contribute via $\chi^{(2)}$ to the SFG intensity upon adhesion; (2) cell adhesion and EPS production on the surface could alter the surface charge of silica, thereby changing the $\chi^{(3)}$ contribution to the SFG signal; and (3) the distinct ionic strength and pH of the unstirred layer surrounding the cells themselves could be contributing to differences in the solution conditions of the microenvironment near the surface.

The goal of this chapter is to narrow down the above possibilities and explain why the SFG signal intensity increases at all. In order to provide a more complete picture of the surface microenvironment during cell growth and adhesion, we use SFG spectroscopy, EPS removal and staining techniques, zeta potential measurements, and white light and fluorescence microscopy.

5.2 Results

5.2.1 Sum Frequency Response during Normal and CER-treated *E. coli* Growth

To determine whether the presence of bound and free EPS during initial exposure of the cells to silica influenced the SFG response, we removed bound EPS via treatment with a cation exchange resin, as well as free EPS in the process of centrifugation of the treated cells. Fig. 5.1a shows the increase in SFG signal (normalized to water) over a 26 h growth period of CER-treated bacteria. It is apparent that both the evolution and extent of increase in the signal intensity are similar to that of untreated cells. Comparing this increase in SFG intensity to the growth curve in Fig. 5.1b, the bulk population of cells is observed to increase much more rapidly and levels off into stationary phase after approximately 7 h of growth. In contrast, the SFG signal continues to increase steadily at a slower rate until about 20 h, where it begins to plateau. This asynchronous behaviour diverges from that seen in the previous chapter, where the growth curve matched the evolution of the SFG signal almost exactly. However, previous growth curves were measured under different conditions than the SFG experiment (i.e. in a shaker–incubator) whereas the growth curve

shown in Fig. 5.1b was measured from cells grown in the same Teflon sample chamber, with the same temperature control and stirring apparatus as the SFG measurements. Thus, it is a more accurate reflection of how the bulk population of cells evolves under these conditions.

It is worth noting that the normalized spectral intensities presented in Fig. 5.1a are lower than those reported in the previous chapter, which increased from 21 to 50% of the water signal. Since we were working above the critical angle (66°) for silica–water, the local field corrections caused a further increase in the signal, purely as a result of optical effects. We initially chose to work at a visible beam angle of 68° (above the critical angle) so as to take advantage of the boost in SFG signal when under total internal reflection conditions. However, since the extent to which the water SFG intensity increases is central to our study, we now work at an angle (64.8°) below the critical angle for this system, which results in a slight decrease in the signal intensity purely from optical effects. Thus, when the signal increases in our SFG experiments, it is undoubtedly a result of changes in the local water environment and not simply due to refractive index changes.

5.2.2 Imaging Silica Surfaces After Exposure to Normal and CER-treated *E. coli*

To determine if the CER treatment impacted the number of bacteria adhered to silica, we imaged surfaces after exposure to both normal and CER-treated *E. coli* at each stage of the growth cycle (lag, exponential, and stationary). At the same time, to elucidate if there were differences in surface coverage by EPS, a non-specific stain for polysaccharides (congo red) was used. Table 5.1 summarizes the white light and fluorescence imaging results after silica surfaces were exposed to lag, exponential, and stationary phase cells after either no treatment, or CER treatment. In both cases, the number of cells on the surface increased from lag to exponential phase, and then decreased by stationary phase. For untreated bacteria, similar to the cell count, EPS coverage also reached a maximum in exponential phase and then decreased by the stationary phase. This is unsurprising as the majority of

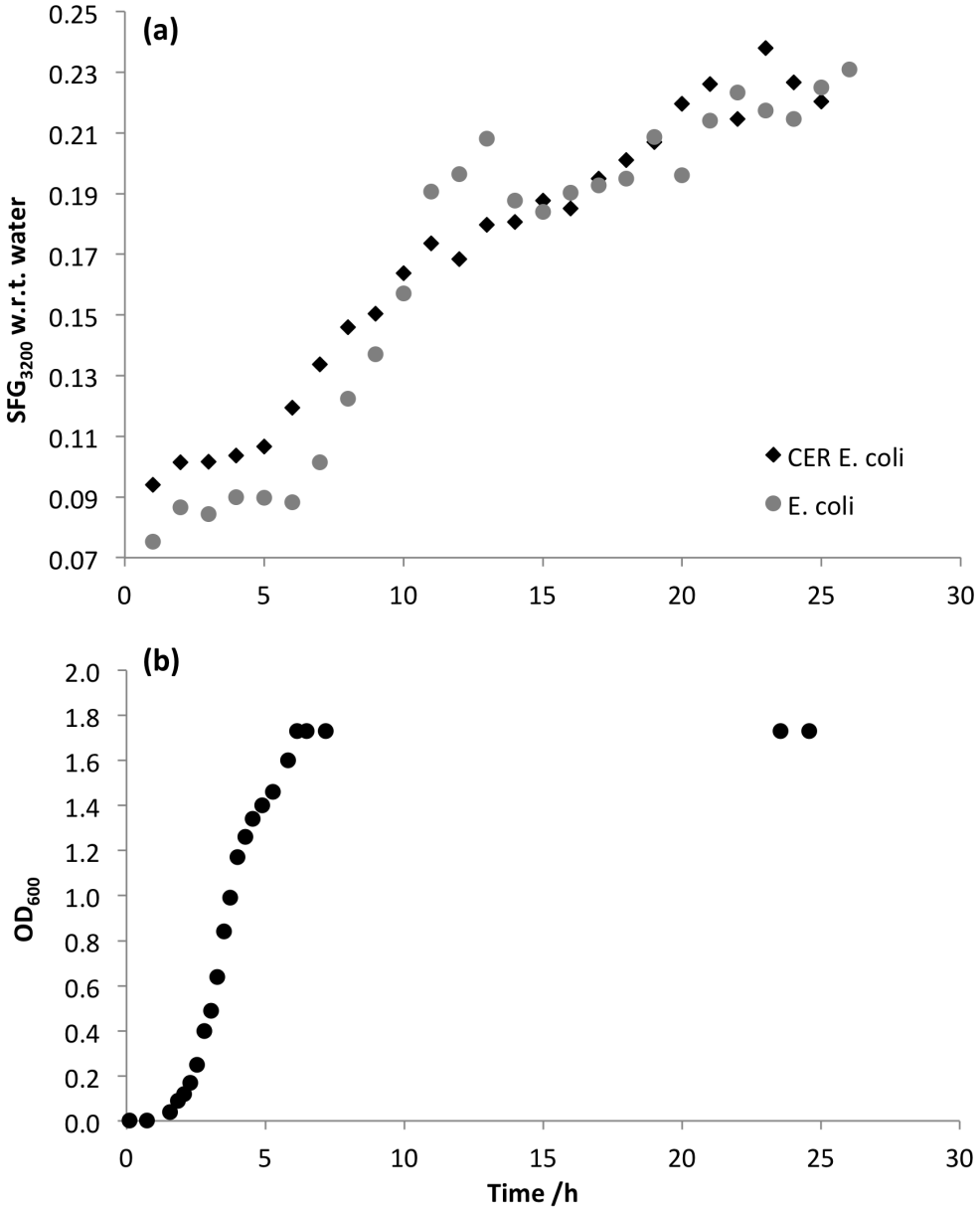

Figure 5.1: (a) Average SFG intensity at 3200 cm^{-1} with time for normal (grey circles) and CER-treated (black diamonds) *E. coli*. Each trace is an average of 3 separate experiments. (b) Population growth curve as measured by the optical density at 600 nm in the SFG Teflon sample holder.

EPS remaining on the surface after rinsing would be associated with adhered cells. Under hydrated conditions during the experiments, there would presumably be more loosely-bound EPS surrounding cells and free EPS within the microenvironment. For untreated *E. coli*, the percentage of EPS per cell remained fairly constant throughout each stage of growth. For CER-treated *E. coli*, there were approximately one half the number of cells on the surface during lag, exponential, and stationary phases, although the overall pattern of increasing and then decreasing cell count was consistent. Removal of bound and free EPS with the CER technique resulted in lower EPS coverage throughout the growth cycle; however, the coverage continually increased. It also initially reduced the percentage of EPS per cell, which indicates that the treatment successfully removed negatively charged EPS from the outer membrane; however, the cells were able to fully restore their bound EPS by stationary phase.

Cell Treatment	Growth Phase	OD_{600}	Cell Count	EPS Coverage /%	% EPS/Cell
none	lag	0.03	301	1.9	0.006
	exponential	0.21	1201	5.6	0.005
	stationary	2.00	964	3.4	0.004
CER	lag	0.03	151	0.3	0.002
	exponential	0.25	445	0.9	0.002
	stationary	2.00	398	1.8	0.005

Table 5.1: Cell counts and EPS coverage for untreated and CER-treated *E. coli* on silica, obtained using white light and fluorescence microscopy, respectively.

5.2.3 Spatial Correlation of the Interfacial Water Response with Cell Counts and EPS Coverage

One possible explanation as to why the SFG signal increases with cell growth is that the surface charge is altered upon adhesion of negatively charged *E. coli*. An increase in the negative surface charge of silica would result in a larger surface field (E_0) and thus a greater contribution from $\chi^{(3)}$ to the SFG signal, causing an increase in signal intensity. In order to probe whether changes in the surface charge would affect the SFG response, we translated the prism vertically over 3.25 mm to see if the intensity at 3200 cm^{-1} was

affected. Considering the size of the bacteria (approximately 0.8 $\times$ 4 μm), translating the prism on a millimeter length scale should capture some variation in surface conditions. Fig. 5.2a shows the normalized SFG intensity at 3200 cm^{-1} at different positions on the prism surface, while still maintaining overlap of the incoming visible and IR beams. It is evident that the signal does not change with location on the prism. When we look at the cell counts from this same region on the prism, we see that the number of cells ranges from about 580–1100, even reaching 1600 cells in one location (Fig. 5.3a; field of view = 287 $\times$ 390 μm). The cell count decreases on either side of the region of interest (between 0 and 3.25 mm) as these are nearer to the edge of the prism and likely outside the O-ring during growth. The corresponding coverage by EPS (as visualized by fluorescence from congo red stain) ranges from approximately 0.8 to 2 % (Fig. 5.3b).

Fig. 5.2b illustrates the SFG intensity at 3200 cm^{-1} for each position on the prism at the various times they were measured throughout the 27 h experiment. The water signal at each position was measured first, against a clean silica prism. This was followed by LB, *E. coli* after 5 h, and then 24 h of growth. At this time, the cells were removed and the water and then LB intensity were measured sequentially. It is interesting to note that the water signal did not reach the same intensity as it was initially, while the LB did not decrease to the intensity it was on the clean prism; in fact, it appears slightly higher in intensity than the *E. coli* after 5 h of growth, but less than after 24 h. When the cells were placed back into the sample holder and the SFG intensity immediately measured (grey square), the signal was almost as high as for the cells at 24 h. Fig. 5.2b also highlights how similar the SFG signal is at each position, with almost all samples appearing as one data point, due to the overlap.

Four representative images spanning the region of interest on the prism are shown in Fig. 5.4a–d. From these images it is apparent that the majority of *E. coli* adhere as individual cells in a fairly uniform manner, with a few small clusters of cells in some regions (lower right corner in Fig. 5.4b). Although the cell count may fluctuate in each image, the

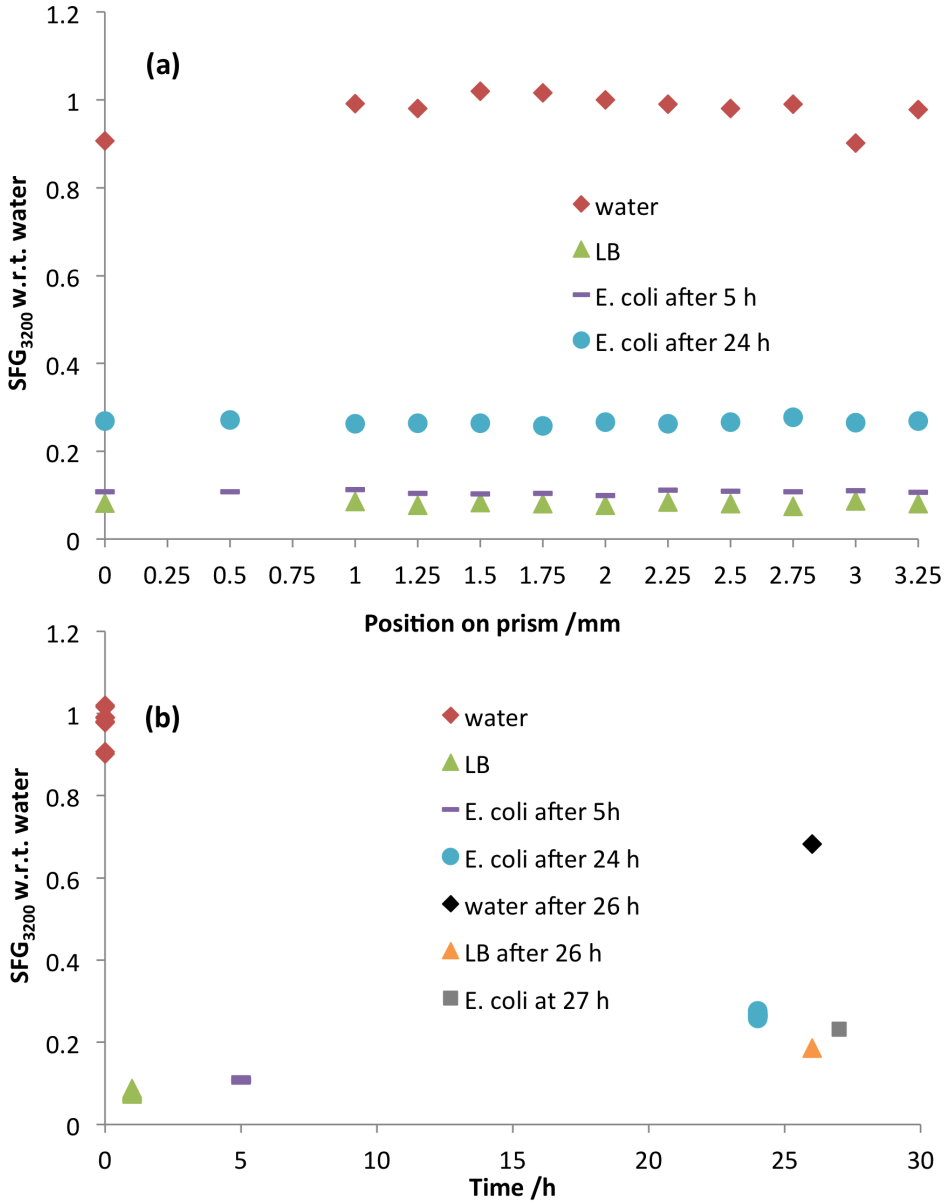

Figure 5.2: (a) Normalized SFG intensity at 3200 cm^{-1} with position on the prism. (b) Normalized SFG intensity at 3200 cm^{-1} at each position with time. The SFG response of water and LB after 26 h were measured directly after removal of cells.

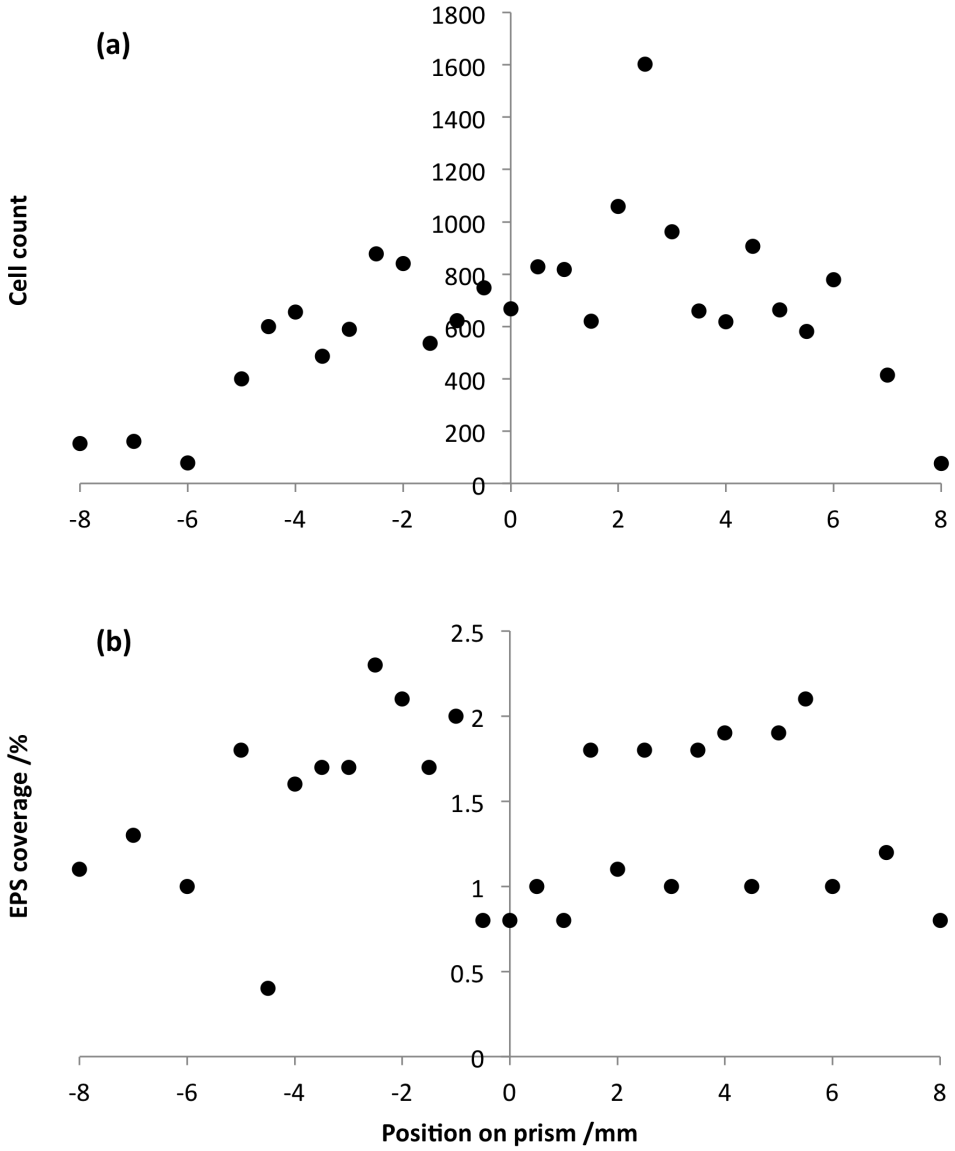

Figure 5.3: (a) Cell count at various positions on the prism. (b) Corresponding EPS coverage at those same positions.

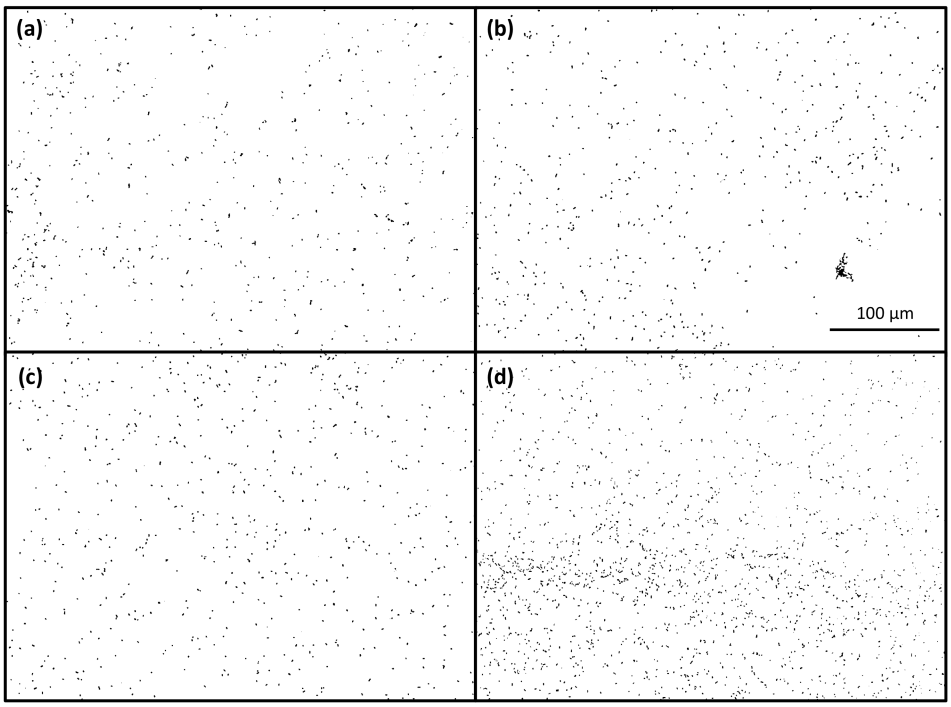

Figure 5.4: (a)–(d) Representative white light images of adhered *E. coli* spanning the translation region of interest on the prism surface.

beam spot (0.5 mm) would capture a relatively uniform distribution of individual cells and a few small clusters.

5.2.4 Zeta Potential Measurements on Silica Beads

As shown in Table 5.2, pure silica beads, as well as those exposed to normal and CER-treated *E. coli*, all had negative zeta potentials. All measurements were performed in filtered 0.02 M NaCl at pH 6.8. Pure silica spheres had the largest negative zeta potential, followed by silica with normal *E. coli* adhered, and then silica with CER-treated *E. coli*, which possessed the least negative zeta potential. The ELS experiment for CER-treated cells on silica was performed on two separate samples from the same liquid culture in order to ensure that measurements were not affected by sampling. The two experiments yielded similar results (4.8% difference) therefore the value reported in Table 5.2 is an average of the two measurements. The standard error for each experiment (less than 3%) was determined by 10 replicate measurements. In addition, the residuals were all considerably

less than 0.1, indicating an excellent fit of the phase data.

Sample	Mobility / $m^2s^{-1}V^{-1}$	Zeta Potential / mV	Residual / rad
silica	-4.1 ± 0.1	-52 ± 1	0.02
E. coli on silica	-3.1 ± 0.1	-40 ± 1	0.01
CER *E. coli* on silica	-2.2 ± 0.1	-29 ± 1	0.02

Table 5.2: Electrophoretic mobility and zeta potential of silica beads exposed to untreated and CER-treated *E. coli*.

5.3 Discussion

5.3.1 Ordered Water on the Bacterial Outer Membrane and Cell Adhesion

One possibility as to why the SFG signal increases is the presence of ordered water in the nanointerface surrounding the bacterial outer membrane. This highly structured water would increase the $\chi^{(2)}$ contribution to the SFG intensity; thus, as more cells bringing ordered water adhere to the surface, an increase in SFG would be observed. This is consistent with the imaging results presented in Table 5.1 up until exponential phase, where an increasing cell count coincides with an increasing SFG intensity. However, when the number of cells decreases in the stationary phase, the SFG does not also decrease, but instead continues to increase before reaching a plateau (Fig. 5.1). Thus, it is unlikely that cells bringing ordered water in their outer membrane to the surface is solely responsible for the increase in SFG intensity. If this were the case then the SFG signal would decrease concurrently with cell detachment. However, this possibility cannot be ruled out entirely. It is known that the hydrophilicity of the cell surface increases with starvation time.[16] Since no new nutrients are supplied to the bacteria during growth, the charge distribution and therefore extent of solvation on the starved bacteria may change significantly from lag to stationary phase. It is likely that more water becomes associated with the bacterial outer membrane as growth (and then starvation) progresses. Consequently, although membrane-associated water cannot be the only reason for increasing water signal in SFG experiments,

it may contribute in part to the observed trend.

Table 5.1 shows that, after CER treatment, there are approximately half the number of adhered cells at all stages of growth. However, Fig. 5.1a shows that the increase in SFG intensity is the same for both normal and treated cells. These results provide further evidence that the SFG response cannot be exclusively due to ordered water on the bacterial membrane. Table 5.1 also demonstrates that the number of cells on the surface is greater in early exponential phase compared to late stationary phase, when cells have detached. Detachment may occur in starved *E. coli* as a result of increased charge heterogeneity on the outer membrane, due to the expression of a unique set of proteins and LPS molecules during stationary phase.[137] Moreover, the hydrophobicity of the cell surface decreases with starvation time, which may also affect their adhesiveness.[16] This adhesion pattern, where maximum surface coverage occurs during the exponential phase and then decreases in stationary phase, has been observed in another study by our group.[214] In that work, although the surface coverage was dominated by large clusters of cells (greater than 100 μm^2), the number of small clusters and individual cells on the surface far exceeded the number of large clusters. In fact, clusters less than 3 μm^2 increased steadily over the growth cycle, in a manner similar to the increase in SFG intensity over the same time period. This suggests—assuming ordered water surrounding adhered cells contributes at least in part to the increase in SFG signal—that individual cells (and small clusters) play a more significant role in altering the interfacial water structure and/or solution conditions in the microenvironment at the surface, than do large clusters.

5.3.2 Surface Charge and Cell Adhesion

Another possible explanation for the increase in SFG intensity is an increase in the negative surface charge on silica upon bacterial adhesion and production of negatively charged EPS. Since we are concerned only with trends in surface charge, we use the zeta potential as an approximation, due to its relative ease of measurement. However, since the zeta

potential of planar silica is difficult to measure accurately, we instead measure the zeta potential of silica beads with normal and CER-treated cells adhered in order to determine if trends in zeta potential could explain the evolution of the SFG signal. The zeta potential measured for pure silica (-52 mV) agrees well with values reported in the literature at a similar ionic strength.[215,216] When *E. coli* adhered to the silica particles, the zeta potential became more positive. Although *E. coli* are also negatively charged, their zeta potential (-38 mV) is more positive than that of pure silica.[217] As shown in Fig. 5.5, when bacteria adhere to the beads, the shear plane is shifted farther from the surface of the particle. In addition, adhered bacteria displace some of the counterions in the Stern layer, pushing them further from the surface toward the slip plane. Moreover, the protruding cells with many negatively charged membrane proteins, bound EPS, and other surface groups attract positively charged ions, further increasing the counterion concentration near the slip plane, which is now located further from the surface. All of the above factors may contribute to a more positive zeta potential of the silica beads when bacteria are adhered. When *E. coli* undergo CER treatment, many of the negatively charged EPS are removed from the cell surface (although negatively charged membrane-bound proteins remain). This results in the creation of a greater number of positively charged regions on the bacterial surface. Since the measurement conditions for the silica beads (0.02 M NaCl) differ from those of planar silica (0.08 M NaCl in LB, which contains other solutes and osmolytes), it is difficult to conclude whether there would be less adhesion of CER-treated bacteria to the beads as was the case for planar silica. Nevertheless, positively charged regions on CER-treated *E. coli* themselves could coincide with the slip plane, thereby contributing to the even more positive zeta potential as a result of decreased mobility. This phenomenon likely contributes in addition to the aforementioned slip plane distance and counterion effects upon adhesion of bacteria to the particles.

The important finding from the data presented in Table 5.2 is that the zeta potential—and thus the surface potential—of silica becomes more positive with bacterial adhesion.

However, a more positive potential does not account for the increase in SFG signal observed when both untreated and CER-treated cells are grown in proximity to a silica surface. It must be noted that the zeta potential is not the same as the surface potential, which ultimately controls the strength of the surface originating electric field responsible for the $\chi^{(3)}$ contribution to SFG intensity. Others have shown that for silica nanoparticles in 10 mM NaCl at pH 10, the surface potential is far more negative—by an order of magnitude—than the zeta potential.[215] Nevertheless, it is generally accepted that regardless of whether the zeta potential and surface potential are similar in magnitude, if the zeta potential increases then the surface potential likely increases as well. Thus, adhesion of *E. coli* would likely result in a more positive surface potential for silica (even more so when CER-treated bacteria adhere). A more positive potential would result in a reduced ability of the surface field to align water molecules in the diffuse layer, which rules out this possibility for explaining the increase in SFG signal.

Although adhered bacteria themselves are not responsible for the observed SFG trend, they do express a unique set of exopolymers—many of which are negatively charged—that could contribute to changes in the local surface charge density with time. Results from the SFG translation experiment showed that, even after 24 h of growth, when the prism was translated over a 3.25 mm region, no change in the SFG signal occurred. From the cell count over this same region (in stationary phase), we know that the number of cells adhered in any given image varied by up to 600. The dimensions of these image tiles (287 $\times$ 390 μm) are slightly smaller than the IR beam diameter (500 μm), which limits the size of the area probed by SFG. Since a greater number of cells (and thus EPS) likely results in a higher surface charge density, more cells may produce a higher SFG intensity in that region. However, even in regions with more cells and greater EPS coverage (Fig. 5.3), no corresponding increase in signal was observed. Moreover, increases in surface charge density would be dependent on cell deposition over time; yet, the SFG signal does not decrease in the stationary phase when it is known that there are fewer cells on the surface

(Table 5.1). In fact, it continues to increase well into the stationary phase, until around 20 h. Even when the prism was translated after 5 h (in the exponential phase, when there are more cells on the surface), no change in the SFG intensity was observed. It may be that, considering the size of the IR beam, slight variations in surface charge density are averaged out over the entire area being illuminated. Nevertheless, neither an increase in the negative surface charge nor surface charge density of silica seems to explain the evolution of SFG intensity with cell growth.

5.3.3 Changes in the Ionic Strength of the Microenvironment

The first two possibilities—increasing numbers of adhered cells and a concurrent increase in negative surface charge—are unable to account for the trend in SFG intensity with cell growth. Thus, changes in the ionic strength and pH of the microenvironment are likely responsible. Fig. 5.1a, in combination with imaging results presented in Table 5.1, indicate that the increase in SFG intensity is independent of the number of cells on the surface as well as the presence of bound EPS during early growth and adhesion events. Although bound EPS are essential to cell aggregation and biofilm formation, these exopolymers only aid bacteria in forming specific interactions with the surface, but do not prevent them from adhering. This disadvantage is likely why there are fewer cells on the surface after CER treatment, but many were still able to adhere. Nonetheless, it seems that initially, the increase in SFG intensity tracks the concomitant increase in cell adhesion to silica until the end of exponential phase, at which point the SFG signal continues to increase and then plateaus, even when cells are detaching from the surface faster than they are attaching. This indicates that cell attachment and growth has altered the microenvironment near the surface in some way, which continues to influence the interfacial water response, even when some cells depart the surface.

In Fig. 5.2b the SFG intensity increased dramatically when cells were replaced with water after 26 h of growth, although not up to the initial water intensity on clean silica. Such

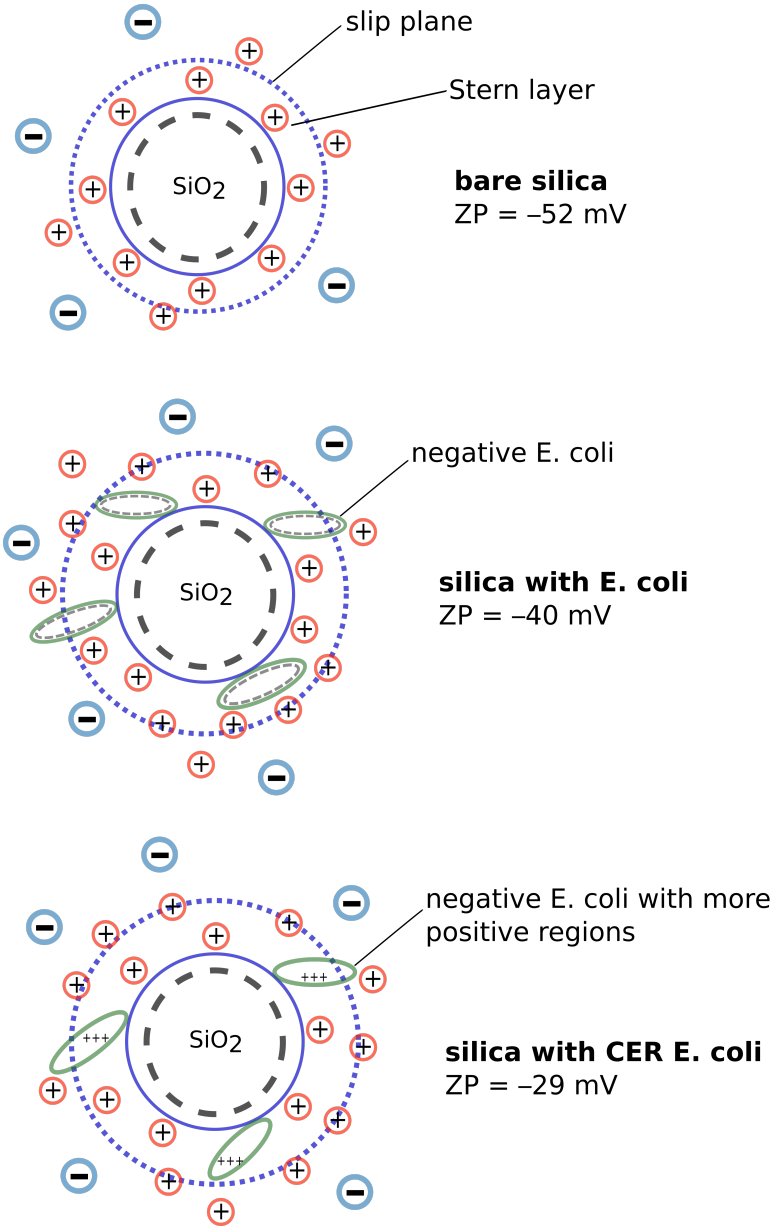

Figure 5.5: Schematic illustrating the slip plane in relation to the silica particle and adhered *E. coli*. Top: bare silica particle; middle: silica particle with normal *E. coli* adhered; bottom: silica particle with CER-treated *E. coli* adhered.

a dramatic decrease in the bulk ionic strength would cause the SFG to increase; however, the fact that it doesn't reach the original silica–water intensity suggests that an organic layer remains on the surface even after gentle rinsing with water. Between the conditioning layer, bacteria, and their sticky EPS, the surface would be quite rough and uneven, resulting in disruption of ordered water at the surface. When the water is then replaced with fresh LB,

the signal intensity decreases, but again not down to the initial intensity at the start of the experiment. Increasing the bulk ionic strength to such a degree would certainly decrease the SFG intensity; however, the intensity remains higher than the initial LB but lower than the previous *E. coli* intensity at 24 h, indicating that the water and LB rinse did not completely disrupt the microenvironment created at the surface by cell adhesion and growth. It is likely that some cells and EPS remain at the surface, resulting in a distinct ionic strength in the microenvironment compared with the bulk LB solution. When the same cells and growth medium previously removed were then placed back in the sample holder at 27 h and their SFG response measured after 10 min, the intensity was higher than that of LB, almost at the same level it was at 24 h. After one more hour of growth the SFG response of the cells again reached the same 24 h plateau intensity.

On average, the SFG signal intensity for both normal and CER-treated cells increases after 5 h of growth, until approximately 20 h. This means that the majority of increase in the signal occurs during the late exponential and early stationary phases. By this time, bacteria have adjusted to the solution conditions and significantly increased their bulk population, resulting in more cells interacting with the surface. With the presence of neighbouring cells near the surface, adhered bacteria participate in quorum sensing, which results in the production of a distinct set of exopolymers and signalling molecules in outer membrane vesicles. *E. coli* also produce more alkaline metabolites during later stages of growth, when their metabolism switches over to consuming peptides instead of carbohydrates. It may be that all of these steps are required *before* the ionic and pH gradients in the microenvironment are established, which then increase with further cell division and EPS/outer membrane vesicle production. The composition of these solutes would be distinct from those produced earlier in exponential phase, when a different set of carbon and nitrogen sources were available for the cells to metabolize. Thus, the increase in SFG intensity would be delayed with respect to the increase in population, as observed in Fig. 5.1. If the ionic strength of the microenvironment is altered as a result of more EPS

accumulating ions, the SFG response of water molecules in the microenvironment would reflect this change. We propose two possible mechanisms to account for the continual increase in the SFG response in the following sections.

5.3.4 Hypothesis 1: Decreasing Ionic Strength at the Interface

Fig. 5.6a illustrates the conditioned silica surface in the presence of LB. The multitude of ions in the growth medium decrease the interfacial water signal significantly through screening of the negative surface charge as well as specific adsorption of cations at the surface, thereby disrupting the existing hydrogen bonding network. When *E. coli* are introduced into the system, after a brief lag phase in which they acclimatize to the solution conditions, they adhere as individual cells and in small clusters (Fig. 5.6b). As a result of the roughness of the protein, polymer, and bacteria-coated surface, it is reasonable to assume that the vast majority of the SFG signal originates from diffuse layer water molecules contributing via $\chi^{(3)}$, with little contribution from ordered water at the surface ($\chi^{(2)}$). These adhered bacteria, as well as those swimming near the surface, begin to express distinct membrane proteins and bound EPS, as well as excrete free EPS, outer membrane vesicles, and other metabolites near the surface. The increasing accumulation of these charged solutes—including in regions where no bacteria are adhered, either by diffusion or swimming/crawling cells—would attract nearby ions, including those in the Stern layer. This would decrease the ionic strength of the microenvironment directly adjacent to the surface, resulting in an increase in the SFG intensity from reduced screening of the negative surface charge. At the same time, the pH of the microenvironment is likely increasing due to production of alkaline metabolites such as ammonium, which would further enhance the SFG signal. In addition, the cells are surrounded by an unstirred layer with its own distinct pH and ionic strength gradients. This layer may further contribute to differences in the solution conditions of the microenvironment, causing the SFG signal to increase. It should be noted that when cells leave the surface: (1) many leave from small clusters as

a result of nutrient depletion in more crowded regions and (2) individual cells that are no longer attached can still remain near the surface, contributing to the "ion sponge effect" via EPS and outer membrane vesicle production, as well as their unstirred layer. Point (1) is confirmed by Sun et al., who found that the size of larger bacterial clusters decreased before that of smaller clusters.[214]

In the case of CER-treated bacteria (Fig. 5.6c), although there are fewer cells on the surface during all stages of growth, the more irreversibly and reversibly adhered cells would still produce the same bound and free EPS, as well as outer membrane vesicles and charged metabolites. As shown in Table 5.1, although CER-treated cells adhere during the lag and exponential phases with fewer EPS per cell, it is fully reinstated by late stationary phase. This is because the CER treatment strips away bound EPS only from cells it comes in contact with, and does not alter the genes that encode for EPS production. Since the doubling time of *E. coli* is only approximately 20 min, a large number of daughter cells can be produced in a relatively short period of time that would possess all of the bound EPS that is encoded for in their genome. Thus, by stationary phase, the majority of cells would appear as if they had never received the CER treatment, with their bound and free EPS both intact. As a result, even with fewer cells, enough solutes and vesicles are likely in place to produce a similar ion sponge effect as seen with normal cells. Moreover, in images taken at each stage of growth after CER-treatment, very few clusters of cells were observed; instead almost all cells present were adhered individually. This is likely due to the lack of bound EPS on these cells during lag and early exponential phases, which aid in cell aggregation and cohesion. Since the majority of treated cells adhere more sparsely, they would each possess a significant unstirred layer, which would be reduced when cells are crowded and completely disappears in cell aggregates, where narrow intercellular spaces are required. Thus, the presence of a greater number of distinct unstirred layers around these cells may contribute to producing pH and ionic strength conditions in the microenvironment similar to those observed with untreated bacteria. This—in conjunction with the accumulation and

diffusion of charged EPS and vesicles over time—could explain why the SFG increases to the same extent in both cases, even though there are different amounts of adhered cells. Furthermore, the presence of an unstirred layer for more isolated bacteria may explain why Sun et al. found that adhesion of smaller clusters and individual cells more closely followed the trend in SFG intensity than larger colonies, which may have less of an impact on solute and ion gradients in the microenvironment due to the absence of an unstirred layer surrounding the cells.

5.3.5 Hypothesis 2: Ordering of Solute Hydration Shells

Biofilms are often treated as colloidal hydrogels, with cells analogous to colloids and the ECM to a cross-linked hydrogel. In fact, biofilms are mostly composed of water, with the majority of it residing in the vicinity of solute ions and macromolecules.[218] These water molecules, bound in the hydration shells of solutes, have properties that differ from free, bulk water. Studies have shown that the majority of water in biofilms is bound by amino acids and salt ions; very little is bound by EPS.[218] Since biofilms are known to accumulate salt ions from the surrounding medium—up to 27 times more than in the bulk solution[218]—production of charged solutes and EPS would result in a concurrent accumulation of bound water.

Many studies have shown that when ions associate with molecules of opposite charge, they do so by specifically adsorbing: either with the loss of part of their solvation shell, or by forming an outer-sphere complex where part of their hydration shell is shared with the molecule they are solvating.[21–23,219] In either case, what results is a break in the inversion symmetry of the hydration shell, making these solvation waters SFG-active. This would also be the case for ions sequestered by EPS and other charged metabolites produced by growing bacteria. As shown in Fig. 5.7, as cells adhere to or sense the silica surface, increased production of charged EPS would result in more ions in the microenvironment. Since the majority of these ions are associated with oppositely charged regions on EPS,

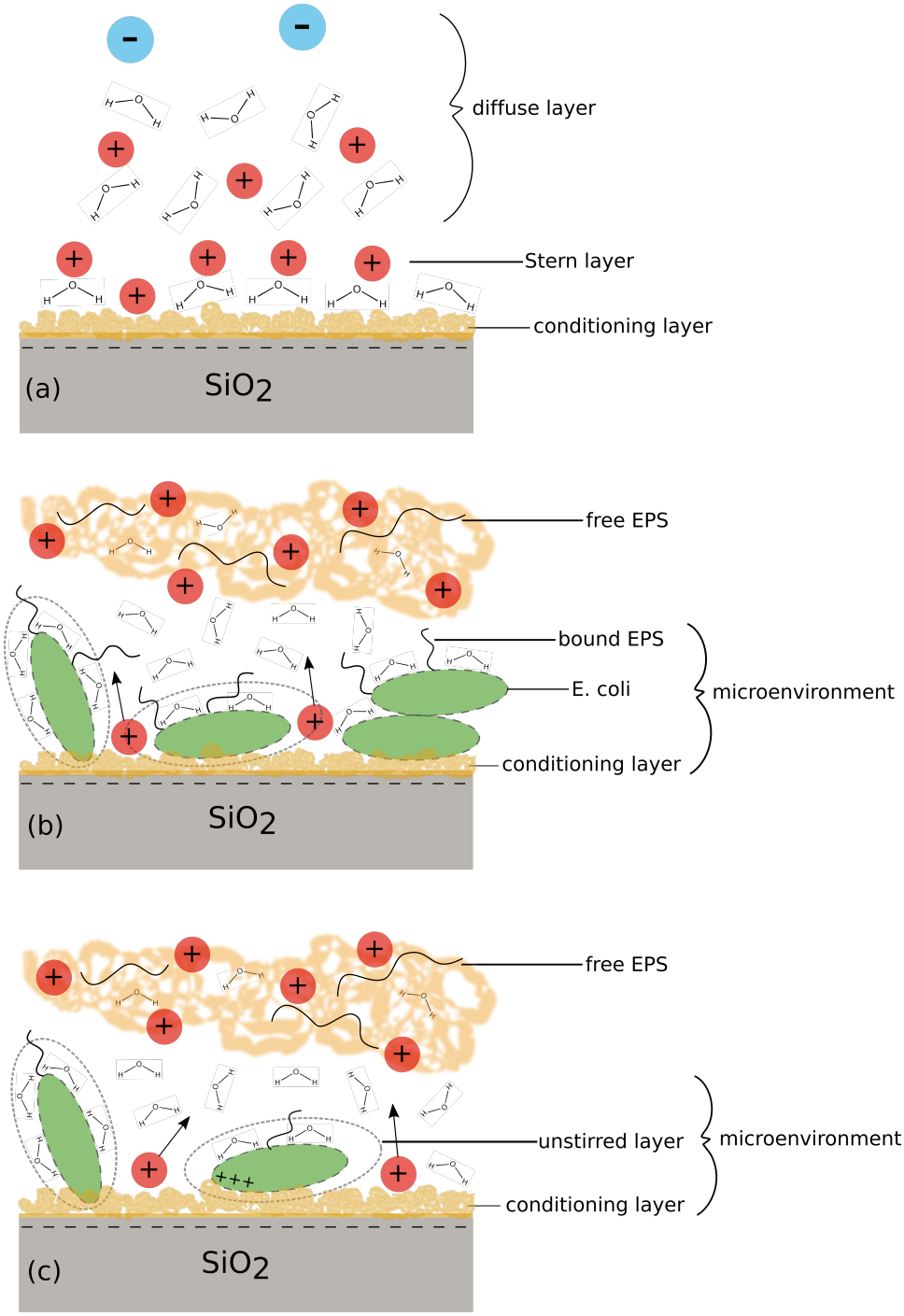

Figure 5.6: Schematic illustrating (a) bare silica in LB growth medium; (b) the microenvironment upon adhesion of untreated *E. coli*; and (c) the microenvironment upon adhesion of CER-treated *E. coli*.

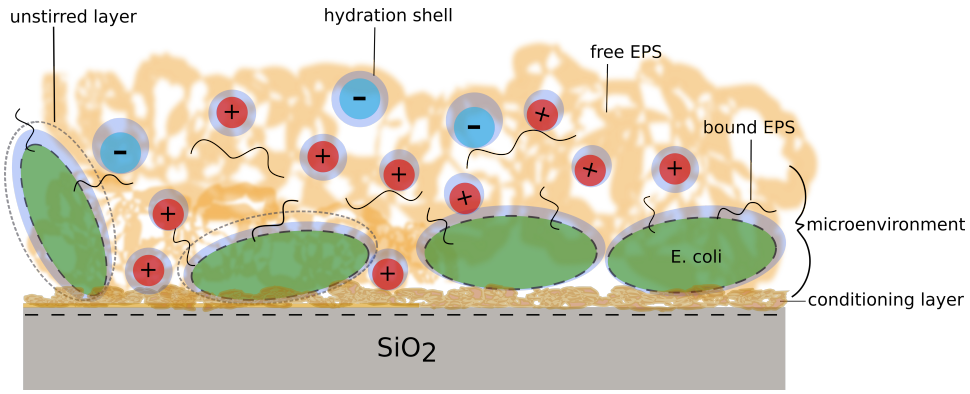

Figure 5.7: Schematic illustrating the increase in ordered water in the hydration shells surrounding solutes attracted to EPS and *E. coli*.

their hydration shell would become distorted, resulting in their contribution to the SFG signal. Thus, as more EPS are produced over time, the increasing number of non-centrosymmetric hydration shell waters could contribute to the observed increase in the SFG signal intensity. This hypothesis is supported by other SFG studies, which have shown that interfacial water structure can be predominately the consequence of macromolecule-ion interactions.[220]

Similar to the previous hypothesis, the increasing concentration of EPS and therefore solvated ions within the microenvironment would not necessarily be correlated with the number of cells adhered to the surface. It would be correlated with the concentration of charged EPS and other solutes near the surface, which would increase with both the number of reversibly and irreversibly adhered cells, as well as with the number of cells simply interacting with the surface in some way.

5.4 Conclusions

Vibrational SFG experiments on both untreated and CER-treated *E. coli*, coupled with in situ cell population measurements and imaging, revealed that the increase in SFG intensity is independent of bulk cell density, surface coverage, and the presence of bound EPS on the outer membrane. Zeta potential measurements on silica beads showed increasingly

positive potentials when *E. coli* and then CER-treated *E. coli* were adhered, ruling out the possibility that an increasingly negative surface charge upon cell adhesion is responsible for the trend in SFG intensity. Probing different locations on the surface resulted in no change in the SFG response of interfacial water, suggesting that slight changes in the surface charge density as a result of cell adhesion and EPS production do not influence the SFG signal. The remaining possibility, which does not rely on surface coverage or bound EPS, is that cells near the surface produce charged EPS, outer membrane vesicles, and other osmolytes that attract ions from the surrounding environment. In combination with the unstirred layer surrounding the cells, this effectively creates ion and pH gradients distinct from the bulk solution. This may influence the surface water response by: reducing screening of the increasingly negative surface charge on silica, or by increasing the number of hydration waters in the solvation shells of solute ions, both of which would increase the SFG intensity.

Chapter 6

Solvent Isotope Effect on Biomolecular Adsorption at Hydrophobic Surfaces[1]

6.1 Introduction

An understanding of the interaction of molecules in solution with hydrophobic surfaces is of fundamental importance to the enhanced biocompatibility of materials used for medical implants,[221–223] bio-separation and purification technologies,[224–229] and the development of biosensors.[230–232] The adsorption of proteins onto polymers is a multi-faceted phenomenon that is governed by the chemical composition and solution structure of the protein, the nature of the polymer substrate, temperature, pH, and the presence of other solutes. One of the challenges associated with characterizing adsorption at solid–liquid interfaces is achieving sufficient specificity for the surface in the presence of the adjacent bulk substrate and solution phases.

There has been considerable development in the quantitative analysis of SFG spectra to reveal the orientation and orientational distribution of interfacial molecules.[233] However, it is often challenging to separate effects arising from the number of molecules at the interface from those due to the arrangement of the molecules. For example, decreasing the number of molecules, or reducing their polar order parameter will both result in a decrease in $\chi^{(2)}$

[1]This was a collaborative project where I performed the QCM-D measurements, Kailash Jena performed the SFG measurements, and Dennis Hore carried out the spectral modeling and QCM-D modelling. Dennis and I analyzed and interpreted the data.

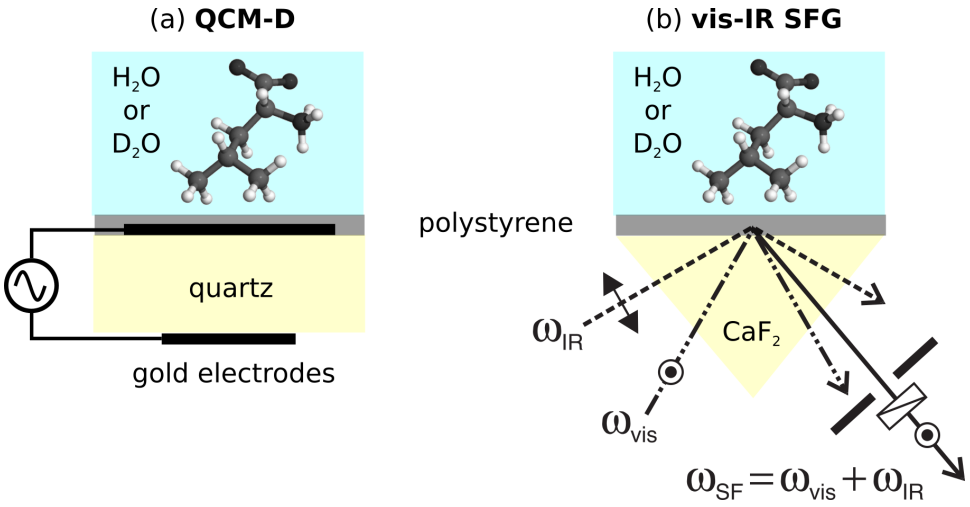

Figure 6.1: (a) QCM-D experiment with polystyrene-coated sensor surfaces next to leucine solutions. (b) SFG experimental geometry illustrating a p-polarized IR beam and s-polarized visible beam approaching an aqueous solution from within a polymer film. In the illustrated configuration, the s-component of the reflected SFG beam is detected, and recorded as a function of the incident IR energy. Reprinted with permission from Ref. 49. Copyright 2017 American Chemical Society.

and therefore a reduction in SFG intensity. Thus, a complementary technique is needed to attribute changes in signal intensity to either alignment or population differences. We use a combination of QCM-D and vibrational SFG measurements to study leucine adsorption onto polystyrene surfaces from solutions of H_2O and D_2O (Fig. 6.1). We will illustrate that the ratio of adsorbed masses from the two solvents, obtained through Voigt modeling of the frequency and dissipation shift data, accounts for the marked difference in SFG spectra recorded for leucine at polystyrene–water and polystyrene–D_2O interfaces.

6.2 Results and Discussion

6.2.1 QCM-D

Fitting the QCM-D Data. Fig. 6.2 illustrates the frequency ($\Delta f_n/n$) and dissipation (ΔD_n) shifts after pure D_2O and H_2O were replaced with heavy and light leucine–water solutions. (Note that we are following the convention that this normalization to the harmonic number n is explicit for Δf, but implicit for ΔD based on the expressions as they appear in Eq. 2.7.)

Data for the fundamental ($n = 1$) are not used as a result of mounting stress effects, as is typical for QCM experiments. The penetration depth of the acoustic wave at each frequency varies as a result of the bulk density and viscosity changes going from H_2O and D_2O to leucine solutions, as well as any adsorbed, solvent-associated leucine molecules that couple to the polystyrene surface and dampen the oscillation. Lower harmonics have a greater penetration depth than higher harmonics, as indicated by Eq. 2.8. We should clarify that the time dependence of these signals, of central interest to most QCM-D studies, has no significance for us. This is because the adsorption is faster than the mixing time in the pump chamber. Any apparent changes in Δf and ΔD with time are largely due to the difference in bulk liquid properties as the pure solvent is replaced with solution inside the chamber. Using code developed in-house, data for the six harmonics were fit to Eq. 2.10 to extract the adsorbed layer thickness h_1, shear viscosity η_1, and shear elastic modulus μ_1. To account for changes in the bulk liquid properties as a result of the relatively high concentration of the leucine solution, the bulk viscosity of the leucine–H_2O and leucine–D_2O solutions were also fit using our measured bulk solution densities of $\rho_2 = 999.2$ kg/m^3 and 1108 kg/m^3 respectively. These values were obtained by weighing solutions of known concentration prepared in volumetric flasks.

The difference between the calculated (solid circles in Fig. 6.2) and experimental values (open circles in Fig. 6.2) was minimized using a truncated Newton's method.[234] Resulting parameters are shown in Table 6.1. One notices that the layer viscosities, in both H_2O and D_2O, are similar to that of the bulk solutions, indicating that the adsorbed layer is liquid-like. The loss tangent $\omega\eta/\mu$ was calculated to be ≈ 1.5 for H_2O and ≈ 2 for D_2O, at the fundamental frequency ω. These values are in the range of what has been reported for adsorption of other species from aqueous solutions,[235,236] including the similarity between the values in the two solvents.[235]

Implication for Surface Coverage. The values returned by the fitting also enable us to calculate the adsorbed mass of the leucine layer in H_2O as 153 ± 28 ng/cm^2, and

Property	Symbol	H_2O value	D_2O value	Units	Source
quartz frequency	f_0	4.958×10^6	4.952×10^6	s^{-1}	measured
quartz thickness	h_0	302.5×10^{-6}	302.9×10^{-6}	m	derived
quartz density	ρ_0	2648	2648	$kg{\cdot}m^{-3}$	literature
solvent density	ρ_2	997.5	1107	$kg{\cdot}m^{-3}$	literature
solvent viscosity	η_2	8.9×10^{-4}	1.25×10^{-3}	$kg{\cdot}m^{-1}{\cdot}s^{-1}$	literature
solution density	ρ_2	999.2	1108	$kg{\cdot}m^{-3}$	measured
solution viscosity	η_2	$(9.538 \pm 0.477) \times 10^{-4}$	$(1.296 \pm 0.065) \times 10^{-3}$	$kg{\cdot}m^{-1}{\cdot}s^{-1}$	fit
layer density	ρ_1	1020	1127	$kg{\cdot}m^{-3}$	assumed
layer viscosity	η_1	$(9.748 \pm 1.755) \times 10^{-4}$	$(1.348 \pm 0.243) \times 10^{-3}$	$kg{\cdot}m^{-1}{\cdot}s^{-1}$	fit
layer shear modulus	μ_1	$(2.005 \pm 0.441) \times 10^4$	$(2.016 \pm 0.444) \times 10^4$	$kg{\cdot}m^{-1}{\cdot}s^{-2}$	fit
loss tangent at 5 MHz	$\tan\delta$	1.515	2.081		calculated
layer thickness	h_1	$(1.5 \pm 0.2) \times 10^{-9}$	$(3.0 \pm 0.4) \times 10^{-9}$	m	fit
adsorbed mass	m	153 ± 28	339 ± 58	$ng{\cdot}cm^{-2}$	calculated

Table 6.1: Parameters used to fit the QCM-D data appearing in Fig. 6.2 to Eq. 2.10.

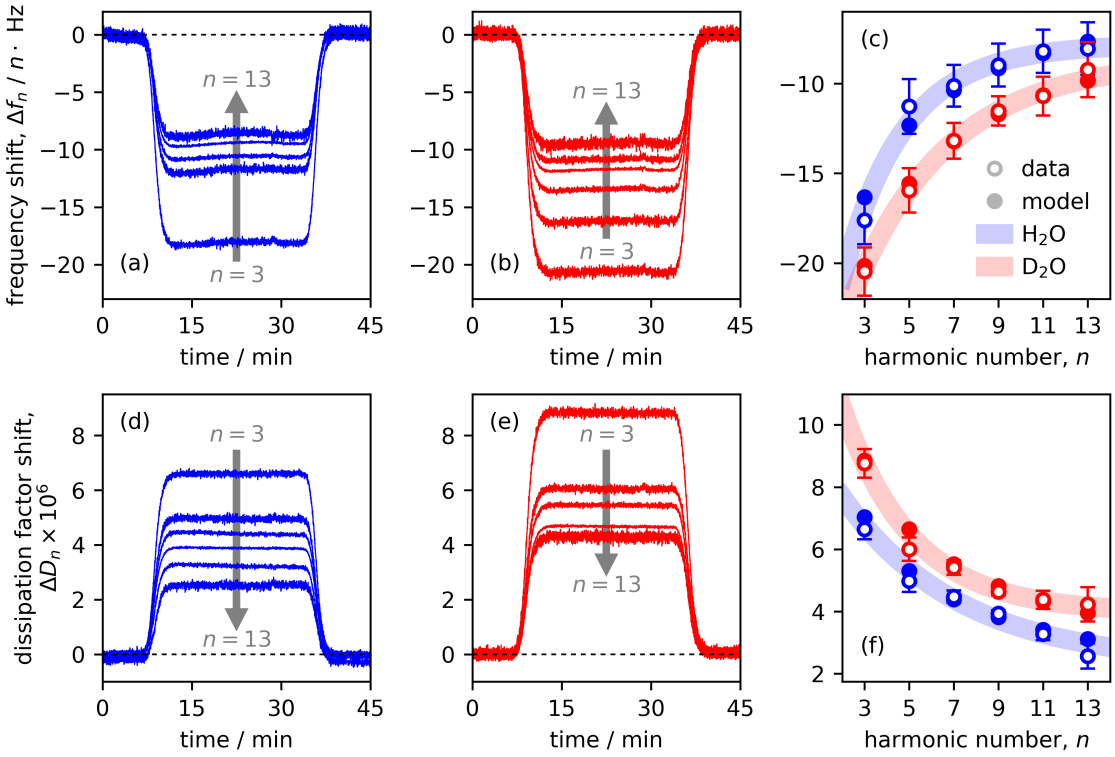

Figure 6.2: (a)–(c) Measured equilibrium frequency shifts, normalized to the harmonic n, on polystyrene-coated quartz sensors when the environment is changed from H_2O to a 0.17 M solution of leucine in H_2O (blue traces and open circles in (c)), and from D_2O to a 0.17 M solution of leucine in D_2O (red traces and open circles in (c)). (d)–(f) Simultaneously measured shift in dissipation factor. In all cases, filled circles are the result of fitting to the model in Eq. 2.10. Error bars indicate one standard deviation. Reprinted with permission from Ref. 49. Copyright 2017 American Chemical Society.

339 ± 58 ng/cm^2 in D_2O. We can provide some further insight into these values by considering how they translate into surface coverage. It has been shown that leucine prefers to adopt a standing conformation at the polystyrene–water interface, rather than one lying flat on the surface.[147] This is because a standing conformation minimizes interactions between the hydrophobic alkyl groups and the hydrophilic, charged amino and ester moieties. Moreover, the alkyl groups are able to occupy regions of lower solvent density nearer the surface, while allowing the zwitterionic portion of the amino acid to be more solvated by the bulk solution. This effect would be enhanced in D_2O since there would be a greater energetic penalty for disrupting the O–D bonding network; thus, the

leucine molecules would be more inclined to orient in a standing conformation near the surface, leading to greater adsorption at the interface. Taking this proposed geometry into account from the structures in the simulations,[147] we assume an elliptical footprint with major axis ≈ 4 Å and minor axis ≈ 2 Å, resulting in an area of ≈ 6.3 Å^2. The adsorbed masses therefore correspond to 98% and 44% surface coverage for leucine in D_2O and H_2O, respectively. In light of the above, the formation of a near monolayer in the case of D_2O seems reasonable based on its increased preference for a standing orientation, resulting in a greater packing of the leucine molecules at the surface. In H_2O, where less adsorption occurs, since the leucine molecules still prefer a standing conformation at the hydrophobic surface, less than monolayer coverage is achieved.

Difference in Adsorbed Mass. Since the structure of the solvent plays a crucial role in the adsorption of amino acids, it is important to consider the effects of the water/D_2O solvation environment on leucine adsorption. For a nonpolar amino acid like leucine adsorbing to a hydrophobic surface, the major driving force is the hydrophobic interactions between the side chain (in particular, the terminal methyl groups) and the substrate. It has been shown that the attractive potential exhibited by hydrophobic surfaces is too weak to hold solvent molecules close to the surface, resulting in a region of low solvent density very near the interface.[146,237] This serves to promote leucine adsorption by allowing it to place its nonpolar side chain in regions of low solvent density, where it will disrupt fewer solvent–solvent interactions than in the bulk, in accordance with the hydrophobic effect.[238] Therefore, the greater adsorption of leucine from D_2O is reasonable based on its lower solubility compared to water.[239] This arises as a result of the greater strength of the bonding network in D_2O. Since the O-D–O bond is stronger than the corresponding hydrogen bond in water, rupturing of this bond in order to interact with the charged amine and carboxyl group in leucine is more difficult, which leads to decreased hydration.[240] Thus, since the energetic penalty of solvation by D_2O is so high, leucine is more likely to reduce exposure of its nonpolar side chain, first by placing it

in regions of lower solvent density near the surface, and eventually associating with the nonpolar polystyrene surface, in order to minimize its disruptive effect on the solvent bonding network. This phenomenon would be more pronounced in D_2O than in H_2O. Moreover, the strength of the hydrophobic interaction would be greater in D_2O than in H_2O, according to previous studies.[239] Another important factor when considering the adsorption of leucine to polystyrene is the differential orientation of water and D_2O at the interface, as a result of quantum nuclear effects. Studies have shown that O–H bonds preferentially orient toward the air/water interface (a model hydrophobic surface) while O–D bonds orient toward the bulk.[241] In addition to solvation environment effects on leucine adsorption, these orientation differences between H_2O and D_2O at the interface likely play a significant role in its preferential adsorption from D_2O, where there are fewer dangling O–D bonds to interact with leucine's side chains, thereby enhancing its surface adsorption capability.[242] We further note that, since our solutions are not buffered, variations in pH may also contribute to differences in adsorbed amount.

6.2.2 SFG

Surface Field Corrections for SFG Spectra. Literature refractive index data for polystyrene,[243] CaF_2,[244] H_2O,[171] and D_2O[245] were used to calculate the surface fields. The real and imaginary components of the water and D_2O refractive index are plotted in Fig. 6.3a and b. As Eq. 2.4 indicates, the relevant correction involves the square of the product of the local field factors, as plotted in Fig. 6.3c. The SFG spectra we present are corrected for these factors, which can vary considerably between the two solvents according to the wavelengths, polarization of the fields, and beam angles. Our results are therefore proportional to $|\chi^{(2)}(\omega_{\mathrm{IR}})|^2$, as the other factors that depend on ω_{IR} have been removed and we are directly comparing the water and D_2O $|\chi^{(2)}_{yyz}|^2$ spectra. These factors are highly sensitive to the polarization of the beams, and the angle of the incident fields. For our experimental geometry, Fig. 6.3 illustrates that the relative correction is in the range

0.5–1.5, and has a significant frequency dependence.

Fitting the SFG Spectra. Fig. 6.4a shows the SFG spectra of 0.17 M leucine at the polystyrene–D_2O interface (red points), and the control experiment in the absence of leucine (black points). A qualitative inspection of the data reveals that alkyl stretching modes are very prominent in the 2800–3000 cm^{-1} region. One of the unique features of nonlinear vibrational spectroscopy is that the response is coherent. As a result, the line shape is obtained by summing over the amplitude and phase of each oscillator/mode prior to squaring the result to obtain the spectral intensity (Eq. 2.2). A simple summation over Lorenztians may be used for the dominant modes when a homogeneous lineshape is assumed,

$$\chi^{(2)}_{\text{Leu}} = \sum_{q=1}^{4} \frac{A_q}{\omega_{\text{IR}} - \omega_q + i\Gamma_q}. \tag{6.1}$$

For each normal mode q we consider ω_{IR} is the incident IR frequency, ω_q is the normal mode frequency, $i = \sqrt{-1}$, Γ_q is the homogeneous line width, and the numerator A_q is the ensemble-averaged product of IR transition dipole moment and Raman transition polarizability. Values of these parameters obtained from a fit to the data (red line in Fig. 6.4a) are shown in Table 6.2.

q	ω_q / cm^{-1}	A_q	$\Gamma_{h,q}$ / cm^{-1}	$\Gamma_{i,q}$ / cm^{-1}
1	2852	−2.7	5.5	—
2	2870	−4.6	5.7	—
3	2900	−4.4	15	—
4	2935	−6.8	10	—
5	3200	0.2	5	95
6	3400	0.02	5	50

Table 6.2: Parameters used to fit the leucine in D_2O on polystyrene data appearing in Fig. 6.4a to Eq. 6.1 (q = 1–4) and water on polystyrene data from Fig. 6.4b to Eq. 6.2 (q = 5 and 6).

In the presence of water, the spectra look remarkably different. Fig. 6.4b shows the baseline polystyrene–water response (black points) and in the presence of 0.17 M leucine (blue points). The overall reduction in intensity upon the addition of solute is typical for many osmolytes, attributed to a disruption of the interfacial hydrogen bonding

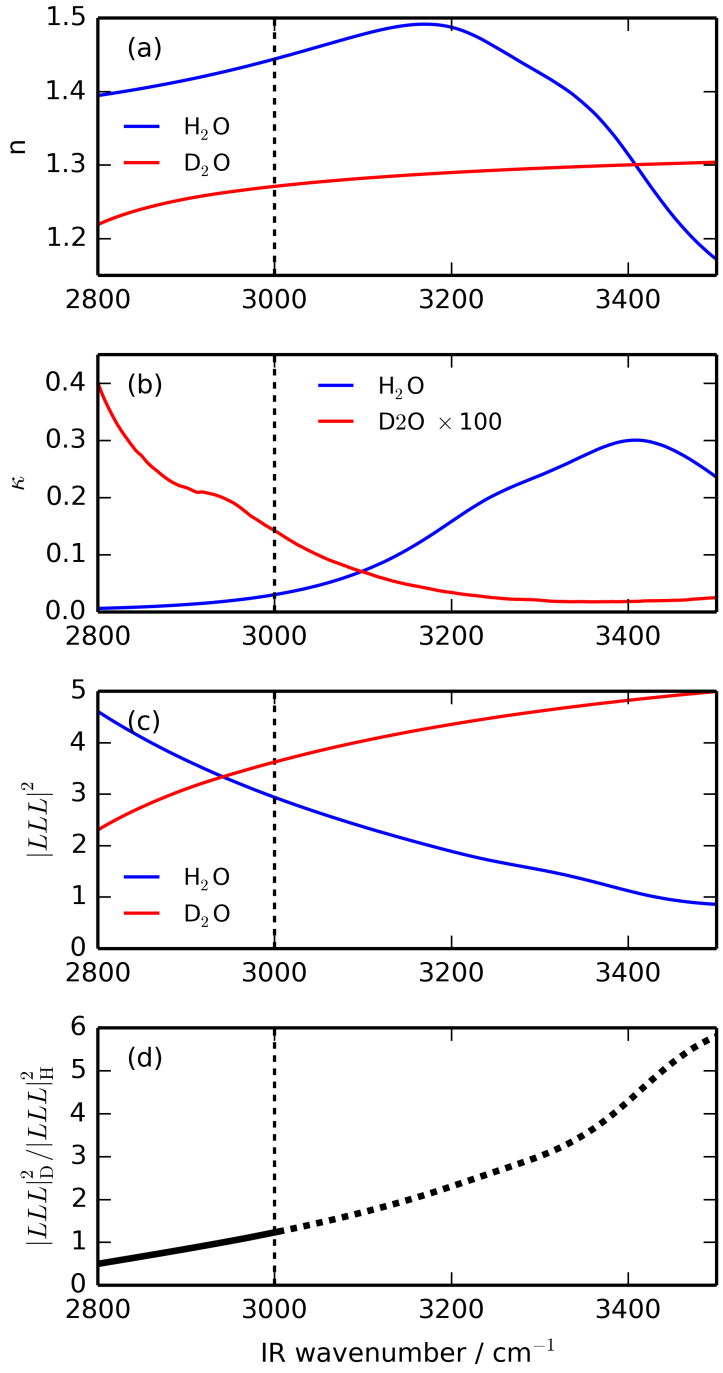

Figure 6.3: (a) Real part of the water (blue) and D_2O (red) refractive index, (b) imaginary part of the refractive indices, (c) corresponding local field correction to the SFG intensity, (d) ratio of the D_2O/H_2O corrections. Reprinted with permission from Ref. 49. Copyright 2017 American Chemical Society.

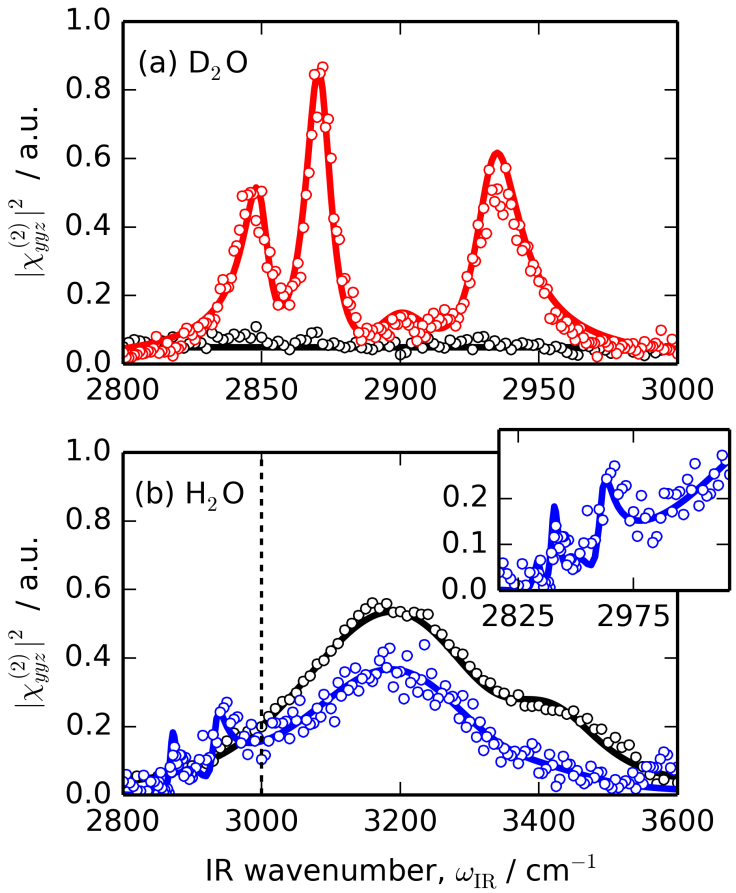

Figure 6.4: (a) SFG intensity spectrum of leucine in D_2O adsorbed at the polystyrene surface (red points), fit to a model based on Eq. 6.1. The neat polystyrene–D_2O interface is shown in black. (b) SFG spectrum of leucine in H_2O at the polystyrene surface (blue points), superimposed on the model created using Eq. 6.3 (blue line) The neat polystyrene–water interface is shown in black. The inset displays an enlarged portion of the 2800–3000 cm^{-1} region. Reprinted with permission from Ref. 49. Copyright 2017 American Chemical Society.

network.[220,246] The leucine spectrum illustrates that, in addition to the broad response of the interfacial O–H stretching modes spanning nearly 1000 cm^{-1}, the alkyl modes are much less prevalent. The coherent nature of the SFG response doesn't necessarily 'bury' low amplitude modes in the presence of large background signals, as would occur in IR absorption or Raman scattering spectra. In SFG spectroscopy, such interference typically leads to amplification of the signal as a result of the water–leucine cross term in $|\chi^{(2)}|^2$. The fact that the leucine modes appear weaker in water therefore points to the possibility

that the adsorbed quantity and/or structure may be different from that in D_2O. We already know from the QCM-D data that there is roughly half the quantity of leucine on the surface in the case of water. We now use this information together with our SFG data to further interpret the spectra.

The inhomogeneous OH lineshape may be accounted for with a convolution of Lorenztian and Gaussian profiles,

$$\chi^{(2)}_{\text{water}} = \sum_{q=5}^{6} \int_0^{\infty} \frac{A_q}{\omega_{\text{IR}} - \omega_L + i\Gamma_{h,q}} \exp\left[\frac{(\omega_q - \omega_L)^2}{2\Gamma^2_{i,q}}\right] \mathrm{d}\omega_L \tag{6.2}$$

where Γ_i is the inhomogeneous line width, and ω_L is the variable over which the integral is evaluated. In such cases, the homogeneous line widths Γ_h are typically fixed at values determined from vibrational dephasing lifetime experiments (here we have used $\Gamma_h = 5$ cm^{-1}). The broad features in the 3000–3500 cm^{-1} region are due to the multitude of water O–H stretching environments. We have modelled this water response using two bands, centered at 3200 cm^{-1} and 3400 cm^{-1}. The leucine C–H modes may be clearly observed in the 2800–3000 cm^{-1} region, but their amplitudes are not significant enough to uniquely fit the peaks using a homogeneous model as was done in the case of D_2O. Such modest intensity is typical of C–H stretching modes of amino acids adsorbed onto polystyrene in water.[247] We therefore model the leucine/water response using

$$\chi^{(2)}_{\text{Leu}-\text{water}} = \chi^{(2)}_{\text{water}} + r \cdot \chi^{(2)}_{\text{Leu}} \tag{6.3}$$

where r represents the fraction of the population of leucine on the surface in water compared to that in D_2O. This can be obtained from the adsorbed mass of leucine on polystyrene in water (m_{H} in Table 6.1) and in D_2O (m_{D}), resulting in $r = m_{\text{H}}/m_{\text{D}} = 0.45$. The spectrum predicted by Eq. 6.3 is indicated by the solid blue line in Fig. 6.4b. One can notice that the agreement with the measured spectra (points in Fig. 6.4b) is reasonable, including the apparent difference in the relative C–H mode strength as a result of their coherent superposition with the tailing of the hydrogen-bonded water O–H modes in the same region (enlarged in the inset to Fig. 6.4b). This indicates that the difference in

intensity and overall appearance of the leucine H_2O compared to D_2O spectra may be attributed to a difference in the population of leucine on the polystyrene surface, with negligible difference in surface-adsorbed structure for the adsorbate between the two interfacial solvation environments.

6.2.3 Implications for the Role of Solvent in Biomolecular Adsorption

Our finding that the structure of leucine adsorbed to polystyrene is similar, whether the solvent is H_2O or D_2O, raises interesting questions on the role of solvent in the adsorption and structuring of biomolecules at surfaces. Although it is recognized that the solvent structure in the first 10–15 Å is highly dependent on the chemical and physical properties of the surface,[188,248] there is surprisingly little evidence of how this affects the molecules in their adsorbed state. A molecular dynamics simulation of leucine in water adsorbed onto surfaces of varying hydrophobicity indicated that, as the hydrophobicity of the substrate increased, the surface water structure in the presence of adsorbed leucine has increasing similarity to that in the absence of leucine.[146] Studies of a diverse sampling of amino acid and peptide adsorption at both hydrophobic and hydrophilic surfaces illustrate that side chain composition, polarity, length, charge, and conformation heavily influence the extent of amino acid/peptide adsorption and surface structure.[157,158] In particular, it was found that the amphiphilic peptide LKα14 (comprised of leucine and lysine residues) preferentially adsorbed to polystyrene via hydrophobic interactions through the dehydrated leucine side chains, while electrostatic interactions of the positively charged lysine side chain dictated adsorption behaviour to a hydrophilic silica surface.[158] Other studies report that adsorption of peptides can have a marked influence on interfacial water structure, as evidenced by changes in the signal intensity and ratio of the 3200 cm^{-1} versus 3400 cm^{-1} peaks in SFG spectra.[160] This highlights the role that solvent structure plays in the adsorption of biomolecules, and the close relationship between interfacial solvent structure and adsorbate structure. In addition to structural considerations, vibrational energy transfer

and dissipation dynamics at the aqueous interface are known to be integral to adhesion processes.[249] It has been shown that interfacial energy transfer in D_2O occurs through rapid and efficient transfer of vibrational energy through the O–D stretching mode, both along the surface and into the bulk, and that these interfacial dynamics are slower in D_2O than in H_2O but are unique to water.[250] The variability among amino acids, peptides, and proteins in terms of adsorption tendencies and strength, conformational changes upon adhesion, structure and orientation at the surface, and reversibility of adsorption require further investigation into the role of solvent in biomolecular adsorption at surfaces.

6.3 Conclusions

Dissipation-monitoring quartz crystal microbalance and vibrational sum frequency generation spectroscopy were used to study the adsorption of a hydrophobic amino acid onto a hydrophobic surface in the presence of H_2O and D_2O. Analysis of the QCM-D data using a Kevin–Voigt model to account for the viscoelastic response of the damped surface environment resulted in the conclusion that more than twice as much leucine was adsorbed onto polystyrene when the solvent was D_2O. When the specific ratio of H_2O:D_2O leucine surface mass was used in a model of the second-order nonlinear response, the intensity and overall appearance of the SFG spectral features was entirely accounted for. This is evidence for similar adsorbed structure in the two different solvent environments, highlighting the role of solvent in dictating the adsorbed quantity while not altering the interfacial structure at hydrophobic surfaces. This data supports the suitability of substituting D_2O for H_2O in spectroscopic studies of biological adsorption at hydrophobic surfaces. The extreme sensitivity of SFG towards molecular orientation, in conjunction with the mass sensitivity of QCM-D, make these techniques complementary for characterizing adsorption and structure at surfaces.

Chapter 7

Conclusions

7.1 Summary of Work

Characterization of the Silica–Water Interface. Vibrational SFG experiments at the silica–water interface using different beam polarization combinations showed the presence of two distinct populations of water in the EDL whose response to changes in bulk ionic strength and pH conditions differed. SFG and simulation results showed that the observed 3200 cm^{-1} peak corresponded to water molecules in the diffuse layer (further from the surface) while the 3400 cm^{-1} mode is sensitive to water in the Stern layer, adjacent to the surface. These two populations were probed using the ssp or ppp and pss polarization combinations, respectively. In the presence of high salt concentrations, the orienting forces acting on each water population were observed to be very different when the pH was varied. These results are consistent with the presence of oriented water, even at low pH near the point-of-zero charge for silica. This could be due to: (1) a positive potential as a result of overcharging of the EDL or (2) specific interactions of hydrated cations with the surface. These results provide new insight into the structure of distinct water populations in the EDL at high salt concentrations, where a Stern layer is present.

Water as a Reporter of Surface Conditions during Bacterial Growth and Adhesion to Silica. When the growth of *E. coli* K12 in the presence of a silica surface was monitored using vibrational SFG spectroscopy, a continual increase in the interfacial water O-H

stretching was observed, followed by a plateau after 25 h of growth. Combining SFG experiments with concurrent growth curve and imaging data exposed the delay in the monotonic increase in SFG intensity compared to bulk cell population growth, and its independence from the extent of *E. coli* adhesion to silica. It was also found that removing bound EPS from the outer membrane did not affect the trend in interfacial water signal during bacterial growth. Zeta potential measurements of normal and CER-treated bacteria adhered to silica beads showed increasingly less negative values. These results, coupled with SFG experiments probing the water response at different positions on the prism, revealed that changes in the surface charge or surface charge density with cell and EPS adhesion could not account for the evolution of the SFG signal with time. Consequently, the remaining possibility to explain the increase in SFG intensity with cell growth is an alteration of the pH and ionic strength of the microenvironment near the surface. Unique ionic gradients may be established in this region due to accumulation and diffusion of charged EPS and outer membrane vesicles, which would attract counterions from the surrounding environment. This could increase the SFG response from diffuse waters either by reducing screening of the negative surface charge, or by increasing the number of hydration waters in the solvation shells of adsorbed ions. These ion sponge effects would only occur after cells have interacted with the surface, inducing the production of these charged solutes that could then establish ionic gradients over time, even in regions with few or no cells adhered. Moreover, the unstirred layer surrounding cells—especially those individually adhered—also possesses distinct pH and ionic strength gradients, which may further contribute to altering the solution conditions in the microenvironment. The alkalinity of this microenvironment would also increase as a result of accumulation of positively charged metabolites, thereby contributing to a more negative surface charge due to deprotonation of silanols. Bulk ionic strength and pH measurements showed small changes that were not sufficient to account for the magnitude of the observed increase in SFG intensity. However, the formation of a microenvironment at the surface produced

by adhered cells, EPS, and metabolites, as well as the ions associated with them, could produce a local ionic strength that is significantly different from the bulk solution.

Solvent Isotope Effect on Biomolecular Adsorption at Hydrophobic Surfaces. In vibrational spectroscopic studies of biological systems, oftentimes D_2O is substituted for H_2O in order to more clearly resolve the amide I and alkyl stretching regions. However, in interfacial studies where adsorption is involved, the interchangeability of H_2O and D_2O may not be straightforward, as the two solvents may have a significant impact on the amount adsorbed and/or the adsorbed structure. Nonlinear vibrational spectroscopy of leucine in H_2O and D_2O showed marked differences in the alkyl stretching region of this amino acid when adsorbed onto polystyrene. A quartz crystal microbalance with dissipation monitoring revealed that more than twice the amount of leucine was adsorbed onto the surface when the solvent was D_2O. When this ratio of adsorbed surface mass in D_2O versus H_2O was used to model the second-order nonlinear response, both the intensity and the overall appearance of the SFG spectral features were entirely accounted for. This indicates that the marked spectral differences in the two solvent environments are a result of changes in the population of leucine at the surface, and not a result of changes in its adsorbed structure. This highlights the importance of solvent in biomolecular adsorption at hydrophobic surfaces, and its role in dictating the amount adsorbed, while not altering the interfacial structure.

7.2 Perspective

Understanding the adsorption of molecules onto surfaces is integral to a wide variety of fields with scientific, engineering, and industrial applications. Using nonlinear optical techniques, we have shown how interfacial water provides a unique window into various adhesion processes to surfaces, including the structure of different water populations in the EDL at silica, biomolecular adhesion to polystyrene in different solvents, as well as the surface microenvironment during bacterial adhesion to silica. These studies underline the

importance of surface water in governing the structure of adhered molecules, in mediating changes in the interfacial environment as a result of adhesion, and provide insight into a nanoscale region that is otherwise difficult to query. They also illustrate the importance of combining surface-sensitive and bulk probes with microscopic techniques to gain a better understanding of what happens at surfaces when ions, biomolecules, and cells are involved in adhesion.

Despite the prominent role it plays in mediating cell adhesion and biofilm formation, water is often neglected in such studies, due in part to the paucity of techniques capable of probing interfacial water exclusively. Vibrational SFG experiments performed here are unique in their ability to overcome this challenge, and highlight the role of solution conditions at the surface in cell attachment and biofilm growth. Changes in the nonlinear vibrational response of interfacial water reflect changes occurring in the pH and ionic strength only at the surface, due to the presence of polymeric adhesives, metabolites, and other solutes secreted by bacteria. The use of SFG to probe the interfacial environment during bacterial adhesion is new for the biofilm community, which mostly uses vibrational techniques such as ATR-IR and Raman scattering to study biofilm composition near the surface.

We have also highlighted the possibility of obtaining qualitative information from SFG spectra. This represents a shift for the nonlinear vibrational spectroscopy community, where it has been established that the study of small molecules with known composition can yield remarkable quantitative detail about orientation, conformation, and the surface orientation distribution.[233,251] In contrast, by examining trends in spectral intensity changes, SFG spectra can be used to obtain information about changes occurring in the interfacial environment. The insight into biomolecular and cell adhesion processes—including biofilm formation—that can be gained from using these nonlinear optical techniques, and combining them with other bulk probes and microscopy methods, provides powerful tools for studying these systems. This is especially true at solid–aqueous

interfaces where water is integral in mediating adhesion and its response can be used to investigate interfacial processes that occur in a wide variety of biologically, chemically, and industrially relevant systems.

7.3 Future Work

Further work is needed to determine the extent of ionic strength and pH changes in the microenvironment during cell growth. To analyze concentration gradients of ions in the unstirred layer around cells and in the microenvironment, electrochemical methods that employ glass microelectrodes with various ion exchangers may be used. A more recently developed method, called scanning ion-conductance microscopy (SICM), may be able to overcome the difficulty many conventional electrochemical techniques have with planar mapping of small ion concentrations.[133] In fact, certain systems could enable 3D mapping of the ionic distribution in these layers at much higher resolution. To visualize the pH and ionic properties of the microenvironment, particularly the cellular unstirred layer, bioimaging probes could be used. These include calcium and sodium ion indicators such as fluo-4 and sodium-binding benzofuran isophthalate (SBFI), as well as pH sensors like BCECF. These probes may be conjugated to certain species that bind exclusively to membrane proteins, thereby preventing their diffusion into the bulk.[252]

In addition to measuring the pH and ionic strength of the microenvironment, it would also be useful to elucidate the extent of solution composition changes near the surface during cell growth and adhesion. This could be monitored using ATR-IR or confocal Raman spectroscopy. Confocal Raman microspectroscopy could be used to monitor protein conditioning of the surface, EPS production by adhered cells, and compositional changes in the microenvironment with colony formation and maturation. Others have been successful in monitoring the spatial and temporal distribution of biofilm components, by identifying increases in certain vibrational modes that correspond to EPS, DNA, lipids, and proteins.[253,254] The time evolution of bands assigned mainly to proteins, polysaccharides,

and nucleic acids can be used to track the accumulation of cells near the surface, while more in depth analysis of the entire spectral profile may provide insight into biochemical and structural changes occurring in the bacterial matrix near the surface, as a result of cell adhesion. In addition, Raman mapping can provide information about the spatial distribution of cells and biofilm components near the surface and extend the structural analysis by confocal microscopy with chemical information.

To determine whether EPS production by adhered cells contributes significantly to decreasing the ionic strength near the surface, a mutant strain of *E. coli* that does not produce EPS, or at least has reduced capability, could be used. If the concentration of these exopolymers is greatly reduced within the microenvironment and a corresponding decrease in the SFG intensity of interfacial water signal is observed, this would confirm the role that EPS plays in altering the solution conditions near the surface. However, caution should be taken when altering the genotype of bacteria as other cell properties may also change. For instance, one study using an EPS mutant strain of *E. coli* K12 found that stationary phase cells were more adhesive than mid-exponential phase cells.[138] This behaviour was attributed to an increase in charge heterogeneity on the outer membrane, leading to decreased electrostatic repulsion with the quartz surface. The authors also found that the number of polar functional groups on the cell surface (and thus charge density) was greater for mid-exponential phase cells, as a result of more outer membrane proteins and LPS-associated functional groups being present. This study was also performed under flow conditions, where nutrients were continually supplied to the growing bacteria, which could also influence the extent of adhesion and even biofilm formation. Thus, future studies should aim to systematically vary experimental conditions—including EPS production, nutrient availability, and flow rate—in order to determine unequivocally the influence they have on the microenvironment and thus evolution of interfacial water structure.

Imaging data taken after growth of *E. coli* K12 in the SFG sample holder and from analogous offline experiments showed a relatively homogeneously colonized surface;

however, it would be beneficial to know accurately the number of cells within the exact spot where the visible and IR beams are overlapped, and whether these are individual cells, or large or small clusters of cells. In the past, our group has built a microscope with the capability to perform simultaneous SFG spectroscopy. Using this setup, it would be possible to visualize the bacterial distribution on the surface and directly correlate this to evolution of the interfacial water signal.

Understanding the initial interactions of cells with surfaces is critical to gaining better insight into the mechanism of bacterial adhesion and colony formation. By simultaneously imaging and collecting surface-sensitive SFG and composition-sensitive Raman spectra, increases in adhered cells, metabolites, and EPS, and how these affect the interfacial microenvironment, can be monitored. This will allow for a more complete picture of bacterial adhesion and growth at surfaces, as changes in Raman band intensities or interfacial water structure in SFG spectra may result from specific morphological changes in adhered cells and colonies. This may lend insight into how compositional changes in the microenvironment develop with cell growth and adhesion, and how this influences water structure and colony formation at surfaces.

References

[1] Li, S.; Du, L.; Wei, Z.; Wang, W. *Sci. Total Environ.* **2017,** *580,* 1155–1161.

[2] Salta, M.; Wharton, J. A.; Blanche, Y.; Stokes, K. R.; Briand, J.-F. *Environ. Microbiol.* **2013,** *15,* 2879–2893.

[3] Crossley, S.; Faria, J.; Shen, M.; Resasco, D. E. *Science* **2010,** *327,* 68–72.

[4] Pratt, L. R.; Pohorille, A. *Chem. Rev.* **2002,** *102,* 2671–2692.

[5] Walker, D. S.; Hore, D. K.; Richmond, G. L. *J. Phys. Chem. B* **2006,** *110,* 20451–20459.

[6] Henderson, M. A. *Surf. Sci. Rep.* **2002,** *46,* 1–308.

[7] Rimola, A.; Costa, D.; Sodupe, M.; Lambert, J.-F.; Ugliengo, P. *Chem. Rev.* **2013,** *113,* 4216–4313.

[8] Schrader, A. M.; Monroe, J. I.; Sheil, R.; Dobbs, H. A.; Keller, T. J.; Li, Y.; Jain, S.; Shell, M. S.; Israelachvili, J. N.; Han, S. *PNAS* **2018,** *115,* 2890–2895.

[9] Papirer, E. *Adsorption on Silica Surfaces;* Marcel Dekker: New York, 2000.

[10] Iler, R. K. *The Chemistry of Silica: Solubility, Polymerization, Colloid and Surface Properties, and Biochemistry;* Wiley: New York, 1979.

[11] Behrens, S. H.; Grier, D. G. *J. Chem. Phys.* **2001,** *115,* 6716–6721.

[12] Hayes, P. L.; Malin, J. N.; nad F. M. Geiger, C. T. K. *J. Phys. Chem. A* **2008,** *112,* 660–668.

[13] Dove, P. M.; Craven, C. M. *Geochim. Cosmochim. Acta* **2005,** *69,* 4963–4970.

[14] Kitamura, A.; Fujiwara, K.; Yamamoto, T.; Nishikawa, S.; Moriyama, H. *J. Nucl. Sci. Technol.* **1999,** *36,* 1167–1175.

[15] Hassanali, A. A.; Singer, S. J. *J. Phys. Chem. B* **2007,** *111,* 11181–11193.

[16] Walczak, J. J.; Wang, L.; Bardy, S. L.; Feriancikova, L.; Li, J.; Xu, S. *Colloids Surf., B* **2012,** *90,* 129–136.

[17] Abdel-Fattah, T. M.; Haggai, S. M.; Mahmoud, M. E. *Chem. Eng. J.* **2011,** *175,* 117–123.

[18] Dove, P. M.; Han, N.; Wallace, A. F.; De Yoreo, J. J. *Am. J. Sci.* **1994,** *294,* 665–712.

[19] Sovago, M.; Campen, R. K.; Bakker, H. J.; Bonn, M. *Chem. Phys. Lett.* **2009,** *470,* 7–12.

[20] DeWalt-Kerian, E. L.; Kim, S.; Azam, M. S.; Zeng, H.; Liu, Q.; Gibbs, J. M. *J. Phys. Chem. Lett.* **2017,** *8,* 2855–2861.

[21] Darlington, A. M.; Jarisz, T. A.; DeWalt-Kerian, E. L.; Roy, S.; Kim, S.; Azam, M. S.; Hore, D. K.; Gibbs, J. M. *J. Phys. Chem. C* **2017,** *121,* 20229–20241.

[22] Dewan, S.; Yeganeh, M. S.; Borguet, E. *J. Phys. Chem. Lett.* **2013,** *4,* 1977–1982.

[23] Dewan, S.; Carnevale, V.; Bankura, A.; Eftekhari-Bafrooei, A.; Fiorin, G.; Klein, M. L.; Bourget, E. *Langmuir* **2014,** *30,* 8056–8065.

[24] Dishon, M.; Zohar, O.; Sivan, U. *Langmuir* **2011,** *27,* 12977–12984.

[25] Lovering, K. A.; Bertram, A. K.; Chou, K. C. *J. Phys. Chem. C* **2016,** *120,* 18099–18104.

[26] Lowe, B. M.; Maekawa, Y.; Shibuta, Y.; Sakata, T.; Skylarist, C. K.; Green, N. G. *Phys. Chem. Chem. Phys.* **2017,** *19,* 2687–2701.

[27] Schaefer, J.; Gonella, G.; Bonn, M.; Backus, E. H. G. *Phys. Chem. Chem. Phys.* **2017,** *19,* 16875–16880.

[28] Yang, Z.; Li, Q.; Chou, K. C. *J. Phys. Chem. C* **2009,** *113,* 8201–8205.

[29] York, R. L.; Mermut, O.; Phillips, D. C.; McCrea, K. R.; Ward, R. S.; Somorjai, G. A. *J. Phys. Chem. C* **2007,** *111,* 8866–8871.

[30] Solid–Liquid Interfaces. In *Fundamentals of Interface and Colloid Science*, Vol. 2; Lyklema, J., Ed.; Academic Press: San Diego, 1995.

[31] Brown, M. A.; Abbas, Z.; Kleibert, A.; Green, R. G.; Goel, A.; May, S.; Squires, T. M. *Phys. Rev. X* **2016,** *6,* 011007.

[32] Brown, M. A.; Goel, A.; Abbas, Z. *Angew. Chem. Int. Ed.* **55,** *2016,* 3790–3794.

[33] Grahame, D. C. *Chem. Rev.* **1947,** *41,* 441–501.

[34] Glawdel, T.; Ren, C. L. Zeta Potential Measurement. In *Encyclopedia of Microfluidics and Nanofluidics*; Springer: Boston, 2008.

[35] Smoluchowski, M. *Physik Z* **1916,** *17,* 557–571.

[36] Tsuneda, S.; Aikawa, H.; Hayashi, H.; Yuasa, A.; Hirata, A. *FEMS Microbiol. Lett.* **2003,** *223,* 287–292.

[37] Long, G.; Zhu, P.; Shen, Y.; Tong, M. *Environ. Sci. Technol.* **2009,** *43,* 2308–2314.

[38] Liu, Y.; Yang, C. H.; Li, J. *Environ. Sci. Technol.* **2007,** *41,* 198–205.

[39] Li, B.; Logan, B. E. *Colloids Surf., B* **2004,** *36,* 81–90.

[40] Sheng, X.; Ting, Y. P.; Pehkonen, S. O. *J. Colloid Interface Sci.* **2008,** *321,* 256–264.

[41] Sanders, R. S.; Chow, R. S.; Masliyah, J. H. *J. Colloid Interface Sci.* **1995,** *174,* 230–245.

[42] Zasloff, M. *Nature* **2002,** *415,* 389–395.

[43] Gray, J. J. *Cur. Op. Struc. Bio.* **2004,** *14,* 110–115.

[44] Clair, S. V. L.; Nguyen, K.; Chen, Z. *J. Adhes.* **2009,** *85,* 484–511.

[45] Damodaran, S. *Anal. Bioanal. Chem.* **2003,** *376,* 182–188.

[46] Servagent-Noinville, S.; Revault, M.; Quiquampoix, H.; Baron, M.-H. *J. Colloid Interface Sci.* **2000,** *221,* 273–283.

[47] Han, X. X.; Zhao, B.; Ozaki, Y. *Trends Anal. Chem.* **2012,** *38,* 67–78.

[48] Sigal, G. B.; Mrksich, M.; Whitesides, G. M. *J. Am. Chem. Soc.* **1998,** *120,* 3464–3473.

[49] Jarisz, T. A.; Jena, K. C.; Dixon, M. C.; Hore, D. K. *J. Phys. Chem. C* **2017,** *121,* 16879–16887.

[50] Su, T. J.; Lu, J. R.; Thomas, R. K.; Cui, Z. F. *J. Phys. Chem. B* **1999,** *103,* 3727–3736.

[51] Wertz, C. F.; Santore, M. M. *Langmuir* **1999,** *15,* 8884–8894.

[52] Ding, B.; Jasensky, J.; Li, Y.; Chen, Z. *Acc. Chem. Res.* **2016,** *49,* 1149–1157.

[53] Liu, Y.; Jasensky, J.; Chen, Z. *Langmuir* **2011,** *28,* 2113–2121.

[54] Yan, E. C. Y.; Wang, Z.; Fu, L. *J. Phys. Chem. B* **2015,** *119,* 2769–2785.

[55] Zhang, C.; Myers, J. N.; Chen, Z. *Soft Matter* **2013,** *9,* 4738–4761.

[56] Wei, F.; Ye, S.; Li, H.; Luo, Y. *J. Phys. Chem. C* **2013,** *117,* 11095–11103.

[57] Jarisz, T.; Roy, S.; Hore, D. K. *Acc. Chem. Res.* **2018,** *51,* 2287–2295.

[58] Arai, T.; Norde, W. *Colloids Surf.* **1990,** *51,* 1–15.

[59] Teughels, W.; Van Assche, N.; Sliepen, I.; Quirynen, M. *Clin. Oral Imp. Res.* **2006,** *17,* 68–81.

[60] Wang, J.; Buck, S. M.; Even, M. A.; Chen, Z. *J. Am. Chem. Soc.* **2002,** *124,* 13302–13305.

[61] Busscher, H. J.; Weerkamp, A. H. *FEMS Microbiol. Rev.* **1987,** *46,* 165–173.

[62] Trudeau, T. G.; Jena, K. C.; Hore, D. K. *J. Phys. Chem. C* **2009,** *113,* 20002–20008.

[63] Scatena, L. F.; Brown, M. G.; Richmond, G. L. *Science* **2001,** *292,* 908–912.

[64] Ta, T. C.; McDermott, M. T. *Anal. Chem.* **2000,** *72,* 2627–2634.

[65] Yee, N.; Fein, J. B.; Daughney, C. J. *Geochim. Cosmochim. Acta* **2000,** *64,* 609–617.

[66] Mei, S.; Yang, L.; Pan, Y.; Wang, D.; Wang, X.; Tang, T.; Wei, J. *Colloids Surf., B* **2019,** *174,* 207–215.

[67] Kim, J.; Cremer, P. S. *ChemPhysChem* **2001,** *2,* 543–546.

[68] Shen, S.-Y.; Schlag, E. W.; Selzle, H. L.; Yang, D.-Y. *J. Phys. Chem. A* **2008,** *112,* 797–802.

[69] Kong, J.; Yu, S. *Acta Biochim. Biophys. Sinica* **2007,** *39,* 549–559.

[70] Efimova, Y. M.; Haemers, S.; Wierczinski, B.; Norde, W.; van Well, A. A. *Biopolymers* **2006,** *85,* 264–273.

[71] Makhatadze, G. I.; Clore, G. M.; Gronenborn, A. M. *Nat. Struct. Biol.* **1995,** *2,* 852–855.

[72] Huyghues-Despointes, B.; Scholtz, M.; Pace, N. *Nat. Struct. Biol.* **1999,** *6,* 910–912.

[73] Ghosh, N.; Singh, A. K.; Mondal, J. A. *J. Phys. Chem. C* **2016,** *120,* 23596–23603.

[74] Castner, D. G.; Ratner, B. D. *Surf. Sci.* **2002,** *500,* 28–60.

[75] Dee, K. C.; Puleo, D. A.; Bizios, R. An Introduction to Tissue-Biomaterial Interactions. In ; Wiley: Hoboken, NJ, 2002; Chapter 3, pages 37–52.

[76] Flemming, H.-C.; Wingender, J. *Nature Rev.* **2010,** *8,* 623–633.

[77] Chamerlain, A. H. L. *Biofilms Sci. Tech.* **1992,** *223,* 59–67.

[78] Bakker, D.; Klijnstra, J. W.; Busscher, K. J.; van der Mei, H. C. *Biofouling* **2003,** *19,* 391–397.

[79] Beech, I. B.; Gubner, R.; Zinkevich, V.; Hanjangsit, L.; Avci, R. *Biofouling* **2000,** *16,* 93–104.

[80] Cooksey, K. E.; Wigglesworth-Cooksey, B. *Aquat. Microb. Ecol.* **1995,** *9,* 87–96.

[81] Comeau, J. W. D.; Pink, J.; Bezanson, E.; Douglas, C. D.; Pink, D.; Smith-Palmer, T. *Appl. Spectrosc.* **2009,** *63,* 1000–1007.

[82] Ceri, H.; Olson, M. E.; Stremick, C.; Read, R. R.; Morck, D.; Buret, A. *J. Clin. Microbiol.* **1999,** *37,* 1771–1776.

[83] Simoes, M. *Curr. Med. Chem.* **2011,** *18,* 2129–2145.

[84] Shen, Y. *J. Endodontics* **2011,** *37*, 657–661.

[85] Stoodley, P.; Boyle, J. D.; deBeer, D.; Lappin-Scott, H. M. *Biofouling* **1999,** *14*, 75–90.

[86] Simões, M.; Simões, L. C.; Vieira, M. J. *LWT Food Sci. Technol.* **2010,** *43*, 573–583.

[87] Costerson, J. W.; Stewart, P. S.; Greenberg, E. P. *Science* **1999,** *284*, 1318–1322.

[88] Olson, M. E.; Ceri, H.; Morck, D. W.; Buret, A. G.; Read, R. R. *Can. J. Vet. Res.* **2002,** *66*, 86–92.

[89] Danhorn, T.; Fuqua, C. *Ann. Rev. Microbiol.* **2007,** *61*, 401–422.

[90] Danese, P. N.; Pratt, L. A.; Kolter, R. *Methods Enzymol.* **2001,** *336*, 19–26.

[91] Hermansson, M. *Colloids Surf., B* **1999,** *14*, 105–119.

[92] Carniello, V.; Peterson, B. W.; van der Mei, H. C.; Busscher, H. J. *Adv. Colloid Interface Sci.* **2018,** *261*, 1–14.

[93] Waters, C. M.; Bassler, B. L. *Annu. Rev. Cell Dev. Biol.* **2005,** *21*, 319–346.

[94] Carbonell, X.; Corchero, J. L.; Cubarsi, R.; Vila, P.; Villaverde, A. *Microbiol. Res.* **2002,** *157*, 257–265.

[95] Cordeiro, M. A.; Werle, C. H.; Milanez, G. P.; Yano, T. *Brad. J. Microbiol.* **2016,** *47*, 414–416.

[96] Flemming, H.-C. *Microorganisms* **2016,** *4*, 41.

[97] McDougald, D.; Rice, S. A.; Berraud, N.; Sternberg, P. D.; Kjelleberg, S. *Nat. Rev.* **2012,** *10*, 39–50.

[98] Eshet, I.; Freger, V.; Kasher, R.; Herzberg, M.; Lei, J.; Ulbricht, M. *Biomacromolecules* **2011,** *12*, 2681–2685.

[99] Renner, L. D.; Weibel, D. B. *MRS Bull.* **2011,** *36,* 347–355.

[100] Bulard, E.; Fontaine-Aupart, M.-P.; Dubost, H.; Zheng, W.; Herry, J.-M.; Bellon-Fontaine, M.-N.; Briandet, R.; Bourguignon, B. *Spectrosc. Int. J.* **2012,** *27,* 571–579.

[101] Bulard, E.; Guo, Z.; Zheng, W.; Dubost, H.; Fontaine-Aupart, M.-P.; Bellon-Fontaine, M.-N.; Herry, J.-M.; Briandet, R.; Bourguignon, B. *Langmuir* **2011,** *27,* 4928–4935.

[102] Baier, R. E. *J. Biomech. Eng.* **1982,** *104,* 257–271.

[103] Eboigbodin, K. E.; Biggs, C. A. *Biomacromolecules* **2008,** *9,* 686–695.

[104] Norde, W.; Lyklema, J. *Colloids Surf.* **1989,** *38,* 1–13.

[105] Nagasawa, D.; Azuma, T.; Noguchi, H.; Uosaki, K.; Takai, M. *J. Phys. Chem. C* **2015,** *119,* 17193–17201.

[106] Hlady, V.; Buijs, J.; Jennissen, H. P. *Methods Enzymol.* **1999,** *309,* 402–429.

[107] Giussani, L.; Tabacchi, G.; Gianotti, E.; Coluccia, S.; Fois, E. *Phil. Trans. R. Soc. A* **2012,** *370,* 1463–1477.

[108] Derjaguin, B.; Landau, L. D. *Acta. Phys. Chim. U.R.S.S.* **1941,** *14,* 633–662.

[109] van Oss, C. J. *Colloids Surf., B* **1995,** *5,* 91–110.

[110] van Oss, C. J.; Good, R. J.; Chaudhury, M. K. *J. Colloid Interface Sci.* **1986,** *111,* 378–390.

[111] van Oss, C. J. *Cell Biophys.* **1989,** *14,* 1–16.

[112] Zobell, C. E. *J. Bacteriol.* **1943,** *46,* 39–56.

[113] Shenga, G.-P.; Yua, H.-Q.; Li, X.-Y. *Biotechnol. Adv.* **2010,** *28,* 882–894.

[114] Hufnagel, D. A.; Depas, W. H.; Chapman, M. R. *Microbiol. Spectr.* **2015,** *3,* 1–14.

[115] Geesey, G. G.; Mutch, R.; Costerton, J. W.; Green, R. B. *Limnol. Oceanogr.* **1978,** *23,* 1214–1223.

[116] Lawrence, J. R.; Swerhone, G. D. W.; Kuhlicke, U.; Neu, T. R. *Can. J. Microbiol.* **2007,** *53,* 450–458.

[117] Dunsmore, B. C.; Jacobsen, A.; Hall-Stoodley, L.; Bass, C. J.; Lappin-Scott, H. M.; Stoodley, P. *J. Ind. Microbiol. Biotechnol.* **2002,** *29,* 347–353.

[118] Decho, A. W.; Kawaguchi, T.; Allison, M. A.; Louchard, E. M.; Reid, R. P.; Stephens, F. C.; Voss, K. J.; Wheatcroft, R. A.; Taylor, B. B. *Liminol. Oceanogr.* **2003,** *48,* 431–443.

[119] Frolund, B.; Palmgren, R.; Keiding, K.; Nielsen, P. H. *Wat. Res.* **1996,** *30,* 1749–1758.

[120] Brown, M. J.; Lester, J. N. *Appl. Environ. Microbiol.* **1980,** *40,* 179–185.

[121] Zhao, W.; Walker, S. L.; Huang, Q.; Cai, P. *Chem. Geol.* **2015,** *410,* 79–88.

[122] Azeredo, J.; Oliveira, R. *Biofouling* **2000,** *16,* 59–67.

[123] Allison, D. G.; Sutherland, I. W. *J. Gen. Microbiol.* **1987,** *133,* 1319–1327.

[124] Diesner, M.-O.; Welle, A.; Kazanci, M.; Kaiser, P.; Spatz, J.; Koelsch, P. *Biointerphases* **2011,** *6,* 171–179.

[125] Diesner, M.-O.; Howell, C.; Kurz, V.; Verreault, D.; Koelsch, P. *J. Phys. Chem. Lett.* **2010,** *1,* 2339–2342.

[126] Howell, C.; Diesner, M.-O.; Grunze, M.; Koelsch, P. *Langmuir* **2008,** *24,* 13819–13821.

[127] Marisch, K.; Bayer, K.; Scharl, T.; Mairhofer, J.; Krempl, P. M.; Hummel, K.; Razzazi-Fazeli, E.; Striedner, G. *PLoS One* **2013,** *8,* e71506.

[128] Ingraham, J. L. *Growth of the Bacterial Cell;* Sinauer Associates Inc.: Sunderland, 1983.

[129] Donachie, W. D.; Begg, K. J.; Vicente, M. *Nature* **1976,** *264,* 328–333.

[130] Blattner, F. R. *et al. Science* **1997,** *277,* 1453–1462.

[131] Allen, R. J.; Waclaw, B. *Rep. Prog. Phys.* **2019,** *82,* 016601.

[132] Harshey, R. M. *Annu. Rev. Microbiol.* **2003,** *57,* 249–273.

[133] Hibino, H.; Takai, M.; Noguchi, H.; Sawamura, S.; Takahashi, Y.; Sakai, H.; Shiku, H. *J. Physiol. Sci.* **2017,** *67,* 439–445.

[134] Bohuszewicz, O.; Liu, J.; Low, H. H. *J. Struct. Biol.* **2016,** *196,* 3–14.

[135] Maier, R. M. Bacterial Growth. In *Environmental Microbiology*; Pepper, I.; Gerba, C.; Gentry, T.; Maier, R., Eds.; Academic Press Inc.: Burlington, 2008; Chapter 3, pages 37–54.

[136] Pletnev, P.; Osterman, I.; Sergiev, P.; Bogdanov, A.; Dontsova, O. *Acta Naturae* **2015,** *7,* 22–33.

[137] Kolter, R.; Siegele, D. A.; Tormo, A. *Annu. Rev. Microbiol.* **1993,** *47,* 855–874.

[138] Walker, S. L.; Hill, J. E.; Redman, J. A.; Elimelech, M. *Appl. Environ. Microbiol.* **2005,** *71,* 3093–3099.

[139] Pászti, Z.; Keszthelyi, T.; Hakkel, O.; Guczi, L. *J. Phys. Condens. Matter* **2008,** *20,* 224014.

[140] Watry, M. R.; Richmond, G. L. *J. Phys. Chem. B* **2002,** *106,* 12517-12523.

[141] Ji, N.; Shen, Y.-R. *J. Am. Chem. Soc.* **2004,** *126,* 15008–15009.

[142] Du, Q.; Freysz, E.; Shen, Y. R. *Phys. Rev. Lett.* **1994,** *72,* 238–241.

[143] Ong, S.; Zhao, X.; Eisenthal, K. B. *Chem. Phys. Lett.* **1992,** *191,* 327–335.

[144] Jena, K. C.; Hore, D. K. *J. Phys. Chem. C* **2009,** *113,* 15364–15372.

[145] Hall, S. A.; Hickey, A. D.; Hore, D. K. *J. Phys. Chem. C* **2010,** *114,* 9748–9757.

[146] Trudeau, T. G.; Hore, D. K. *Langmuir* **2010,** *26,* 11095–11102.

[147] Hall, S. A.; Jena, K. C.; Trudeau, T. G.; Hore, D. K. *J. Phys. Chem. C* **2011,** *115,* 11216–11225.

[148] Jena, K. C.; Covert, P. A.; Hore, D. K. *J. Phys. Chem. Lett.* **2011,** *2,* 1056–1061.

[149] Dixon, M. C. *J. Biomol. Techn.* **2008,** *19,* 151–158.

[150] Voinova, M. V.; Rodahl, M.; Jonson, M.; Kasemo, B. *Physica Scripta* **1999,** *59,* 391–396.

[151] Berglin, M.; Pinori, E.; Sellborn, A.; Andersson, M.; Hulander, M.; Elwing, H. *Langmuir* **2009,** *25,* 5602–5608.

[152] Gormally, M.; McKibben, R.; Johal, M.; Selassie, C. *Langmuir* **2009,** *25,* 10014–10019.

[153] Höök, F.; Voros, J.; Rodahl, M.; Kurrat, R.; Boni, P.; Ramsden, J. J.; Textor, M.; Spencer, N. D.; Tengvall, P.; Gold, J.; Kasemo, B. *Coll. Surf. B* **2002,** *24,* 155-170.

[154] Stålgren, J. J. R.; Eriksson, J.; Boschkova, K. *J. Colloid Interface Sci.* **2002,** *253,* 190–195.

[155] Bieri, M.; Burgi, T. *J. Phys. Chem. B.* **2005,** *109,* 22476–22485.

[156] Bieri, M.; Bürgi, T. *Phys. Chem. Chem. Phys.* **2006,** *8,* 513–520.

[157] Onorato, R. M.; Yoon, A. P.; Lin, J. T.; Somorjai, G. A. *J. Phys. Chem. C* **2012,** *116,* 9947–9954.

[158] Mermut, O.; Phillips, D. C.; York, R. L.; McCrea, K. R.; Ward, R. S.; Somorjai, G. A. *J. Am. Chem. Soc.* **2006,** *128,* 3598–3607.

[159] Phillips, D. C.; York, R. L.; Mermut, O.; McCrea, K. R.; Ward, R. S.; Somorjai, G. A. *J. Phys. Chem. C* **2007,** *111,* 255-261.

[160] York, R. L.; Holinga, G. J.; Somorjai, G. A. *Langmuir* **2009,** *25,* 9369–9374.

[161] Liu, C.; Thormann, E.; Claesson, P. M.; Tyrode, E. *Langmuir* **2014,** *30,* 8866–8877.

[162] Reviakine, I.; Johannsmann, D.; Richter, R. P. *Anal. Chem.* **2011,** *83,* 8838–8848.

[163] Dunér, G.; Thormann, E.; Dèdinaitò, A. *J. Coll. Inter. Sci.* **2013,** *408,* 229–239.

[164] Liu, S.; Kim, J. *J. Assoc. Lab. Autom.* **2009,** Aug, 213–220.

[165] McNeil-Watson, F. Electrophoretic Light Scattering. In *Encyclopedia of Biophysics*; Roberts, G. C. K., Ed.; Springer: Berlin, 2013.

[166] Nel, A. E.; Maedler, L.; Velegol, D.; Xia, T.; Hoek, E. M. V.; Somasundaran, P.; Klaessig, F.; Castranova, V.; Thompson, M. *Nat. Mater.* **2009,** *8,* 543–557.

[167] Soper, A. K. *Chem. Phys.* **2000,** *258,* 121–137.

[168] Roy, S.; Hore, D. K. *J. Phys. Chem. C* **2012,** *116,* 22867–22877.

[169] Covert, P. A.; Jena, K. C.; Hore, D. K. *J. Phys. Chem. Lett.* **2014,** *5,* 143–148.

[170] Raymond, E. A.; Tarbuck, T. L.; Richmond, G. L. *J. Phys. Chem. B* **2002,** *106,* 2817–2820.

[171] Segelstein, D. J. “The Complex Refractive Index of Water”, Master’s thesis, University of Missouri, 1981.

[172] Warren, S. G. *Appl. Opt.* **1984,** *23,* 1206–1225.

[173] Jarisz, T. A.; Lane, S.; Gozdzialski, L.; Hore, D. K. *J. Chem. Phys.* **2018,** *148,* 222825.

[174] Schultz, Z. D.; Shaw, S. K.; Gewirth, A. A. *J. Am. Chem. Soc.* **2005,** *127,* 15916–15922.

[175] Myalitsin, A.; Urashima, S.-h.; Nihonyanagi, S.; Yamaguchi, S.; Tahara, T. *J. Phys. Chem. C* **2016,** *120,* 9357–9363.

[176] Ostroverkhov, V.; Waychunas, G. A.; Shen, Y. R. *Phys. Rev. Lett.* **2005,** *94,* 046102.

[177] Fletcher, M. *J. Gen. Microbiol.* **1976,** *94,* 400–404.

[178] Ørstavik, D. *Acta Pathol. Scand., Sect. B: Microbiol.* **1977,** *85B,* 38–46.

[179] Rosenberg, M.; Kjelleberg, S. *Adv. Microbial Ecol.* **1986,** *9,* 353–393.

[180] Terlizzi, A.; Fraschetti, S.; Gianguzza, P.; Faimali, M.; Boero, F. *Aquat. Conserv.: Mar. Freshwater Ecosyst.* **2001,** *11,* 311–317.

[181] Simões, M.; Pereira, M. O.; Vieira, M. J. *Water Sci. Technol.* **2003,** *47,* 217–233.

[182] Chávez de Paz, L. E.; Bergenholtz, G.; Svensäter, G. *J. Endodontics* **2010,** *36,* 70–77.

[183] Norton, T. A.; Thompson, R. C.; Pope, J.; Veltkamp, C. J.; Banks, B.; Howard, C. V.; Hawkins, S. J. *Aquat. Microb. Ecol.* **1998,** *16,* 199–204.

[184] Costerton, J. W. *The Biofilm Primer;* Springer: Heidelberg, 2007.

[185] Romeo, T. *Bacterial Biofilms;* Springer: Heidelberg, 2008.

[186] Flemming, H.-C. *Springer Ser. Biofilms* **2011,** *5,* 81–109.

[187] Tanaka, M.; Hayashi, T.; Morita, S. *Polymer J.* **2013,** *45,* 701–710.

[188] Jena, K. C.; Hore, D. K. *Phys. Chem. Chem. Phys.* **2010,** *12,* 14383–14404.

[189] Shen, Y. R. *Pure Appl. Chem.* **2001,** *73,* 1589–1598.

[190] Eisenthal, K. B. *Chem. Rev.* **1996,** *96,* 1343–1360.

[191] Geiger, F. M. *Ann. Rev. Phys. Chem.* **2009,** *60,* 61–83.

[192] Shultz, M. J.; Schnitzer, C.; Simonelli, D.; Baldelli, S. *Int. Rev. Phys. Chem.* **2000,** *19,* 123–153.

[193] Gonella, G.; Lütgebaucks, C.; de Beer, A. G. F.; Roke, S. *J. Phys. Chem. C* **2016,** *120,* 9165–9173.

[194] Ohno, P. E.; Wang, H.-f.; Geiger, F. M. *Nature Comm.* **2017,** *8,* 1032.

[195] Liljeblad, J. F. D.; Tyrode, E. *J. Phys. Chem. C* **2012,** *116,* 22893–22903.

[196] Sposito, G. *The Chemistry of Soils, 2nd. ed.;* Oxford University Press: London, 2008.

[197] Marion, G. M.; Babcock, K. L. *Soil Sci.* **1976,** *122,* 181–187.

[198] Querry, M. R.; Waring, R. C.; Holland, W. E.; Hale, G. M.; Nijm, W. *J. Opt. Soc. Am.* **1972,** *62,* 849–855.

[199] Querry, M. R.; Holland, W. E.; Waring, R. C. *J. Opt. Soc. Am.* **1976,** *66,* 830–836.

[200] Tumolo, T.; Angnes, L.; Baptista, M. S. *Anal. Biochem.* **2004,** *333,* 273–279.

[201] Fisk, A. A. *Proc. Nat. Acad. Sci. USA* **1950,** *36,* 518–523.

[202] Sezonov, G.; Joseleau-Petit, D.; D'Ari, R. *J. Bacteriol.* **2007,** *189,* 8746–8749.

[203] Baron, S., Ed.; *Medical Microbiology;* University of Texas Medical Branch: Galveston, 1996.

[204] Dunne, Jr., W. M. *Clin. Microbiol. Rev.* **2002,** *15,* 155–166.

[205] Costerton, J. W.; Lewandowski, Z.; Caldwell, D. E.; Korber, D. R.; Lappin-Scott, H. M. *Annu. Rev. Microbiol.* **1995,** *49,* 711–745.

[206] Limoli, D. H.; Jones, C. J.; Wozniak, D. J. *Microbiol. Spectr.* **2015,** *3,* 1–30.

[207] Donlan, R. M. *Emerg. Infect. Dis.* **2002,** *8,* 881–890.

[208] Polissi, A.; Sperandeo, P. *Mar. Drugs* **2014,** *12,* 1023–1042.

[209] Clifton, L. A.; Skoda, M. W. A.; Le Brun, A. P.; Ciesielski, F.; Kuzmenko, I.; Holt, S. A.; Lakey, J. H. *Langmuir* **2015,** *31,* 404–412.

[210] Bulard, E.; Fontaine-Aupart, M.-P.; Dubost, H.; Zheng, W.; Bellon-Fontaine, M.-N.; Herry, J.-M.; Bourguignon, B. *Langmuir* **2012,** *28,* 17001–17010.

[211] Lawrence, J. R.; Wolfaardt, G. M.; Korber, D. R. *Appl. Environ. Microbiol.* **1994,** *60,* 1166–1173.

[212] Gilbert, P.; Evans, D. J.; Evans, E.; Duguid, I. G.; Brown, M. R. W. *J. Appl. Bacteriol.* **1991,** *71,* 72–77.

[213] Meister, K.; Roeters, S. J.; Paananen, A.; Woutersen, S.; Versluis, J.; Szilvay, G. R.; Bakker, H. J. *J. Phys. Chem. Lett.* **2017,** *8,* 1772–1776.

[214] Sun, V.; Jarisz, T. A.; Hore, D. K. *Langmuir* **2020,** *36,* 2120–2128.

[215] Marchioro, A.; Bischoff, M.; Lütgebaucks, C.; Biriukov, D.; Prědota, M.; Roke, S. *J. Phys. Chem. C* **2019,** *123,* 20393–20404.

[216] Franks, G. V. *J. Colloid Interface Sci.* **2002,** *249,* 44–51.

[217] Mitik-Dineva, N.; Wang, J.; Truong, V. K.; Stoddart, P.; Malherbe, F.; Crawford, R. J.; Ivanova, E. P. *Curr. Microbiol.* **2009,** *58,* 268–273.

[218] Ido, N.; Lybman, A.; Hayet, S.; Azulay, D. N.; Ghrayeb, M.; Liddawieh, S.; Chai, L. *Soft Matter* **2020,** *16,* 6180–6190.

[219] Eftekhari-Bafrooei, A.; Borguet, E. *J. Phys. Chem. Lett.* **2011,** *2,* 1353–1358.

[220] Chen, X.; Yang, T.; Kataoka, S.; Cremer, P. S. *J. Am. Chem. Soc.* **2007,** *129,* 12272–12279.

[221] Moradi, S.; Hadjesfandiari, N.; Toosi, S. F.; Kizhakkedathu, J. N.; Hatzikiriakos, S. G. *Appl. Mater. Interfaces* **2016,** *8,* 17631–17641.

[222] Agarwal, R.; García, A. J. *Adv. Drug Delivery Rev.* **2015,** *94,* 53–62.

[223] Ye, S.; Wei, F.; Li, H.; Tian, K.; Luo, Y. *Adv. Protein Chem. Struct. Biol.* **2013,** *93,* 213–255.

[224] Lu, J. R.; Zhao, X.; Yaseen, M. *Curr. Opin. Coll. Inter. Sci.* **2007,** *12,* 9–16.

[225] Chena, H.; Yuana, L.; Song, W.; Wub, Z.; Lia, D. *Prog. Poly. Sci.* **2008,** *33,* 1059–1087.

[226] Zhang, L.; Sun, Y. *Biochem. Eng. J.* **2010,** *48,* 408–415.

[227] Krishnan, S.; Weinman, C. J.; Ober, C. K. *J. Mater. Chem.* **2008,** *18,* 3405–3413.

[228] Elbert, D. L.; Hubbell, J. A. *Annu. Rev. Mater. Sci.* **1996,** *26,* 365–394.

[229] Green, R. J.; Frazier, R. A.; Shakesheff, K. M.; Davies, M. C.; Roberts, C. J.; Tendler, S. J. *Biomater.* **2000,** *21,* 1823–1835.

[230] Miyata, T.; Uragami, T.; Nakamae, K. *Adv. Drug Delivery Rev.* **2002,** *54,* 79-98.

[231] Adhikari, B.; Majumdar, S. *Prog. Polym. Sci.* **2004,** *29,* 699-766.

[232] Jin, W.; Brennan, J. *Anal. Chim. Acta* **2002,** *461,* 1-36.

[233] Hall, S. A.; Jena, K. C.; Covert, P. A.; Roy, S.; Trudeau, T. G.; Hore, D. K. *J. Phys. Chem. B* **2014,** *118,* 5617–5636.

[234] Nash, S. G. *J. Comput. Appl. Math.* **2000,** *124,* 45–49.

[235] Höök, F.; Kasemo, B.; Nylander, T.; Fant, C. *Anal. Chem.* **2001,** *73,* 5796–5804.

[236] Tagaya, M.; Ikoma, T.; Hanagata, N.; Yoshioka, T.; Tanaka, J. *Sci. Technol. Adv. Mater.* **2011,** *12,* 034411.

[237] Krause, K. D.; Roy, S.; Hore, D. K. *Biointerphases* **2017,** *12,* 02D407.

[238] Southall, N. T.; Dill, K. A.; Haymet, A. D. J. *J. Phys. Chem. B* **2002,** *106,* 521–533.

[239] Kresheck, G. C.; Schneider, H.; Scheraga, H. A. *J. Phys. Chem.* **1965,** *69,* 3132–3144.

[240] Broutin, I.; Riès-Kautt, M.; Ducruix, A. *J. Appl. Cryst.* **1995,** *28,* 614–617.

[241] Nagata, Y.; Pool, R. E.; Backus, E. H. G.; Bonn, M. *Phys. Rev. Lett.* **2012,** *109,* 226101.

[242] Liu, J.; Andino, R. S.; Miller, C. M.; Chen, X.; Wilkens, D. M.; Ceriotti, M.; Manolopoulos, D. E. *J. Phys. Chem. C* **2013,** *117,* 2944–2951.

[243] Sultanova, N.; Kasarova, S.; Kokolov, I. *Acta Phys. Polonica A* **2009,** *116,* 585–587.

[244] Malitson, I. H. *Appl. Opt.* **1963,** *2,* 1103–1107.

[245] Max, J.-J.; Chapados, C. *J. Chem. Phys.* **2009,** *131,* 184505.

[246] Zhang, Y.; Cremer, P. S. *Ann. Rev. Phys. Chem.* **2010,** *61,* 63–83.

[247] Holinga, G. J.; York, R. L.; Onorato, R. M.; Thompson, C. M.; Webb, N. E.; Yoon, A. P.; Somorjai, G. A. *J. Am. Chem. Soc.* **2011,** *133,* 6243–6253.

[248] Stiopkin, I. V.; Weeraman, C.; Pieniazek, P. A.; Shalhout, F. Y.; Skinner, J. L.; Benderskii, A. V. *Nature* **2011,** *474,* 192–195.

[249] Zhang, Z.; Piatkowski, L.; Bakker, H. J.; Bonn, M. *J. Chem. Phys.* **2011,** *135,* 021101.

[250] Zhang, Z.; Piatkowski, L.; Bakker, H. J.; Bonn, M. *Nat. Chem.* **2011,** *3,* 888–893.

[251] Hofmann, M. J.; Koelsch, P. Soft Matter at Aqueous Interfaces. In ; Springer: New York, 2016; Chapter 15, pages 491–514.

[252] Cho, J.; Kushiro, K.; Teramura, Y.; Takai, M. *Biomacromol.* **2014,** *15,* 2012–2018.

[253] Athamneh, A. I. M.; Alajlouni, R. A.; Wallace, R. S.; Seleem, M. N.; Senger, R. S. *Antimicrob. Agents Chemother.* **2014,** *58,* 1302–1314.

[254] Chao, Y.; Zhang, T. *Anal. Bioanal. Chem.* **2012,** *404,* 1465–1475.